REPUBLIC OF TÜRKİYE
YILDIZ TECHNICAL UNIVERSITY
GRADUATE SCHOOL OF SCIENCE AND ENGINEERING

ENHANCING GEL ELECTROLYTE PERFORMANCE IN LEAD-ACID BATTERIES USING CONDUCTIVE POLYMER/GRAPHITE COMPOSITES

Ziyad Nidhal Moosa MIRA

DOCTOR OF PHILOSOPHY THESIS

Department of Metallurgical and Materials Engineering

Program of Materials Science and Engineering

Supervisor

Prof. Dr. Metin GENÇTEN

April, 2026

REPUBLIC OF TÜRKİYE

YILDIZ TECHNICAL UNIVERSITY

GRADUATE SCHOOL OF SCIENCE AND ENGINEERING

ENHANCING GEL ELECTROLYTE PERFORMANCE IN LEAD-ACID BATTERIES USING CONDUCTIVE POLYMER/GRAPHITE COMPOSITES

A thesis submitted by Ziyad MIRA in partial fulfillment of the requirements for the degree of **DOCTOR OF PHILOSOPHY** is approved by the committee on 01.04.2026 in Department of Metallurgical and Materials Engineering, Program of Materials Science and Engineering.

Prof. Dr. Metin GENÇTEN
Yildiz Technical University
Supervisor

Approved By the Examining Committee

Prof. Dr. Metin GENÇTEN, Supervisor
Yildiz Technical University _____

Prof. Dr. Nilgün KARATEPE YAVUZ, Member
Istanbul Technical University _____

Assoc. Prof. Dr. Buğra ÇİÇEK, Member
Yildiz Technical University _____

Assoc. Prof. Dr. Burak BİROL, Member
Yildiz Technical University _____

Assoc. Prof. Dr. Melih Beşir ARVAS, Member
Istanbul University _____

I hereby declare that the study entitled “Enhancing Gel Electrolyte Performance in Lead-Acid Batteries Using Conductive Polymer/Graphite Composites” that I prepared under the supervision of Prof. Dr. Metin GENÇTEN was conducted in full compliance with the relevant legal requirements regarding data collection and data use; that all information obtained from other sources has been fully and properly acknowledged in the main text and references; that no fabrication and/or falsification has been made with respect to the research data or findings; and that throughout the study I have adhered to the principles of scientific research and academic ethics.

Generative Artificial Intelligence (GenAI) technologies were not employed at any stage of this thesis study, including its conceptualization, planning, execution, evaluation, or the writing process; the work was conducted entirely through my own original effort.

I accept full administrative and legal responsibility for any consequences that may arise if this declaration is determined to be false.

Ziyad Nidhal Moosa MIRA

Signature

This work was supported by “The Scientific and Technological Research Council of Türkiye (TÜBITAK) under 124M200 project code”.

To my family —

your love, sacrifice, and unwavering support made this possible.

This achievement is yours as much as it is mine.

ACKNOWLEDGEMENTS

First of all, thanks to ALLAH for giving me the strength and patience to complete this work.

I would like to sincerely thank my supervisor, Prof. Dr. Metin GENÇTEN, for his continuous guidance, support, and encouragement throughout my PhD. His advice and belief in me helped me move forward, especially during difficult times. I am truly grateful for his mentorship and kindness.

I would also like to express my deepest gratitude to my beloved wife, my son Husam, my daughter Maryam, and my parents and family. Your love, patience, and constant support gave me the strength to continue this journey. Thank you for standing beside me in every step and for believing in me when things were not easy.

I also thank my colleagues and friends for their support and for creating a positive and cooperative research environment. My appreciation goes to the Gençten Research Group (GRG) at Yildiz Technical University for its technical and academic support. I am thankful to the jury members (Dr. Nilgün KARATEPE YAVUZ), (Dr. Buğra ÇİÇEK), (Dr. Burak BİROL), and (Dr. Melih Beşir ARVAS) for their valuable comments and contributions.

This achievement belongs to everyone who supported me along the way.

Ziyad Nidhal Moosa MIRA

TABLE OF CONTENTS

LIST OF SYMBOLS ix

LIST OF ABBREVIATIONS x

LIST OF FIGURES xi

LIST OF TABLES xiv

ABSTRACT xvi

ÖZET xviii

1 INTRODUCTION 1

1.1 Energy Storage Systems (EESs) 1

1.1.1 Battery Systems 1

1.1.2 Lead Acid Batteries 2

1.1.3 Classifications Lead Acid Batteries 3

1.1.4 Flooded (Wet) Lead Acid Batteries 3

1.1.5 Dry (Maintinance Free) Lead Acid Batteries 4

1.1.6 Absorbed Mat Glass Batteries (AGM) 4

1.1.7 Gel-Type Valve Regulated Batteries (VRLA) 5

1.1.8 Conductive Polymers CPs 8

1.2 The Aim of the Study 9

2 EXPERIMENTAL WORK 10

2.1 Introduction 10

2.1.1 Materials 10

2.1.2 Synthesis of Conductive Polymers CP's and Conductive Polymers/Graphite Composites 10

2.1.3 Characterization of Conductive Polymers and Conductive Polymers/Graphite Composite 19

2.1.4 Preparation of Gel Electrolyte 21

2.1.5 Electrochemical Characterization of Gel Electrolytes 25

3 RESULTS AND DISCUSSION **28**

3.1 Introduction 28

3.2 Characterization Analysis Tests 28

3.2.1 Fourier-Transform Infrared Spectroscopy (FT-IR) 29

3.2.2 Electrical Conductivity (EC) 31

3.2.3 Differential Scanning Calorimetry and Thermogravimetric Analysis DSC-TGA 34

3.2.4 Brunauer, Emmett & Teller (BET) 37

3.2.5 Field Emission Scanning Electron Microscopy (EF-SEM) and Scanning Electron Microscopy (SEM) 40

3.3 Optimization and characterization of Gel Electrolyte Systems 45

3.3.1 Optimization of Conductive Polymers and Conductive Polymers/Graphite Composites Additives in Fumed Silica Gel Electrolyte 46

3.3.2 Optimization of Conductive Polymers and Conductive Polymers/Graphite Composites Additives Content in Fumed Silica Gel Electrolyte 46

3.3.3 Optimization of Stirring Time for the Preparation of Conductive Polymers and Conductive Polymers/Graphite Composites - Containing Fumed Silica-Based Gel Electrolytes 62

3.3.4 Optimization of Stirring Rates for the Preparation of Conductive Polymers and Conductive Polymers Composites-Containing Fumed Silica-Based Gel Electrolytes 74

3.4 Battery Test for Polymers and Conductive Polymers Composites-Containing Fumed Silica-Based Gel Electrolyte 81

4 CONCLUSION **84**

4.1 Conclusion 84

REFERENCES **87**

PUBLICATIONS FROM THE THESIS **102**

LIST OF SYMBOLS

C	Coulombic efficiency
Z”	Imaginary resistance
mAh g^{-1}	Milliampere hour over gram
mA g^{-1}	Milliampere over gram
mV s^{-1}	Millivolt over second
Ω	Ohm
Z’	Real resistance

LIST OF ABBREVIATIONS

AGM	Absorbed glass mat
CPs	Conductive polymers
CV	Cyclic voltammetry
EC	Electrical conductivity
E_{corr}	Corrosion potential
EESs	Energy storage systems
EIS	Electrochemical impedance spectroscopy
GCDT	Galvanostatic charge-discharge test
I_{corr}	Corrosion current density
LSEVs	Low speed electric vehicles
NAM	Negative active material
Ni-Cd	Nickle-cadmium
Ni-MH	Nickle-metal hydride
OCP	Open circuit potential
PANi	Polyaniline
PANi/G	Polyaniline/graphite composite
PPy	Polypyrrole
PTF	Polythiophene
PTF/G	Polythiophene/graphite composite
R_{ct}	Charge transfer resistance
R_s	Solution resistance
SCE	Saturated calomel electrode
SLI	Starting, lighting, and ignition
UPS	Uninterrupted power source
VRLA	Valve regulated lead acid
W	Warburg

LIST OF FIGURES

Figure 1.1 Lead acid battery's structure and work principle **2**

Figure 1.2 Classifications of lead acid batteries **3**

Figure 1.3 Fumed silica gel network **6**

Figure 2.1 Schematic of synthesizing process and characterizations of different CPs **12**

Figure 2.2 Schematic of Gel preparation and optimization with different parameters **24**

Figure 2.3 Gamry ınterface 1010b potentiostat/galvanostat **25**

Figure 2.4 Gamry ınterface 1010b potentiostat/galvanostat **26**

Figure 2.5 NEWARE-4000 multichannel testing system **27**

Figure 3.1 FT-IR test of conductive polymers and conductive polymers/composites. a) represents PANi and PANi/G composite. b) represents PTF and PTF/G composite. c) represents PPy..... **31**

Figure 3.2 Electrical conductivity of CPs and their graphite composites under various conditions: a) varying aniline concentration; b) sulfuric acid concentration; c) PANi/graphite content; d) thiophene concentration; e) HCl concentration; f) PTF/graphite content; g) varying pyrrole concentration; h) sulfuric acid concentration. **34**

Figure 3.3 DSC-TGA thermal analysis of a) polyaniline powder; b) Polyaniline/Graphite composite powder; c) Polythiophene powder; d) Polythiophene/Graphite composite powder; e) Polypyrrole powder **37**

Figure 3.4 BET analysis (Surface area & Pore diameter) of CPs and their graphite composites under various conditions: a) varying aniline concentration; b) sulfuric acid concentration; c) PANi/graphite content; d) thiophene concentration; e) HCl concentration; f) PTF/graphite content; g) varying pyrrole concentration; h) sulfuric acid concentration. **40**

Figure 3.5 Scanning electron microscopy of different polyaniline samples synthesized using varying concentration of monomer and sulfuric acid. **41**

Figure 3.6 Scanning electron microscopy of different polyaniline/graphite composite samples synthesized using varying graphite content. **42**

Figure 3.7 Field emission scanning electron microscopy of different polythiophene samples synthesized using varying concentration of monomer and hydrochloric acid. **43**

Figure 3.8 Field emission scanning electron microscopy of different polythiophene/graphite composite samples synthesized using different graphite content. **44**

Figure 3.9 SEM images of chemically synthesized PPy with different pyrrole concentrations (a, b, c) and different sulfuric acid concentrations (d, e, f, g). **45**

Figure 3.10 Cyclic voltammetry analysis of fumed silica-based gel electrolytes containing different additive contents at stirring time 30 min and stirring rate 500 rpm (a) PANi, (b) PANi/G composite, (c) PPy, (d) PTF, and (e) PTF/G composite. **51**

Figure 3.11 Electrochemical impedance spectroscopy EIS of fumed silica-based gel electrolytes containing different additive contents at stirring time 30 min and stirring rate 500 rpm (a) PANi, (b) PANi/G composite, (c) PPy, (d) PTF, and (e) PTF/G composite. **58**

Figure 3.12 TAFEL polarization analysis of fumed silica-based gel electrolytes containing different additive contents at stirring time 30 min and stirring rate 500 rpm (a) PANi, (b) PANi/G composite, (c) PPy, (d) PTF, and (e) PTF/G composite. **61**

Figure 3.13 Cyclic voltammetry analysis for gel systems prepared at 500 rpm with different stirring time containing (a) 0.6 wt% of PANi, (b) 0.6 wt% of PANi/G composite, (c) 0.8 wt% of PPy, (d) 0.2 wt% of PTF, and (e) 0.2 wt% of PTF /G composite. **64**

Figure 3.14 Electrochemical impedance spectroscopy for gel systems prepared at 500 rpm with different stirring time containing (a) 0.6 wt% of PANi, (b) 0.6 wt% of PANi/G composite, (c) 0.8 wt% of PPy, (d) 0.2 wt% of PTF, and (e) 0.2 wt% of PTF /G composite **70**

Figure 3.15 Tafel Polarization analysis for gel systems prepared at 500 rpm with different stirring time containing (a) 0.6 wt% of PANi, (b) 0.6 wt% of PANi/G composite, (c) 0.8 wt% of PPy, (d) 0.2 wt% of PTF, and (e) 0.2 wt% of PTF /G composite. **73**

Figure 3.16 Cyclic voltammetry analysis for gel systems prepared with different stirring rates containing (a) 0.6 wt% of PANi for 90 min, (b) 0.6 wt% of PANi/G composite for 150 min, (c) 0.8 wt% of PPy for 60 min, (d) 0.2 wt% of PTF for 30 min, and (e) 0.2 wt% of PTF /G composite for 30 min. **75**

Figure 3.17 Electrochemical impedance spectroscopy (EIS) analysis for gel systems prepared with different stirring rates containing (a) 0.6 wt% of PANi for 90 min, (b) 0.6 wt% of PANi/G composite for 150 min, (c) 0.8 wt% of PPy for 60 min, (d) 0.2 wt% of PTF for 30 min, and (e) 0.2 wt% of PTF /G composite for 30 min **78**

Figure 3.18 TAFEL polarization analysis for gel systems prepared with different stirring rates containing (a) 0.6 wt% of PANi for 90 min, (b) 0.6 wt% of PANi/G composite for 150 min, (c) 0.8 wt% of PPy for 60 min, (d) 0.2 wt% of PTF for 30 min, and (e) 0.2 wt% of PTF /G composite for 30 min **80**

Figure 3.19 Galvanostatic charge/discharge test results for different electrolyte systems: (a) Initial capacities of sulfuric acid electrolyte, fumed silica-based electrolyte, PANi-doped gel electrolyte (0.6 wt% PANi, 90 minutes stirring at 500 rpm), PANi/G-doped gel electrolyte (0.6 wt% PANi/G, 150 minutes stirring at 500 rpm), PPy-doped gel electrolyte (0.8 wt% PPy, 60 minutes stirring at 500 rpm), PTF-doped gel electrolyte (0.2 wt% PTF, 30 minutes stirring at 500 rpm), and PTF/G-doped gel electrolyte (0.2 wt% PTF/G, 30 minutes stirring at 500 rpm). (b) Long-cycle test performance, showing coulombic efficiency and retention capacity for sulfuric acid electrolyte, fumed silica-based electrolyte, and Conductive polymers and conductive polymers composites additives fumed silica-based gel electrolyte. **.....82**

Figure 4.1 VRLA gel electrolytes. a) specific capacity with different additive materials, b) capacity retention with different additive materials.....**86**

LIST OF TABLES

Table 2.1 Polyaniline synthesis parameters with different concentrations of monomers and acid **13**

Table 2.2 Polypyrrole synthesis parameters with different concentrations of pyrrole monomer and sulfuric acid **15**

Table 2.3 Polyaniline/graphite composite synthesis parameters with different graphite powder additive..... **16**

Table 2.4 Polythiophene synthesis parameters with different concentrations of thiophene monomer and hydrochloric acid..... **17**

Table 2.5 Polythiophene/graphite composite synthesis parameters with different graphite powder additive..... **19**

Table 2.6 Preparation conditions for aqueous electrolyte, fumed silica-based gel electrolyte, and PANi-added fumed silica-based gel electrolytes **23**

Table 3.1 The Optimal Samples of CP's and CP's/G Composite That Used as Gel Additives **46**

Table 3.2 R_s, R_{ct}, I_{corr}, and corrosion rate values of fumed silica-based gel electrolytes containing different amounts of PANi (wt%) **53**

Table 3.3 R_s, R_{ct}, I_{corr}, and corrosion rate values of the gel electrolyte prepared at different PANi/G composite content **54**

Table 3.4 The R_s, R_{ct}, E_{corr}, and I_{corr} values of the electrolyte consisting of different amounts of PPy in fumed silica-based gel electrolyte **55**

Table 3.5 The R_s, R_{ct}, E_{corr}, and I_{corr} values of the electrolyte consisting of different PTF content in fumed silica-based gel electrolyte **56**

Table 3.6 The R_s, R_{ct}, E_{corr}, and I_{corr} values of the electrolyte consisting of different PTF/G composite content in fumed silica-based gel electrolyte..... **57**

Table 3.7 R_s, R_{ct}, I_{corr}, and corrosion rate values of the gel electrolyte containing PANi 0.6 wt% prepared at different stirring times. **65**

Table 3.8 R_s, R_{ct}, I_{corr}, and corrosion rate values of the PANi/G-doped gel electrolyte prepared at different stirring rates. **66**

Table 3.9 The R_s, R_{ct}, E_{corr}, and I_{corr} values obtained for fumed silica-based gel electrolyte consisting of 0.8 wt% of PPy at different stirring times ... **67**

Table 3.10 The R_s, R_{ct}, E_{corr}, and I_{corr} values obtained for fumed silica-based gel electrolyte consisting of 0.2 wt% of PTF at different stirring times... **68**

Table 3.11 The R_s, R_{ct}, E_{corr}, and I_{corr} values obtained for fumed silica-based gel electrolyte consisting of 0.2 wt% of PTF/G composite at different stirring times. **69**

Table 3.12 R_s, R_{ct}, I_{corr}, and corrosion rate values of the PANi-doped gel electrolyte prepared at different stirring rates **76**

Table 3.13 R_s, R_{ct}, I_{corr}, and corrosion rate values of the PANi/G-doped gel electrolyte prepared at different stirring rates **76**

Table 3.14 The R_s, R_{ct}, E_{corr} and I_{corr} values obtained for fumed silica-based gel electrolyte consisting of 0.8 wt% of PPy at different stirring rates **77**

Table 3.15 The R_s, R_{ct}, E_{corr} and I_{corr} values obtained for fumed silica-based gel electrolyte consisting of 0.2 wt% of PTF at different stirring rates **77**

Table 3.16 The R_s, R_{ct}, E_{corr} and I_{corr} values obtained for fumed silica-based gel electrolyte consisting of 0.2 wt% of PTF/G composite at different stirring rates **77**

Table 3.17 Initial Capacity and Retention Capacity for different gel systems with different conductive additives. **83**

Table 4.1 Different gel systems with different preparation parameters and their results **85**

ABSTRACT

Enhancing Gel Electrolyte Performance in Lead-Acid Batteries Using Conductive Polymer/Graphite Composites

Ziyad Nidhal Moosa MIRA

Department of Metallurgical and Materials Engineering

Doctor of Philosophy Thesis

Supervisor: Prof. Dr. Metin GENÇTEN

In this work, chemically synthesized conductive polymers (CPs) and their composites were introduced for the first time as additive materials in gel-type valve-regulated lead–acid (VRLA) batteries to enhance electrical conductivity and charge transfer characteristics of the gel electrolyte. Polyaniline (PANi), polypyrrole (PPy), polythiophene (PTF), polyaniline/graphite (PANi/G), and polythiophene/graphite (PTF/G) were synthesized via chemical oxidative polymerization using different concentrations of monomers, and acids. The obtained powders were characterized using spectroscopic and microscopic techniques to determine their suitability for gel electrolyte applications.

A series of gel systems were prepared by varying three key parameters: additive content, stirring time, and stirring rate, which are critical for gel optimization. Electrochemical analyses, including cyclic voltammetry (CV), electrochemical impedance spectroscopy (EIS), and Tafel extrapolation, were conducted to evaluate performance. The optimal conditions were identified as follows: 0.6 wt% PANi (90 min, 500 rpm), 0.6 wt% PANi/G (150 min, 500 rpm), 0.8 wt% PPy (60 min, 500 rpm), and 0.2 wt% PTF and PTF/G (30 min, 500 rpm). These systems exhibited superior electrochemical behavior in terms of redox activity, reduced charge

transfer resistance, improved diffusion characteristics, and enhanced corrosion resistance.

Galvanostatic charge–discharge (GCD) tests were performed on the optimized systems, with initial capacity measured at 5 mA g^{-1} and cycling stability evaluated over 200 cycles at 10 mA g^{-1}. The results demonstrated significant improvements in coulombic efficiency, capacity retention, and cyclic stability compared to both fumed silica-based gel electrolyte and aqueous sulfuric acid electrolyte. The highest initial capacity was achieved by the PTF/G-based gel (55.75 mAh g^{-1}), followed by PANi, PANi/G, PPy, and PTF systems, all outperforming the reference systems. Overall, the incorporation of CPs and their composites effectively enhance the electrochemical performance of VRLA gel electrolytes, highlighting their strong potential for advanced energy storage applications.

Keywords: VRLA batteries, gel electrolyte, conductive polymers - composites, electrochemical optimization, chemical oxidative polymerization.

ÖZET

Jel Elektrolit Tabanlı Kurşun-Asit Akülerde İletken Polimer/Grafit Kompozit Katkılarla Performans Artırımı

Ziyad Nidhal Moosa MIRA

Metalurji ve Malzeme Mühendisliği Anabilim Dalı

Malzeme Bilimi ve Mühendisliği Programı

Doktora Tezi

Danışman: Prof. Dr. Metin GENÇTEN

Bu çalışmada, kimyasal olarak sentezlenen iletken polimerler (CP'ler) ve bunların kompozitleri, jel tipi valf kontrollü kurşun-asit (VRLA) akülerde elektriksel iletkenliği ve jel elektrolitin yük transfer özelliklerini artırmak amacıyla literatürde ilk kez katkı maddesi olarak kullanılmıştır. Polianilin (PANi), polipirrol (PPy), politiyofen (PTF), polianilin/grafit (PANi/G) ve politiyofen/grafit (PTF/G), uygun monomer ve asit konsantrasyonları kullanılarak kimyasal oksidatif polimerizasyon yöntemiyle sentezlenmiştir. Elde edilen tozlar, jel elektrolit uygulamalarına uygunluklarını belirlemek amacıyla spektroskopik ve mikroskobik tekniklerle karakterize edilmiştir.

Jel optimizasyonu için kritik öneme sahip olan katkı maddesi oranı, karıştırma süresi ve karıştırma hızı gibi üç temel parametre değiştirilerek farklı jel sistemleri hazırlanmıştır. Performans değerlendirmesi amacıyla döngüsel voltametri (CV), elektrokimyasal empedans spektroskopisi (EIS) ve Tafel ekstrapolasyonu gibi elektrokimyasal analizler gerçekleştirilmiştir. En uygun koşullar; %0,6 PANi (90 dk, 500 rpm), %0,6 PANi/G (150 dk, 500 rpm), %0,8 PPy (60 dk, 500 rpm) ve %0,2 PTF ile PTF/G (30 dk, 500 rpm) olarak belirlenmiştir. Bu sistemler, redoks

aktivitesi, düşük yük transfer direnci, gelişmiş difüzyon özellikleri ve yüksek korozyon direnci açısından üstün elektrokimyasal performans sergilemiştir.

Optimize edilen sistemler üzerinde galvanostatik şarj-deşarj (GCD) testleri uygulanmış; başlangıç kapasitesi 5 mA g^{-1} akım yoğunluğunda ölçülmüş ve çevrim kararlılığı 10 mA g^{-1}'de 200 çevrim boyunca değerlendirilmiştir. Sonuçlar, hem dumanlı silika bazlı jel elektrolit hem de sulu sülfürik asit elektrolitine kıyasla Coulomb verimliliği, kapasite korunumu ve çevrimsel kararlılık açısından önemli iyileşmeler göstermiştir. En yüksek başlangıç kapasitesi PTF/G bazlı jel için 55,75 mAh g^{-1} olarak elde edilmiş; bunu sırasıyla PANi, PANi/G, PPy ve PTF sistemleri izlemiştir. Tüm sistemler referans elektrolitlere göre daha üstün performans göstermiştir. Genel olarak, iletken polimerlerin ve kompozitlerinin kullanımı, VRLA jel elektrolitlerin elektrokimyasal performansını önemli ölçüde artırmakta olup, ileri enerji depolama uygulamaları için yüksek potansiyel sunmaktadır.

Anahtar Kelimeler: VRLA aküleri, jel elektrolit, iletken polimerler - kompozitler, elektrokimyasal optimizasyon, kimyasal oksidatif polimerizasyon.

1
INTRODUCTION

1.1 Energy Storage Systems (EESs)

The rapid growth of energy demands due to urbanization, industrialization and the rapid growth of technological societies has put huge pressure on fossil fuels resources. In the last century, fossil fuels were the dominant energy source for transportation, industries and other energy needs. fossil fuels depletion and the rapid CO_2 emissions put the world in front of huge climate and energy issues [1]–[4]. Renewable energy sources such as solar, tidal, wind, hydropower, biofuels, etc., have expanded rapidly [5]. Nevertheless, the renewable energy sources are intermittent and variable, which make it instable for power generation and grid reliability [2], [3], [6]. Energy storage systems (ESSs) therefore play a major role for energy sector by integrating large-scale stored energy into the power network. By storing excess energy during high energy generation and releasing it again during the peaks of energy demands, the energy storage systems reduce the dependence on fossil fuels systems, improve energy efficiency as well as enhance energy stability [1], [6], [7].

1.1.1 Battery Systems

Rechargeable batteries play a crucial role in modern energy storage systems, supporting a wide range of applications from portable electronic devices to electric vehicles and the integration of renewable energy sources [1]–[4]. Among various battery technologies, lithium-ion batteries dominate the market due to their high energy density and relatively long cycle life, while suffering from the safety issue as well as its sensitivity to high temperatures. However, nickel–cadmium (Ni–Cd) and nickel–metal hydride (Ni–MH) batteries are still used in specific industrial applications where robustness and tolerance to extreme conditions are prioritized. On the other hand, they have low specific energy compared to Li-ion batteries as

well as the high cost and heavy weight of the batteries. Zinc–air batteries, in contrast, offer significant environmental advantages and exceptionally high theoretical capacities, rendering them suitable for applications such as medical equipment and backup power systems, but it has low nominal potential and low specific energy limiting their usage applications [3]–[9].

1.1.2 Lead Acid Batteries

Lead-acid batteries were invented in 1859 by the French physicist Louis Gaston. Since their invention, many developments have been made to improve their performance and overcome usage limitations. However, their basic structure and working principle have remained unchanged [4], [10], [11]. A lead-acid battery consists of two electrodes made of lead and lead dioxide, immersed in an aqueous electrolyte composed of sulfuric acid and water, the electrodes insulation materials were used as separators [2], [12]. Until the 1970s, lead-acid batteries utilized aqueous electrolytes and were known as flooded batteries. These batteries were valued for their low cost, high safety, stability, and good cold cranking performance. However, they required periodic maintenance due to water consumption, electrolyte stratification, and gas evolution caused by electrochemical reactions. Lead acid batteries are widely used as primary energy storage systems in various applications, such as telecommunications, starting, lighting, and ignition (SLI) systems, low-speed electric vehicles (LSEVs), emergency life support systems in the healthcare sector, automobiles, and uninterruptible power supply (UPS) systems [1], [4], [10]. Figure 1.1 illustrates the lead acid battery's structure and work principle.

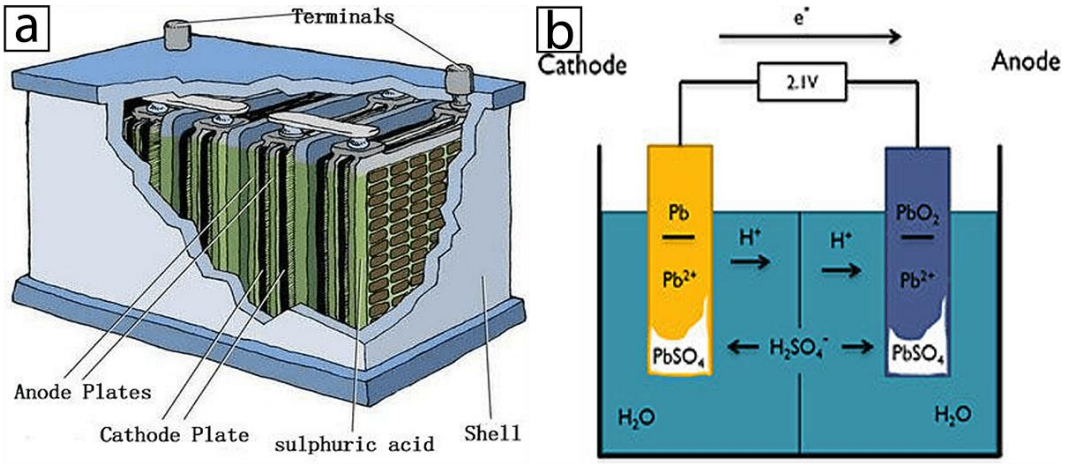


Figure 1.1 Lead acid battery's structure and work principle

The lead acid batteries work principle during charge/discharge can be described in the reactions below:

$$Pb + SO_4^{2-} \rightleftarrows PbSO_4 + 2e^- \quad (1.1)$$

$$PbSO_4 + 2H_2O \rightleftarrows PbO_2 + SO_4^{2-} + 4H^+ + 2e^- \quad (1.2)$$

The overall reaction at both electrodes surface,

$$Pb + PbO_2 + 2H_2SO_4 \rightleftarrows 2PbSO_4 + 2H_2O \quad (1.3)$$

1.1.3 Classifications Lead Acid Batteries

Lead acid batteries are classified into two major groups, the flooded lead acid batteries and the dry lead acid batteries as listed in Figure 1.2.

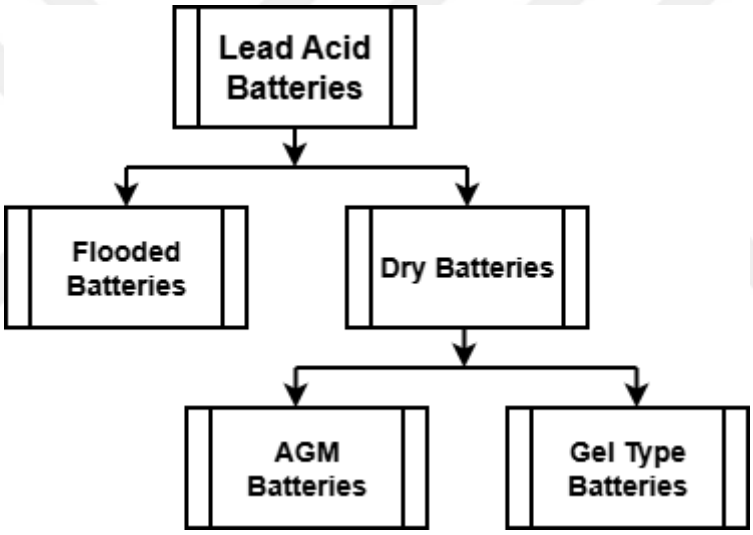


Figure 1.2 Classifications of lead acid batteries

1.1.4 Flooded (Wet) Lead Acid Batteries

This type of lead acid batteries is also called the maintenance batteries, which needs periodic maintenance, consists of two electrodes of lead and lead dioxide that were immersed in aqueous electrolyte of 30% sulfuric acid. In such batteries, oxygen and hydrogen are released on the plates in case of overcharging. Due to the direct removal of these gases from the system, the amount of electrolyte decreases over time, and consequently, a decrease in the contact surface with the electrolyte is observed [4], [10], [13]. This causes the battery to overheat, reducing battery

performance and shortening the battery's lifespan. Therefore, continuous electrolyte replenishment is required. This need for continuous maintenance has led to wet-cell batteries being called maintenance batteries.

1.1.5 Dry (Maintenance Free) Lead Acid Batteries

This type is also known as maintenance free lead acid batteries which consist of sealed box contain battery components, in this type of the box contains valves that control gas inside the box, in this type of electrolyte keeps its consistency and keeps properties. This type has longer lifespan, no gas emission as well as high safety than flooded type. VRLA battery systems are recombinant batteries. This means that oxygen formed in the positive plates reacts with hydrogen in the negative plates to form water [14]. Therefore, in VRLA batteries, water is not released from the cell but is instead subjected to conversion. Thus, VRLA batteries can be subjected to sufficiently high overcharging to convert almost all active material without water loss, and do not require maintenance such as electrolyte addition during this process [4], [10], [14]. VRLA lead-acid batteries have a safety pressure relief valve. The pressure relief valve maintains the internal pressure, which helps recombination by keeping the gases within the cell long enough for diffusion to occur [15], [16]. The valve is a safety feature in case the rate of hydrogen formation becomes dangerously high. If the valve is activated, excess hydrogen is released into the atmosphere via vent or through the plastic container [14]. In VRLA batteries, the cell is filled with electrolytes only enough to coat the surfaces, and in these systems the electrolyte is either absorbed in the separator material or deactivated in a gel. This allows for homogeneous gas transfer between the plates, which is necessary to support recombination reactions [2], [17]. The capacity of a VRLA battery is limited by the amount of positive plate or positive active material [14].

1.1.6 Absorbed Mat Glass Batteries (AGM)

The electrolyte can be immobilized using an absorbent glass mat (AGM) separator or a gel electrolyte. AGM is made of micro glass fibers. AGM acts as a separator between the positive and negative electrodes and also the electrolyte reservoir [11], [14]. Battery systems in which the electrolyte is immobilized in this way are called AGM type lead-acid batteries. AGM battery technology has been developed as a significant alternative to expensive Ni-Cd batteries used in both naval helicopters

and fighter jets due to its high chemical stability, adaptability to hot weather operation and vibration resistance [18], [19]. In AGM type lead-acid batteries, very thin glass fibers are woven into a mat on the cells to increase the surface area sufficient to hold enough electrolyte for their lifetime. The fibers that make up the thin glass mat do not absorb or are not affected by the acidic electrolyte in which they are located [18], [19]. All AGM batteries have significant performance advantages over conventional flooded lead-acid batteries in terms of performance.

1.1.7 Gel-Type Valve Regulated Batteries (VRLA)

The gel-type VRLA consists of using different gelling agents such as colloidal silica, fumed silica, and some inorganic siloxanes that transform the aqueous electrolyte into a gel form. However, fumed silica offers significant advantages over other systems due to its high thixotropy and ability to form a three-dimensional gel., the sulfuric acid immobilized within the gel electrolyte [20], [21]. As a result of the dispersion of fumed silica, silanol groups form weak hydrogen bonds. If there are strong hydrogen bonds related to the diameter of the silicas, a sol is formed in the system, and if there are weak hydrogen bonds in the silanol, a gel system is formed [22]–[25]. If there is a strong bond between the water molecule and the silanol group, a water layer forms on the silanol surface, and a sol system is formed. The most important parameter that will reveal the sol or gel that the system will form is the existing hydrogen bond strength and therefore the diameter of the silanol groups [25]. If the diameter of the fumed silica is greater than 30 nm, the hydrogen bonds are strong and the formation of a layer of water on the surface is observed. If it is less than 10 nm, isolated silanol groups are formed and the formation of a network structure with weak hydrogen bonds is achieved by gel formation Figure 1.3 [25].

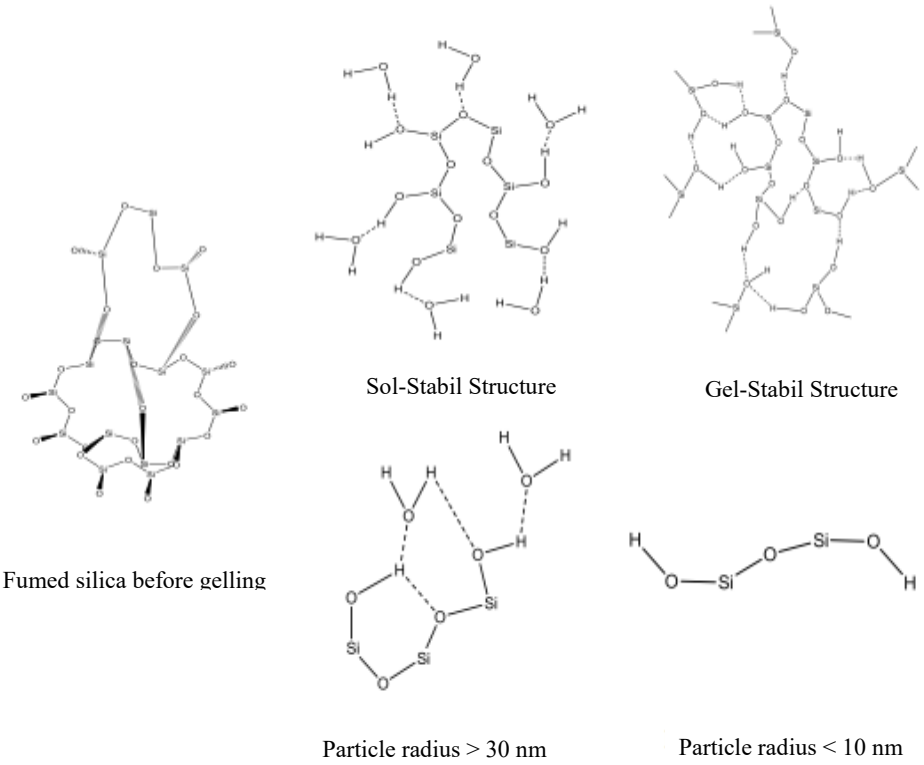


Figure 1.3 Fumed silica gel network

This gel electrolyte has good chemical stability and overcomes the sulfuric acid stratification during usage, but the introduction of fumed silica into the aqueous sulfuric electrolyte increases the medium resistance and decreases the ionic conductivity, the performance of the Gel VRLA battery is directly affected by the filling process of the gel into the battery [14], [26]. In response to these limitations, many researchers have focused on incorporating different additive materials into the gel electrolyte to enhance battery performance. In the literature, some additives have been used to improve the conductivity, gel structure (easy filling process without solidification) and stability of fumed silica-based gel electrolyte. Mansuroglu et al. (2021–2023) studied the effects of three types of additives—N-doped graphene, S-doped graphene, and Cl-doped graphene on the performance of gel-type lead-acid batteries. Their results demonstrated that the additives reduced charge transfer resistance and enhanced battery capacity [27]–[29]. Li et al. (2010) investigated the addition of a siloxane derivative, N-triethoxysilylpropyl 3,4,5-tris(tetradecyloxy) benzamide, into the fumed silica gel electrolyte and its effects on electrochemical behavior during battery operation. The results showed that the gel electrolyte resistance decreased, and the formation of large inorganic crystals was inhibited [25]. Chen et al. (2015) studied the effects of three types of straight-

chain polyols on gel system performance. Their findings indicated that the use of these polyols decreased both charge transfer resistance and stirring time while improving gel behavior [30]. Gencten et al. (2017) investigated the addition of Al_2O_3, TiO_2, and B_2O_3 to the gel electrolyte of lead-acid batteries. They found that the addition of TiO_2 increased the anodic peak and battery capacity by reducing solution and charge transfer resistances. Meanwhile, the addition of Al_2O_3 and B_2O_3 decreased both solution and charge transfer resistances but also reduced anodic peaks and battery capacity [31]. Sari et al. (2025) developed a cellulose-based hydrogel derived from coir fiber as a polymer electrolyte for lead–acid batteries. The study demonstrated improved tensile strength, enhanced electrical conductivity, and increased battery capacity [32]. Chikkatti et al. (2025) reported that the incorporation of montmorillonite into a sodium alginate matrix improved gel properties and resulted in superior battery discharge capacity [33]. Cao et al. (2024) studied the effect of aluminum ion doping in fumed silica-based gel electrolytes, observing increased gel stability and improved electrochemical performance compared to gels without aluminum ions [34]. In another approach, Rajur et al. (2024) examined the use of zirconia nanoparticles as additives in poly(vinyl alcohol) based gels. Their results indicated enhanced conductivity and improved long-cycle discharge capacity [35]. Furthermore, Chikkatti et al. (2023) designed a novel gel system using the sodium salt of poly(4-styrene sulfonic acid-co-maleic acid) blended with poly(vinyl alcohol). Electrochemical characterization demonstrated considerable improvements in battery performance, particularly under galvanostatic cycling [36]. Insinga et al. (2019) compared physically and chemically prepared PVA-based hydrogels for VRLA batteries and found that physically crosslinked hydrogels exhibited better stability and performance [37]. Additionally, Donmez et al. (2017) introduced a polysiloxane-based gel electrolyte and observed enhanced discharge performance when used in VRLA batteries [38]. Yang et al. (2024) examined the effect of incorporating aluminum sulfate into silica gel electrolyte; the findings indicated a reduction in both solution resistance and charge transfer resistance, alongside a positive influence on redox activity. This enhancement is attributed to Al^{+3}, as a result, the capacity and the cycling results were improved [34].

1.1.8 Conductive Polymers CPs

Polymers are known as electrically insulating materials and are widely used in the electrical sector as dielectric coatings for electric cables and electronic devices. However, a class of electroactive organic polymers, known as conductive polymers, exhibit electrical properties comparable to inorganic semiconductors and, in some cases, metal-like electrical conductivity [39], [40]. The development of conductive polymers represents the most important invention in polymer science. In the 1960s, it was discovered that polysulfur nitride (an inorganic polymer) exhibits metallic conductivity at room temperature. Indicating that the polymers can have conductor behavior. The discovery of Alan J. Heeger and his colleagues in 1977 reveals that oxidizing polyacetylene can dramatically enhance its electrical conductivity. Their pioneering work led to the award of the Nobel Prize in Chemistry in 2000 for the discovery and development of conductive polymers [39]–[41]. This event opened the doors for extensive studies on conductive polymers and their applications in sensing, electronics, biotechnology, and recently in electrochemical energy storage systems [42]–[44]. Conductive polymers are characterized by a conjugated backbone structure, consisting of single and double bonds along its chain. The charge carrier mobility is enabled due to the presence of delocalized p-electrons through the polymer backbone [39], [41]. Unlike conventional insulating polymers, conductive polymers can exhibit redox activity, reversible oxidation-reduction processes, and their conductivity can be increased when using the suitable dopant agent during synthesis [39], [40]. The most important category for energy applications is π-conjugated conductive polymers, such as polyacetylene (PA), polyaniline (PANI), polypyrrole (PPy), polythiophene (PTF), and poly(3,4-ethylenedioxythiophene) (PEDOT). These CPs share the same characteristics: conjugated p-electron backbone, reversible redox activity, tunable conductivity via doping/dedoping, and relatively simple synthesis [45], [46]. As a result of the electrical and electrochemical properties of CPs, they are widely used in energy storage systems, supercapacitors, and rechargeable batteries [42], [47]. CPs are synthesized using different methods such as chemical oxidative polymerization, electrochemical polymerization, ultrasonic radiation/ultrasonication, vapor phase polymerization, electrospinning, mechanochemical polymerization, photopolymerization, etc. [40], [41], [44].

1.2 The Aim of the Study

In spite of the high electrochemical properties of lead acid batteries compared to other battery types. The improvement of their overall electrochemical performance becomes a necessity due to the rapid growth of the technological society and its related requirements. Fumed silica is commonly used in the gel electrolyte components of lead-acid batteries. However, the rapid solidification and low stability of the gel formed when only fumed silica is used creates significant problems, especially in terms of charging the battery and using the system efficiently. In addition, when fumed silica is added to the sulfuric acid solution as a gelling agent, an increase in the internal resistance of the electrolyte system occurs. Literature studies show that improvements in important parameters such as gel stability, capacity, and charge-discharge time can be achieved by adding additives to the gel electrolyte component. In this study, for the first time in literature, conductive polymers and conductive polymer composites-based additives will be used for the electrolyte component of gel-type lead-acid batteries, aiming to significantly reduce the electrical resistance of the gel electrolyte component and improve the performance of gel-type lead-acid batteries.

2
EXPERIMENTAL WORK

2.1 Introduction

This chapter describes the materials, preparation methods, and experimental procedures employed in this study. It outlines the synthesis routes, electrolyte preparation, and characterization techniques used to investigate the structural, thermal, morphological, and electrochemical properties of the prepared samples. All experiments were conducted under controlled conditions to ensure reproducibility and reliability of the results.

2.1.1 Materials

The experimental work was carried out using commercially available analytical-grade materials. Aniline (99%) and thiophene (≥99%) supplied by Sigma-Aldrich, and pyrrole (>99%) obtained from TCI Chemicals, were used as monomers for conductive polymer synthesis. Ferric chloride hexahydrate (≥99%) was purchased from Chemsolute and employed as the oxidizing agent. Fumed silica (SiO_2, 99.8%) supplied by Aldrich was used as the gelling material, while commercial graphite was incorporated as a conductive additive. Sulfuric acid (95–98%) and hydrochloric acid (37%) were obtained from ISOLAB and used for electrolyte preparation and protonation, and hydrogen peroxide (30%) was used as required. All materials were used as received without further purification.

2.1.2 Synthesis of Conductive Polymers CP's and Conductive Polymers/Graphite Composites

In this study, the conductive polymers (polyaniline (PANi), polyaniline/graphite composite (PANi/G), polythiophene (PTF), polythiophene/graphite composite (PTF/G) and polypyrrole (PPy)) were synthesized using the chemical oxidative polymerization method, a simple and cost-effective approach commonly employed

in polymer synthesis [44], [46], [48]. The CP's synthesis process was carried out in two distinct stages to optimize the polymer's electrical conductivity and other material properties. The first stage consists of mixing in reaction flask constant amount of acid and oxidant agent with 500 rpm stirring rate and heated up to (80 - 70)^{o}C (**according to conductive polymer type**) then different amount of monomer (**according to monomer type**) were added to the mixture the polymerization reaction was allowed to proceed for (5-3) hours, the reacted solution then filtered and washed with water several times until removing the residuals and unreacted materials, then dried in furnace for 48h with varied drying temperatures according to the type of monomer. The second step consists of mixing iron chloride hexahydrate with different concentrations of acid under constant stirring rate and temperature (**same as step 1**), the aim was to investigate the effect of sulfuric acid concentration on the electrical conductivity and morphology of CPs. To initiate polymerization process, the optimum value of monomer was added, and the reaction allowed to proceed for several hours. The resulting product was then filtrated, washed, and dried to obtain the conductive polymer powder. The properties of the synthesized CP's and CP's/G composites powders were thoroughly characterized using several analytical techniques. The surface area and pore structure were analyzed using Brunauer-Emmett-Teller (BET) analysis, while the morphology and structure were examined using scanning electron microscopy (SEM) and field emission scanning electron microscopy (FESEM). The chemical structure and functional groups of the CPs and CP's/G composites were investigated through Fourier transform infrared spectroscopy (FTIR). Electrical conductivity measurements were also performed to assess the conductive properties of the synthesized CPs and CP's/G composites, Four Point Probe Method was performed to measure the electrical resistivity of each synthesized CPs and CP's/G composites powders. The electrical conductivity was defined as the key factor for choosing the optimum values of monomers and acids concentrations [28], [29]. Figure 1. Shows the synthesizing and characterization process of conductive polymers that were used in this study.

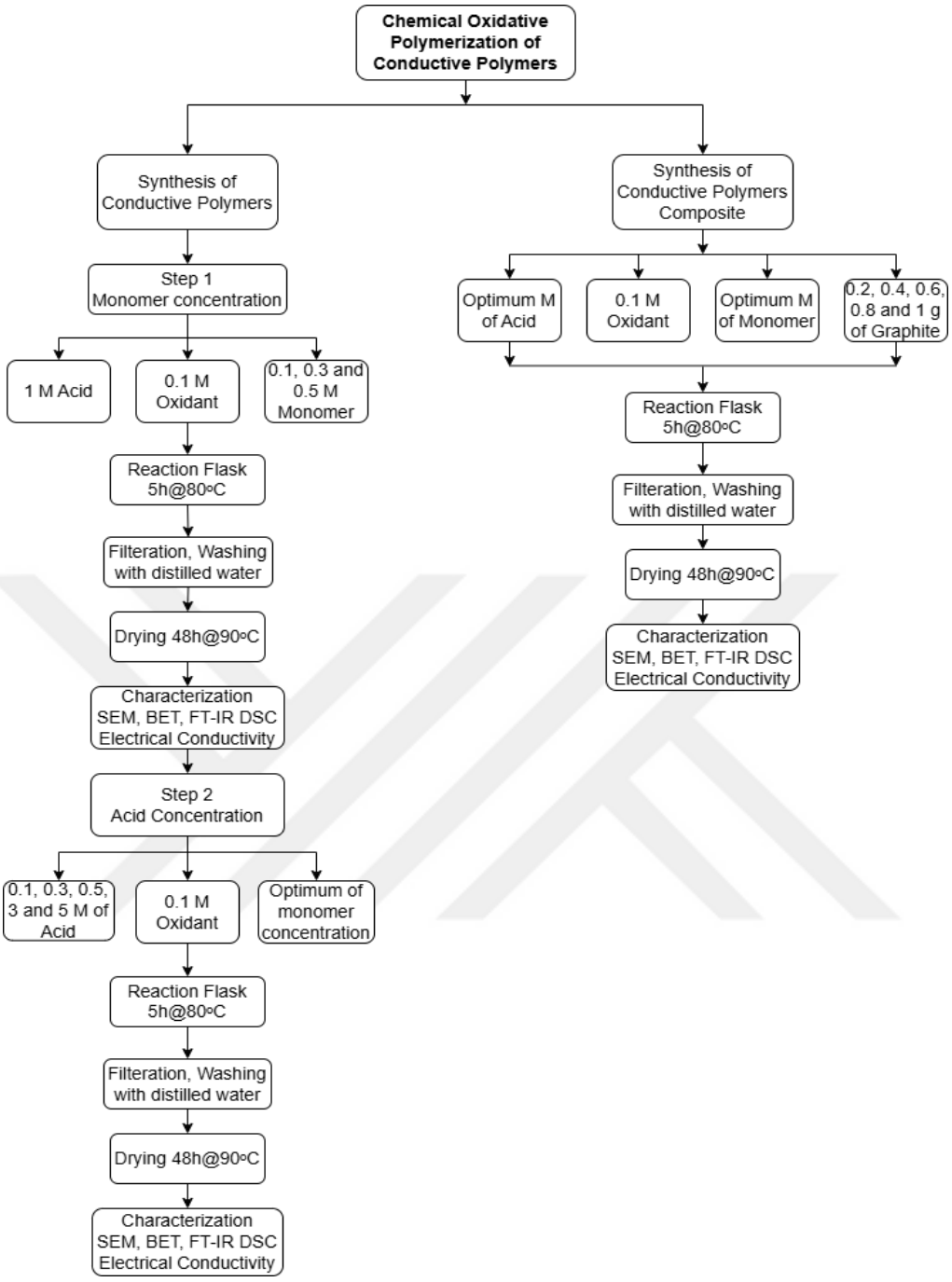


Figure 2.1 Schematic of synthesizing process and characterizations of different CPs

2.1.2.1 Synthesis of Polyaniline (PANi), Polypyrrole (PPy), and Polyaniline/Graphite Composite (PANi/G)

Polyaniline (PANi), polyaniline/graphite composite (PANi/G), and polypyrrole (PPy) were synthesized via chemical oxidative polymerization using ferric chloride hexahydrate ($FeCl_3.6H_2O$) as the oxidizing agent and sulfuric acid as the dopant. For PANi synthesis, 1 M of H_2SO_4 and 0.1 M $FeCl_3.6H_2O$ were mixed in reaction

flask that heated up to 80°C and stirred at 500 rpm [49], followed by the addition of different aniline monomer concentrations (0.1, 0.3 or 0.5 M). After 5 h of reaction, the product was filtered, washed with distilled water several times, then dried at 90°C for 48 h. The sample with the lowest electrical resistivity was selected for the second stage, which involved optimizing varying sulfuric acid concentrations (0.1, 0.3, 0.5, 1, 3, and 5 M) under the same reaction conditions. For PPy synthesis, the same procedure of PANi was used with one difference: the reaction temperature. The oxidant and dopant were mixed in a reaction flask up to 70°C [50] then the pyrrole monomer was added to the mixture, and the reaction continued for 3 h. Then the produced polymer was filtered, washed, and dried at 90°C for 48 hours [49], [51]. The second stage was conducted using the optimum monomer concentration and varying sulfuric acid concentrations. PANi/G composite was synthesized using the optimum concentrations of aniline monomer and sulfuric acid via the exact procedure; after adding the monomer, different amounts of graphite powder were added during the polymerization process, and the produced powder was filtered, washed, and dried at 90°C for 48 hours. Table 2.1, 2.2, and 2.3. shows the synthesis parameters of polyaniline, polypyrrole, and polyaniline/graphite composite with varying monomers and acid concentrations. These parameters were optimized based on the desired conductivity and material properties.

Table 2.1 Polyaniline synthesis parameters with different concentrations of monomers and acid

Sample Name	Monomer concentration / M	Acid concentration / M	Synthesizing time/hr.	Stirring rate/rpm	Reaction temp./°C	Drying temp. / °C
P01_1	**0.1**	**1**	**5**	**500**	**80**	**90**
P03_1	**0.3**	**1**	**5**	**500**	**80**	**90**
P05_1	**0.5**	**1**	**5**	**500**	**80**	**90**

Table 2.1 Polyaniline synthesis parameters with different concentrations of monomers and acid "continued"

Sample Name	Monomer concentration / M	Acid concentration / M	Synthesizing time/hr.	Stirring rate/rpm	Reaction temp./°C	Drying temp. / °C
P03_01	0.3	0.1	5	500	80	90
P03_03	0.3	0.3	5	500	80	90
P03_05	0.3	0.5	5	500	80	90
P03_3	0.3	3	5	500	80	90
P03_5	0.3	5	5	500	80	90

Table 2.2 Polypyrrole synthesis parameters with different concentrations of pyrrole monomer and sulfuric acid

Sample Name	Monomer concentration/M	Acid concentration/M	Synthesizing time/hr.	Stirring rate/rpm	Reaction temp./ ^{o}C	Drying temp./ ^{o}C
PPy01_1	0.1	1	3	500	70	90
PPy03_1	0.3	1	3	500	70	90
PPy05_1	0.5	1	3	500	70	90
PPy03_01	0.3	0.1	3	500	70	90
PPy03_05	0.3	0.1	3	500	70	90
PPy03_3	0.3	0.1	3	500	70	90
PPy03_5	0.3	0.1	3	500	70	90

Table 2.3 Polyaniline/graphite composite synthesis parameters with different graphite powder additive

Sample Name	Monomer/Acid concentration/ M	Graphite weight/ g	Synthesizing time/hr.	Stirring rate/rpm	Reaction temp./°C	Drying temp. / °C
PG_02	**0.3/3**	**0.2**	**5**	**500**	**80**	**90**
PG_04	**0.3/3**	**0.4**	**5**	**500**	**80**	**90**
PG_06	**0.3/3**	**0.6**	**5**	**500**	**80**	**90**
PG_08	**0.3/3**	**0.8**	**5**	**500**	**80**	**90**
PG_1	**0.3/3**	**1.0**	**5**	**500**	**80**	**90**

2.1.2.2 Synthesis of Polythiophene (PTF)

Polythiophene was synthesized by polymerizing thiophene monomer (C_4H_4S) through chemical oxidative method [52]. The synthesis process consists of mixing 0.5 M hydrochloric acid and 0.1 M $FeCl_3.6H_2O$ in reaction flask with fixed stirring rate 500 rate and raising the temperature 80°C then different concentrations (0.1, 0.3, 0.5 and 1 M) of thiophene monomer were added into the solution, the polymerization was initiated with the addition of 3 ml of hydrogen peroxide and the reaction continues for 5h, the solution were filtered and washed with water and methanol several times until removing the unreacted residuals then dried in furnace for 48h at 70°C the dried powder were characterized to obtain the sample with the best electrical properties. The second step was carried out using 0.1 M $FeCl_3.6H_2O$

with different HCl acid concentrations (0.1, 0.3, 0.5, 0.7 and 1 M) the mixture stirred with 500 rpm at 80°C then the optimum concentration of thiophene were added, a few minutes later 3 ml of H_2O_2 added to start the polymerization of thiophene monomer. The product filtered and washed with distilled water and methanol to remove the by-products and dried in furnace for 48h at 70°C, then the produced powder characterized to obtain the optimum sample. Table 2.4 shows the procedure parameters.

Table 2.4 Polythiophene synthesis parameters with different concentrations of thiophene monomer and hydrochloric acid.

Sample Name	Monomer concentration/M	Acid concentration/M	Synthesizing time/hr.	Stirring rate/rpm	Reaction temp./ °C	Drying temp./ °C
PT01_05	0.1	0.5	5	500	80	70
PT03_05	0.3	0.5	5	500	80	70
PT03_05	0.5	0.5	5	500	80	70
PT1_05	1	0.5	5	500	80	70
PT05_01	0.5	0.1	5	500	80	70
PT01_03	0.5	0.3	5	500	80	70

Table 2.4 Polythiophene synthesis parameters with different concentrations of thiophene monomer and hydrochloric acid "continued".

Sample Name	Monomer concentration/M	Acid concentration/M	Synthesizing time/hr.	Stirring rate/rpm	Reaction temp./ ^{o}C	Drying temp./ ^{o}C
PT01_07	0.5	0.5	5	500	80	70
PT01_1	0.5	1	5	500	80	70

2.1.2.3 Synthesis of Polythiophene/Graphite Composite (PTF/G)

The synthesis of PTF/Graphite composite was performed using the optimum sample of synthesized polyaniline with the addition of graphite powder. The process was performed by mixing the optimum concentration of HCl and 0.1 M of $FeCl_3.6H_2O$ were stirred with 500 rpm and maintain the reaction temperature at 80^{o}C, after getting homogenous solution, then the optimum concentration value of thiophene monomer were added to the solution the polymerization was initiated by adding 3 ml of H_2O_2 to the solution then different weight of graphite powder (0.2, 0.4, 0.6, 0.8 and 1 g) were added to the reaction flask, the reaction were maintained for 5h then filtered and washed with water and methanol for several time to remove unreacted products and dried at 70^{o}C for 48h. Same characterization techniques were performed for the analysis of PTF/G composite properties.

Table 2.5 Polythiophene/graphite composite synthesis parameters with different graphite powder additive.

Sample Name	Monomer/Acid concentration /M	Graphite weight/ g	Synthesizing time/hr.	Stirring rate/rpm	Reaction temp./^{o}C	Drying temp. / ^{o}C
PTFG_02	**0.5/0.5**	**0.2**	**5**	**500**	**80**	**70**
PTFG_04	**0.5/0.5**	**0.4**	**5**	**500**	**80**	**70**
PTFG_06	**0.5/0.5**	**0.6**	**5**	**500**	**80**	**70**
PTFG_08	**0.5/0.5**	**0.8**	**5**	**500**	**80**	**70**
PTFG_1	**0.5/0.5**	**1.0**	**5**	**500**	**80**	**70**

2.1.3 Characterization of Conductive Polymers and Conductive Polymers/Graphite Composite

The chemically synthesized conductive polymers and their corresponding conductive polymer/graphite composites were comprehensively characterized to evaluate their structural, morphological, and electrical properties. A suite of advanced spectroscopic and microscopic techniques was employed to gain in-depth insight into the materials' composition, molecular structure, surface morphology, and potential electrochemical performance. These analyses included Fourier-transform infrared spectroscopy (FTIR), scanning electron microscopy (SEM), thermogravimetric analysis (TGA), and Brunauer–Emmett–Teller (BET) surface

area measurements, among others. All characterization processes were conducted using state-of-the-art instrumentation available at the Central Research Laboratory of Yildiz Technical University and the Eastern Anatolia High Technology Application and Research Center (DAYTAM) at Ataturk University. This multi-facility approach ensured high reliability and precision in evaluating the physicochemical and functional characteristics of the synthesized materials.

2.1.3.1 Electrical Conductivity (EC)

The electrical resistivity of the synthesized powders, prepared using varying concentrations of monomers and acids, was evaluated using the Four-Point Probe method. Measurements were conducted with a JANDEL model RM3-AR system, which provides high accuracy in determining resistivity and conductivity of thin films and powdered materials. This technique enabled precise assessment of the electrical properties of the conductive polymer and polymer/graphite composite samples, offering valuable insights into the influence of synthesis conditions on their conductive behavior.

2.1.3.2 Fourier-Transform Infrared Spectroscopy (FT-IR)

The chemical structure and functional groups of the synthesized conductive polymers (CPs) and conductive polymer/graphite (CPs/G) composites were analyzed using Fourier-transform infrared (FTIR) spectroscopy. This technique provided detailed information on the molecular bonding and functional group distribution within the samples. The FTIR measurements were performed using a PerkinElmer Spectrum 100 spectrometer, enabling the identification of characteristic peaks associated with specific chemical bonds. This analysis was essential for confirming successful polymerization and evaluating interactions between the polymer matrix and graphite particles.

2.1.3.3 Differential Scanning Calorimetry and Thermogravimetric Analysis DSC-TGA

The thermal properties and stability of the synthesized conductive polymers (CPs) and conductive polymer/graphite (CPs/G) composites were investigated using a NETZSCH STA 449F3 simultaneous thermal analyzer. This technique combines Differential Scanning Calorimetry (DSC) and Thermogravimetric Analysis (TGA) to provide comprehensive thermal characterization of the materials under controlled

heating conditions. The analysis offered valuable insights into the overall thermal behavior and structural integrity of the samples, supporting their evaluation for potential use in energy storage and electronic applications.

2.1.3.4 Brunauer, Emmett ve Teller (BET)

The surface area and pore structure characteristics of the synthesized conductive polymers (CPs) and conductive polymer/graphite (CPs/G) composites were analyzed using the Brunauer–Emmett–Teller (BET) method. This analysis was performed to evaluate how variations in monomer and acid concentrations during synthesis influence the textural properties of the materials. The nitrogen adsorption–desorption measurements were conducted using Micromeritics ASAP 2020 and instrument. BET analysis provided essential information on specific surface area, pore volume, and pore size distribution, which are critical factors affecting the electrochemical performance and capacitive behavior of the materials in energy storage applications.

2.1.3.5 Field Emission Scanning Electron Microscopy (EF-SEM) and Scanning Electron Microscopy (SEM)

The morphological and structural features of each synthesized conductive polymer (CP) and conductive polymer/graphite (CPs/G) composite were examined using Scanning Electron Microscopy (SEM) to assess the impact of varying monomer and acid concentrations. These structural investigations aimed to provide a clearer understanding of how synthesis parameters influence the surface texture, particle distribution, and network formation of the materials, which are closely related to their electrochemical performance in gel electrolyte optimization. High-resolution imaging was performed using a Zeiss EVO LS10 and a Thermo Scientific Apreo 2 S LoVac SEM system, both of which allowed for detailed visualization of surface morphology at micro and nanoscale levels.

2.1.4 Preparation of Gel Electrolyte

The base gel electrolyte was prepared using a 30 wt% sulfuric acid solution (Sigma-Aldrich, 95–98%) as the electrolyte medium. To 100 mL of this solution, 6 wt% fumed silica (7 nm, Sigma-Aldrich), based on the total mass, was gradually added under continuous magnetic stirring. The mixture was stirred for 30 minutes at 500 rpm to ensure uniform gel formation. This formulation was used as the base fumed

silica gel electrolyte for comparison [53]. To improve the gel electrolyte system with different amounts of CPs and CPs/G composites, a step-by-step experimental method was used. First, fumed silica (6 wt%) and different amounts of CPs and CPs composites (from 0.2 to 1.0 wt% based on the total gel mixture) were added at the same time to 100 mL of the 30 wt% H_2SO_4 solution. In the first step, six samples were prepared by changing only the CPs and CPs composites content while keeping the stirring speed and time fixed. This was done to find the best concentration of CPs and CPs composites. In the second step, the best CPs or CPs composite content from the first step was used, and the stirring time was changed (15, 30, 60, 90, 120, and 150 minutes), while the stirring speed stayed the same. In the third step, the stirring speed (250, 500, 750, and 1000 rpm) was changed, using the best CPs or CPs composite content and stirring time found earlier. This method helped identify the best combination of conditions without testing every possible mix (Table 2.6). The gels were prepared, and measurements were taken after letting them sit for 30 minutes. All preparation steps were done at room temperature. The goal was to find the best CPs or CPs composite amount, stirring time, and speed to reduce internal resistance, improve ion movement, and increase the electrochemical performance of the gel electrolyte. Also, a reference solution of just 30 wt% sulfuric acid was prepared and tested for comparison [29], [53].

Table 2.6 Preparation conditions for aqueous electrolyte, fumed silica-based gel electrolyte, and PANi-added fumed silica-based gel electrolytes

Sample Designation	**Electrolyte Medium**	**Fumed Silica Content (wt%)**	**Additive Content (wt%)**	**Stirring Speed (rpm)**	**Stirring Duration (min)**
Aqueous electrolyte*	30 wt% sulfuric acid solution	-	-	-	-
Fumed silica-based gel electrolyte (FS)**	30 wt% sulfuric solution	6	-	500	30
CP's, CP's/G composite-added fumed silica-based gel electrolyte (CP's, CP's/G composite-GEs) ***	30 wt% sulfuric solution	6	0.2, 0.4, 0.6, 0.8 and 1.0	250, 500, 750, and 1000	15, 30, 60, 90, 120, and 150

* Aqueous electrolyte for baseline comparison

** Bare fumed silica-based gel electrolyte for baseline comparison

*** The gel electrolytes are prepared by varying conductive polymers or conductive polymers graphite composite content and stirring conditions, providing a range of formulations for comparison.

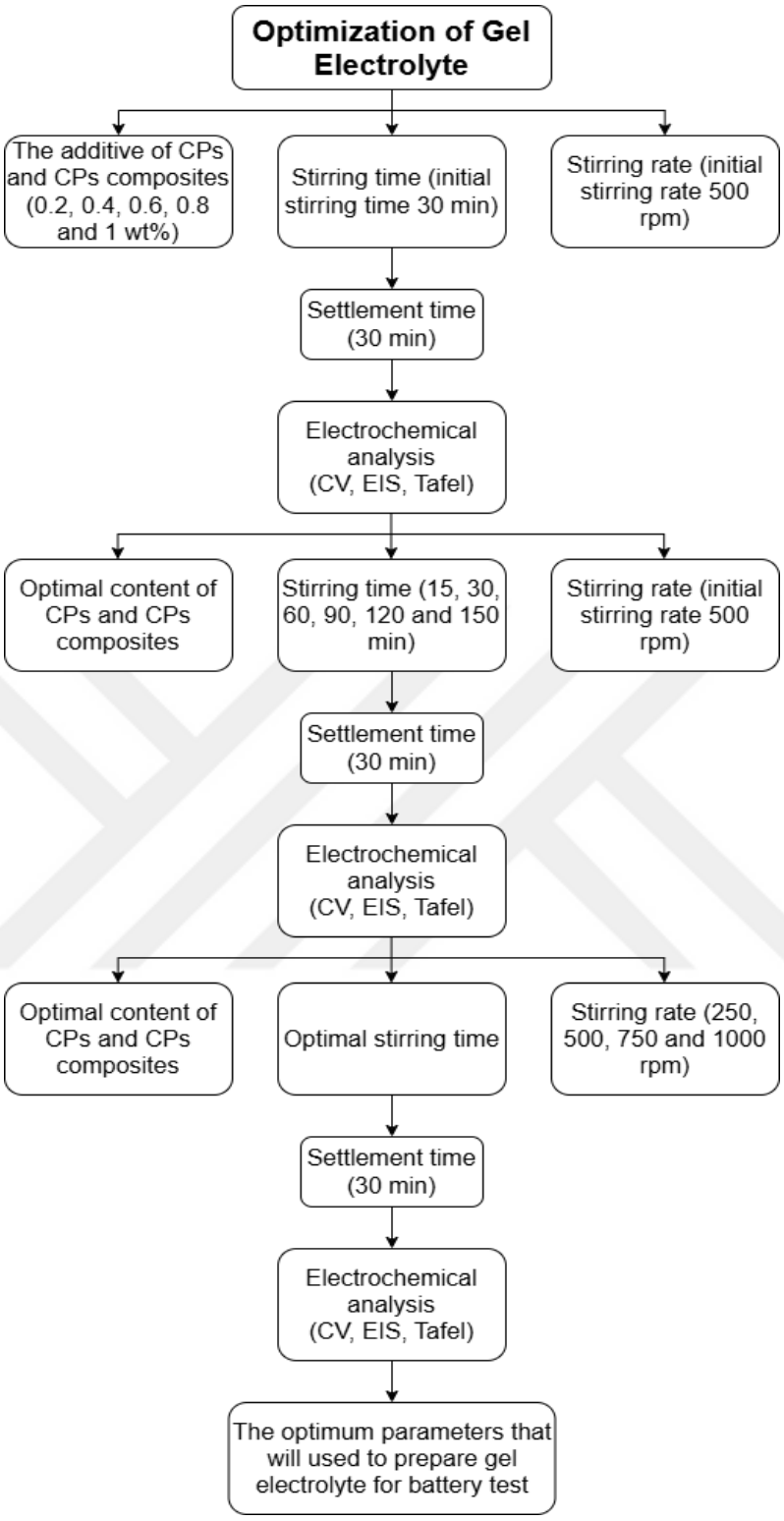


Figure 2.2 Schematic of gel preparation and optimization with different parameters

2.1.5 Electrochemical Characterization of Gel Electrolytes

Electrochemical characterization plays a critical role in evaluating the performance and stability of gel electrolytes used in lead–acid battery systems. In this study, a combination of cyclic voltammetry (CV), electrochemical impedance spectroscopy (EIS), and Tafel analysis were employed to assess the redox behavior, ion transport properties, and corrosion resistance of both the bare and conductive polymer-modified gel electrolytes. These techniques offer a comprehensive understanding of the electrochemical processes occurring at the electrode–electrolyte interface. All measurements were conducted at room temperature using a standard three-electrode setup and a Gamry Interface 1010B Potentiostat/Galvanostat [28], [53].



Figure 2.3 Gamry interface 1010b potentiostat/galvanostat

2.1.5.1 Cyclic Voltammetry (CV)

Cyclic voltammetry is a widely used technique to study the redox reactions and electrochemical reversibility of electrode processes. It helps identify the oxidation and reduction peaks of active species and assess the influence of the gel matrix on charge storage behavior. In this work, metallic lead electrodes with a geometric surface area of 0.5 cm^2 were used as both the working electrode and counter electrode, while a saturated calomel electrode (SCE) served as the reference electrode. The potential was scanned in the range of –1.0 V to 0 V vs. SCE, which corresponds to the typical redox window of lead in sulfuric acid media. This range

was selected to ensure safe operation and to avoid water electrolysis, while capturing the key redox processes related to $Pb/PbSO_4$ transitions in the system.

2.1.5.2 Electrochemical Impedance Spectroscopy (EIS)

EIS is a powerful tool for analyzing internal resistance and ion transport efficiency within gel electrolyte systems. It provides information on bulk resistance, charge transfer resistance, and double-layer capacitance, which are essential for understanding the ionic conductivity and interfacial properties of the gel. In this study, EIS measurements were performed at the open-circuit potential (OCP) using the same electrode configuration as CV. The frequency range was set from 0.1 Hz to 10,000 Hz, and a 10 mV AC voltage amplitude was applied relative to the SCE. The data obtained were used to evaluate the impedance behavior of each electrolyte formulation and to compare the effect of CPs and CPs/G composites on reducing resistance and enhancing ionic movement. Obtained spectra were fitted using an equivalent circuit model given in Figure 2.4. The error rate in fitting process was lower than that of 1%.

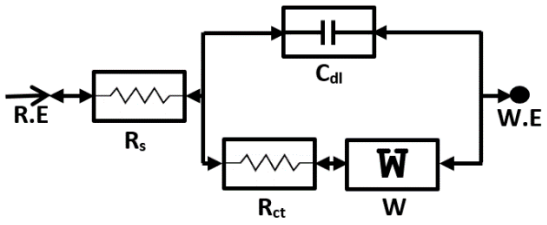


Figure 2.4 Gamry interface 1010b potentiostat/galvanostat

2.1.5.3 Tafel Analysis

Tafel polarization analysis was conducted to assess the corrosion behavior of the gel electrolytes, particularly with respect to the negative lead electrodes. This method is useful for determining corrosion potential, corrosion current density, and the kinetics of electrochemical reactions. For this analysis, the potential was scanned from –0.8 V to 0.0 V vs. SCE at a scan rate of 1 $mV \cdot s^{-1}$. The results were interpreted using the Tafel extrapolation method, which provides insights into the electrochemical stability of the electrolyte formulations. This is particularly

important in understanding how conductive polymer additives influence the corrosion resistance of lead electrodes in gel environments.

2.1.5.4 Battery Test

Galvanostatic charge-discharge tests (GCDTs) were carried out for the non-gelled (aqueous) electrolyte, the bare fumed silica-based gel electrolyte (FS), and the optimized conductive polymers CPs and its composites-doped gel electrolyte. The tests were conducted within a voltage range of 1.75–2.35 V, using a charge/discharge current density of 5 mA/g, based on the weight of the negative active material (NAM). A long-cycle test was also performed using a voltage range of 2.3–1.85 V at a current density of 10 mA/g (NAM-based). The tests were conducted on a single-cell battery made up of 4 Pb electrodes and 3 PbO_2 electrodes taken from a commercial battery, separated by commercial polyethylene micro-separators and placed in a glass cell. GCDTs were performed using a NEWARE-4000 battery testing system. All tests were carried out at room temperature. [29], [53].



Figure 2.5 NEWARE-4000 multichannel testing system

3
RESULTS AND DISCUSSION

3.1 Introduction

This chapter presents and discusses the experimental results obtained during the course of this study. The results are systematically organized according to the objectives of the work and the methodologies employed, providing a clear link between the experimental findings and the scientific principles. Each set of results is analyzed in detail to evaluate the influence of key parameters on the material properties and performance, and to evaluate their consistence with theoretical expectations and reported literature studies. The discussion integrates data observations to explain the electrochemical behavior of different gel systems with different additives. The analysis allows coherent interpretation of the data to give a clear and deeper understanding of the relationship between structure, gel preparation parameters, and optimization, as well as synthesis optimization.

3.2 Characterization Analysis Tests

This section presents the characterization analyses carried out to investigate the structural, morphological, thermal, surface, and electrical properties of the prepared samples. Fourier-transform infrared spectroscopy (FT-IR) was used to identify functional groups and confirm chemical interactions, while BET analysis provided information on specific surface area and porosity. Thermal stability and decomposition behavior were evaluated using DSC-TGA. The surface morphology and microstructural features were examined by SEM and FE-SEM. In addition, electrical conductivity measurements were performed to assess the charge-transport characteristics of the materials. Together, these techniques provide a

comprehensive understanding of the material properties relevant to their electrochemical performance.

3.2.1 Fourier-Transform Infrared Spectroscopy (FT-IR)

Figure 3.1 shows the FT-IR results of CPs and CPs/composites. Figure 3.1a shows the FTIR spectra of PANi and PANi/G. The black line represents the spectrum of PANi, confirming the successful formation of the emeraldine salt form, which is the most conductive oxidation state of polyaniline. The peaks observed at 1566 cm^{-1} and 1490 cm^{-1} correspond to the quinoid and benzenoid C=C stretching vibrations, respectively. These bands indicate the alternating structure of the polymer backbone, which is essential for effective electron delocalization along the chains. This alternation between quinoid and benzenoid rings plays a crucial role in enhancing the electrical conductivity of PANi by facilitating charge transfer. The peak at 1443 cm^{-1} suggests the presence of ortho-coupled aniline units and possibly phenazine-like structures. While these structures are beneficial for polymerization, they may slightly disrupt the regularity of the polymer chain, potentially affecting conductivity; however, these disruptions are minimal, and the overall structure remains conducive to electron movement. The band at 1288 cm^{-1} is attributed to C–N stretching in benzenoid rings, while the strong band at 1128 cm^{-1} corresponds to protonated $C–N^+$ groups. The presence of these protonated sites is a clear indicator of doping, which is essential for the conductive properties of PANi. The degree of doping directly influences the polymer's conductivity, and a higher intensity of the 1128 cm^{-1} band typically reflects better doping efficiency, leading to improved charge transport and overall electrochemical performance. Additionally, the broad absorption around 3228 cm^{-1} is related to N–H stretching and surface-adsorbed OH groups, indicating the presence of residual water or functional groups that may influence electrolyte interaction without significantly affecting conductivity [54]–[59]. The blue line in the same figure represents the FTIR spectrum of the PANi/G composite, which also confirms the formation of the conductive emeraldine salt structure. Key peaks at 1567 cm^{-1} and 1497 cm^{-1} are associated with quinoid and benzenoid C=C stretching vibrations, respectively, indicating that the alternating conjugated structure is preserved. The band at 1443 cm^{-1} again suggests the presence of ortho-coupled aniline units or phenazine-like structures, while the peak at 1291 cm^{-1} is attributed to C–N stretching in benzenoid rings. Peaks at 994 cm^{-1}

and 732 cm^{-1} correspond to aromatic C–H bending vibrations and may reflect interactions with the graphite surface. A broad absorption band between 3231 and 3432 cm^{-1}, along with a weak peak at 3783 cm^{-1}, is attributed to N–H and O–H stretching vibrations, suggesting the presence of residual moisture and surface functional groups likely introduced by graphite, which can enhance compatibility with electrolytes. Additionally, the weak band at 2350 cm^{-1} is likely due to adsorbed atmospheric CO_2, which is common in FTIR spectra and does not affect material structure [60]–[65]. Overall, the FTIR spectrum confirms the successful incorporation of graphite into PANi without disrupting its backbone structure. The observed shifts and additional bands suggest π–π interactions and improved structural integrity, supporting the enhanced electrochemical performance of the composite in applications such as batteries. Figure 3.1b displays the FTIR spectra of PTF (black line) and PTF/G (blue line), confirming the successful polymerization of polythiophene and its composite formation with graphite. In the PTF spectrum, the peaks at 605, 793, and 992 cm^{-1} are attributed to C–S–C deformation and C–H bending vibrations within the thiophene ring, indicating the integrity of the heterocyclic structure. The band at 1215 cm^{-1} corresponds to C–C and C–H in-plane deformation vibrations, while the sharp band at 1385 cm^{-1} is due to symmetric stretching of the thiophene ring. A prominent absorption at 1675 cm^{-1} is associated with C=C stretching in conjugated thiophene units, confirming π-conjugation critical for electrical conductivity. The broad bands observed at 2925 and 3067 cm^{-1} represent aliphatic C–H stretching vibrations, while the band at 3437 cm^{-1} corresponds to O–H stretching from adsorbed water or surface hydroxyl groups [52], [66]–[69]. In the PTF/G spectrum, the characteristic bands are retained with slight shifts, supporting the structural stability of the polymer upon graphite incorporation. Notably, the C=C stretching shifts slightly to 1678 cm^{-1}, and a new peak at 1037 cm^{-1} appears, possibly indicating C–O or C–S interactions influenced by graphite. The 1384 cm^{-1} band, close to the original 1385 cm^{-1} in PTF, suggests preserved ring vibrations, while the 2919 and 3428 cm^{-1} bands indicate retained C–H and O–H stretching. These changes, along with the increased broadness and subtle shifts, suggest π–π stacking and interfacial interactions between PTF chains and graphite layers [69]–[72]. Overall, the FTIR data confirm that the PTF/G composite maintains the essential structural and conductive features of PTF while gaining additional surface functionality and interaction sites from graphite, which

can enhance charge transport and electrochemical performance in energy storage applications. Figure 3.1c shows the FTIR spectrum of PPy. The band at 3413 cm^{-1} represents the N-H stretching vibration, while the band at 1561 cm^{-1} corresponds to C=C stretching. The presence of the C-H stretching bond is observed at 927 cm^{-1}, indicating the reaction of PPy, and the band at 1206 cm^{-1} is attributed to N-C stretching. Moreover, the small peaks observed in the 621–790 cm^{-1} are likely associated with C–H out-of-plane bending and deformation of the pyrrole ring. These signals further confirm the polymerization of pyrrole and support the structural characteristics of the resulting polypyrrole [73]–[75].

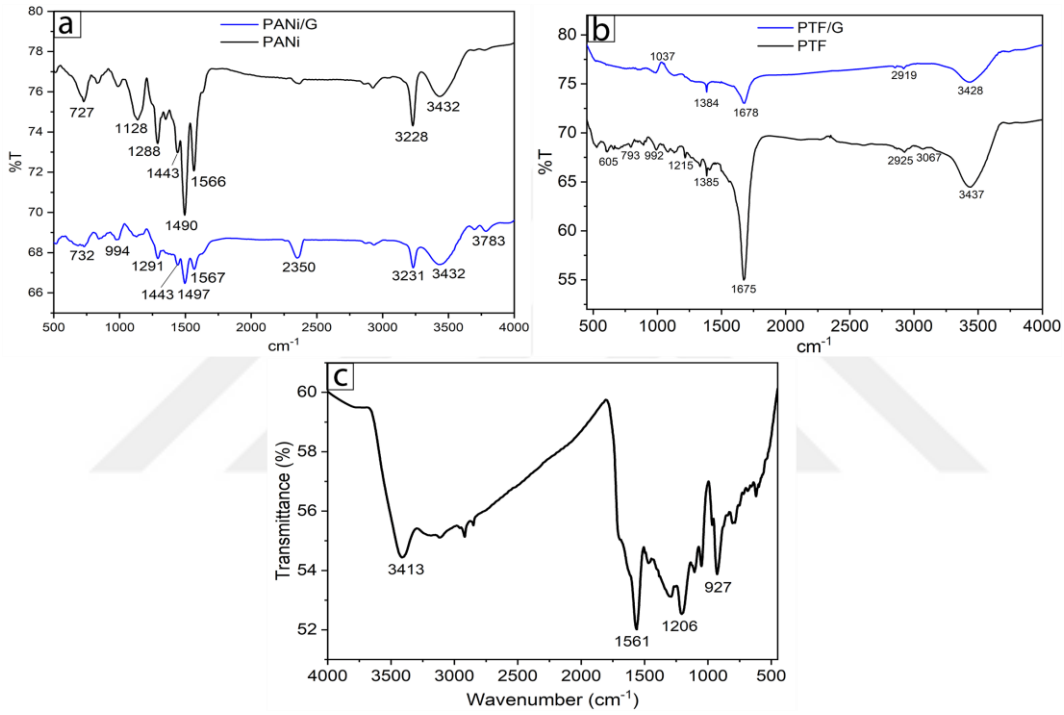


Figure 3.1 FT-IR test of conductive polymers and conductive polymers/composites. a) represents PANi and PANi/G composite. b) represents PTF and PTF/G composite. c) represents PPy.

3.2.2 Electrical Conductivity (EC)

Figure 3.2. illustrates the electrical resistivity variations of PANi, PANi/graphite composite, PTF, and PTF/graphite composite and PPy under different synthesis conditions. For PANi (Figures 3.2a and 3.2b), the aniline monomer concentration and sulfuric acid molarity significantly influenced conductivity. The sample synthesized with 0.3 M aniline and 1 M H_2SO_4 exhibited the lowest resistivity (12.63 mΩ·cm), indicating optimal polymer chain growth and effective doping.

Lower monomer concentration (0.1 M) resulted in incomplete polymerization, while higher concentration (0.5 M) likely led to structural disorder, both causing increased resistivity. Increasing sulfuric acid concentration to 3 M further reduced resistivity to 12.37 mΩ·cm due to enhanced protonation and doping efficiency, whereas synthesis failed at 5 M H_2SO_4 because over-protonation inhibited polymerization. In the PANi/graphite composite (Figure 3.2c), resistivity sharply decreased with graphite addition [60], [61], [63], [65], reaching a minimum of 0.205 mΩ·cm at 0.8 g due to the formation of conductive pathways and improved charge transport; a slight increase at 1.0 g (0.227 mΩ·cm) may result from graphite aggregation [76]. For PTF (Figures 3.2d and 3.2e), At low TF concentrations (0.1 M), the conductivity is low due to the lack of monomer availability, which causes the propagation restriction of polymer chains, resulting in disordered and shorter structures with poor electrical conductivity. By increasing thiophene concentration to 0.3 M, an increase in the electrical conductivity was recorded, meaning that the presence of a higher thiophene concentration during the polymerization process leads to better protonation and improves the polymer matrix. On the other hand, the higher the monomer concentration (1.0 M), the more aggregated and irregular the polymer matrix caused by excessive and uncontrolled polymerization, which leads to hindered charge mobility [77], [78]. An electrical resistivity of 4.74 mΩ·cm was obtained at 0.5 M of both thiophene monomer and HCl acid concentrations, which indicates that this combination provides suitable polymerization conditions for polymer chain growth and effective doping during the process. As shown in Figure 3.2b, the synthesis of polythiophene polymer using different concentrations of HCl acid plays a key role in controlling the doping level of polythiophene polymer chains. The results show similar behavior as noticed when using different concentrations of thiophene monomer; the lowest acid concentration (0.1 M) used during polymerization leads to under-doping and insufficient conductivity, while excessive acid (1.0 M) causes over-protonation, resulting in chain disorder and defects. Such defects may lead to hindrance, which lowers electron transport efficiency. In the case of the PTF/graphite composite (Figure 3.2f), the addition of graphite significantly reduced the resistivity from 3.79 mΩ·cm (at 0.2 g graphite) to 0.954 mΩ·cm at 0.6 g, due to the formation of a more continuous and interconnected conductive network within the polymer matrix [66]. This improvement is attributed to the excellent electrical conductivity of graphite and its

ability to bridge gaps between PTF chains, thus enhancing the percolation pathway for charge carriers. Beyond 0.6 g of graphite, the resistivity values remained relatively stable (0.92–0.982 mΩ·cm), indicating that a percolation threshold had been reached. Additional graphite at higher loadings does not further improve conductivity, likely due to saturation of conductive sites or minor agglomeration that offsets further benefits. These findings collectively demonstrate that both precise control of synthesis parameters and judicious use of conductive fillers are essential for optimizing the electrical performance of polythiophene-based systems [70], [71]. For PPy (Figures 2g and 2h), the electrical resistivity of various pyrrole monomer concentrations, the sample with 0.3 M pyrrole has the lowest electrical resistivity, and therefore the highest electrical conductivity, compared to the other samples (0.1 M and 0.5 M). This may result from excessive oxidation of the PPy generated by both low and high concentrations of pyrrole in the presence of $FeCl_3.6H_2O$, which interrupts the conjugation due to carbonyl defects. These defects hinder electron delocalization along the polymer chain, leading to decreased electrical conductivity at higher and lower pyrrole concentrations, as reported in previous studies [75], [79], [80]. Figure 3.2h shows the conductivity of PPy at different sulfuric acid concentrations. The data indicate that a lower sulfuric acid concentration (0.1 M) leads to higher conductivity, which decreases as the sulfuric acid concentration increases. This decline in conductivity can be attributed to the reduced permeability of hydroxyl groups as a result of the densely packed polymer chains, which limit ion mobility and conductivity within the polymer matrix [50], [81]. This has direct implications for their use in energy storage devices such as lead acid batteries, where low resistivity is crucial for maximizing charge transport and energy efficiency.

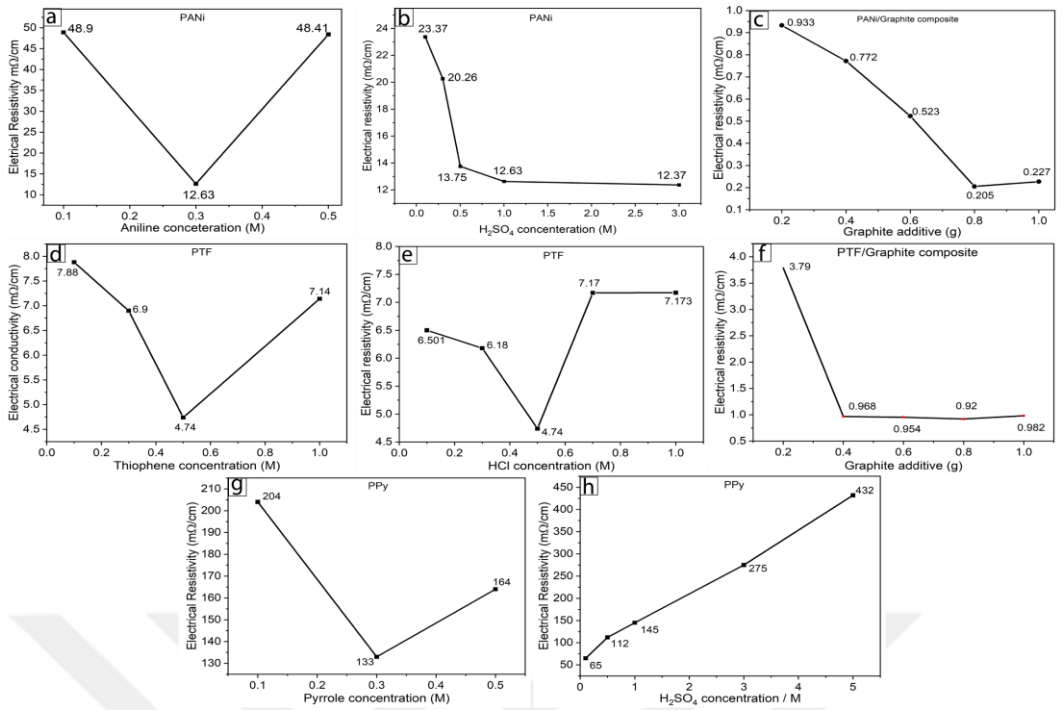


Figure 3.2 Electrical conductivity of CPs and their graphite composites under various conditions: a) varying aniline concentration; b) sulfuric acid concentration; c) PANi/graphite content; d) thiophene concentration; e) HCl concentration; f) PTF/graphite content; g) varying pyrrole concentration; h) sulfuric acid concentration.

3.2.3 Differential Scanning Calorimetry and Thermogravimetric Analysis DSC-TGA

Figure 3.3 shows the thermal behavior of conductive polymers and conductive polymer graphite composite. Figure 3.3a shows the DSC curve exhibits two distinct endothermic peaks. The first peak, observed in the range of 27.8 °C to 125 °C, corresponds to the evaporation of physically adsorbed water molecules from the PANi matrix. This is a common feature in conductive polymers due to the presence of residual moisture within their porous structure. The second endothermic transition, occurring between 228 °C and 373 °C with a maximum at approximately 336.6 °C, is associated with structural rearrangements within the polymer. This peak likely results from a combination of interchain crosslinking, partial recrystallization, and possible isomerization processes, reflecting thermally induced transitions in the PANi backbone. The TGA curve (orange line), which complement the DSC data, shows a corresponding minor weight loss below 125 °C,

confirming the release of moisture. A more significant weight loss is observed between approximately 280 °C and 420 °C, which can be attributed to the thermal decomposition of the doped PANi backbone. This stage is indicative of chain scission, degradation of the polymer structure, and loss of dopant species. Beyond 500 °C, a gradual weight loss continues, representing carbonization of the residual organic components and the breakdown of thermally stable dopants or inorganic residues. These thermal characteristics confirm that PANi synthesized under the given conditions (0.3 M aniline and 3 M H_2SO_4) exhibits good thermal stability up to approximately 280 °C, which is suitable for most electrochemical device applications [64], [82], [83]. Figure 3.3b illustrate the thermal analysis of the PANi/G composite, as shown in the combined TGA–DSC graph, reveals its thermal stability and decomposition behavior. The TGA curve (orange line) indicates an initial minor weight loss below 125 °C, corresponding to the evaporation of moisture and physically adsorbed water from the composite matrix. A significant weight loss occurs between approximately 280 °C and 420 °C, which is attributed to the thermal degradation of the polyaniline backbone and the release of dopant molecules. Beyond 500 °C, a gradual weight loss continues, associated with the carbonization of the organic matrix and decomposition of thermally stable residues. The DSC curve (blue line) complements this analysis by showing two prominent endothermic peaks. The first, below 125 °C, corresponds to the moisture evaporation event, while the second, broader peak between 230 °C and 370 °C, with a minimum near 336 °C, reflects thermal transitions within the PANi chains, such as interchain reorganization, partial crystallization, or dopant-polymer interactions. A broad exothermic feature beyond 700 °C suggests slow oxidative degradation or carbon residue breakdown. These results confirm that the PANi/G composite maintains good thermal stability up to around 280 °C, making it suitable for electrochemical applications that require moderate thermal endurance [63]–[65], [76], [82]. Figure 3.3c shows the DSC-TGA analysis; the DSC curve of PTF shows a small endothermic peak below 150°C, which can be attributed to the evaporation of moisture, residual solvent, or unreacted oxidant. Then, an exothermic transition due to the oxidative decomposition of the conjugated thiophene backbone was recorded approximately between 250°C and 450°C. PTF shows an amorphous, rigidly conjugated polymer without thermoplastic behavior due to the absence of any glass transition Tg or melting peak before its decomposition. In the TG curve,

a minor mass loss (< 5%) occurs below 150°C, as confirmed by the DSC analysis, while a sharp weight decrease of about 70–80% is observed between 250°C and 450°C due to the separation and oxidation of the polymer chain, and the remaining carbonaceous residue is gradually oxidized up to about 950–1000°C. These results confirm that PTF remains stable up to roughly 230–250°C and decomposes through a single dominant exothermic stage typical of conjugated polymers [67], [84]–[88]. Figure 3.3d illustrates the DSC-TGA curve of PTF/G, which shows a typical multi-stage thermal degradation behavior. The material exhibits a minor weight loss below 150 ˚C, which can be attributed to the removal of adsorbed moisture and/or residual impurities. PTF/G remains thermally stable up to approximately 230-250 ˚C. An exothermic peak occurs in DSC between 250 and 450 ˚C suggested that the degradation stage of the composite starts. This corresponds to the oxidative decomposition of PTF backbone. Above 450 ˚C, gradual mass loss is observed due to oxidation of carbonaceous residue and the presence of thermally stable graphite. Compared with neat PTF, the PTF/G composite exhibits higher residual mass and slightly improved thermal stability, confirming the stabilizing effect of graphite within the composite structure [89]. Figure 3.3e illustrate the thermal behavior of polypyrrole (PPy). The initial weight loss observed in the TGA curve between 25 °C and 100 °C corresponds to the evaporation of absorbed moisture. A gradual weight reduction beyond 100 °C is attributed to the release of dopant residues and structural impurities. A significant mass loss between 200 °C and 400 °C marks the onset of polymer degradation. Meanwhile, the DSC curve shows a broad endothermic response, indicating an amorphous nature and low crystallinity of the material. Together, these results confirm the moderate thermal stability and non-crystalline structure of PPy [79], [90].

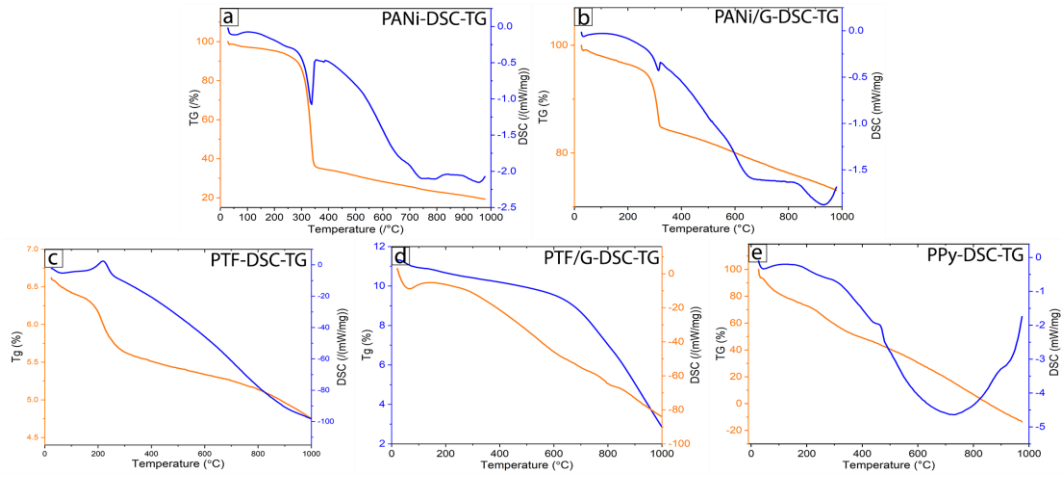


Figure 3.3 DSC-TGA thermal analysis of a) polyaniline powder; b) Polyaniline/Graphite composite powder; c) Polythiophene powder; d) Polythiophene/Graphite composite powder; e) Polypyrrole powder

3.2.4 Brunauer, Emmett & Teller (BET)

The BET analysis presented in Figures 3.4a–h illustrates the influence of varying monomer concentration (aniline, thiophene and pyrrole), acid concentration (H_2SO_4 and HCl), and graphite loading on the surface area and pore diameter of conductive polymers (CPs) and their composites. Starting with PANi, Figure 3.4a shows that increasing the aniline concentration from 0.1 M to 0.5 M leads to a significant rise in surface area (from 14.06 to 45.85 m^2 g^{-1}), with a peak pore diameter observed at 0.3 M (20.18 nm), suggesting that moderate monomer concentrations promote more favorable chain packing and porosity. In Figure 3.4b, varying sulfuric acid concentration has a pronounced effect: the surface area spikes at 0.5 M (74.28 m^2 g^{-1}), then decreases with higher acid concentration, while the pore diameter reaches a maximum at 3 M (39.19 nm). This indicates that while moderate acid levels enhance surface development, stronger acid promotes pore enlargement and interchain connectivity, as seen in the P03_3 sample. Together, these features imply that optimal doping enhances π–π stacking and conductivity through improved morphology.

For PANi/graphite (PANi/G) composites, the BET results shown in Figure 3.4c indicate a clear inverse relationship between graphite content and surface area. As the amount of graphite increases from 0.2 g to 1.0 g, the surface area of the composite decreases significantly—from 17.1 m^2 g^{-1} to 8.76 m^2 g^{-1}. This notable

reduction can be attributed to the fact that graphite particles tend to occupy or block the active pores of the PANi matrix, thereby limiting the overall accessible surface area available for electrochemical interactions. At the same time, the pore diameter exhibits a substantial increase, reaching a peak value of 47.94 nm at 0.8 g of graphite before slightly decreasing to 46.83 nm at 1.0 g. This trend suggests that the incorporation of graphite contributes to the formation of larger pore structures, possibly due to enhanced spacing between polymer chains or the generation of interfacial voids between PANi and graphite. The presence of graphite may also facilitate improved chain alignment or act as a physical spacer, preventing excessive entanglement or collapse of the polymer framework. Despite the reduction in surface area, the increased pore diameter is advantageous for ion transport and electrolyte diffusion, which are critical for improving the charge storage and cycling performance of the composite material.

In the case of pure polythiophene (PTF), Figures 3.4d and 3.4e illustrate the effect of both thiophene monomer and HCl acid concentrations on the surface area and pore structure of the synthesized conductive polymer. The surface area decreases with the increasing of thiophene monomer concentration from 0.1 M to 1.0 M, from 26.85 $m^2 g^{-1}$ to 5.05 $m^2 g^{-1}$. This behavior can be attributed to the denser packing of polymer chains and aggregation at higher monomer concentrations, which limits the number of accessible surface sites. In conclusion, the use of thiophene monomer concentrations from 0.1 M to 1.0 M leads to a steady decline in surface area. In contrast, the pore diameter shows a slight increase, from 14.93 nm to 16.71 nm, giving the indication that there is a possible formation of interchain voids or structural irregularities at high monomer concentrations, which can maintain moderate-ion diffusion channels. Simultaneously, a non-linear fluctuation in surface area and pore diameter was observed, which was caused by using different concentrations of hydrochloric acid (0.1 M to 1.0 M). The concentrations at 0.5 M of HCl acid with 0.5 M monomer loading showed relatively low pore diameter (15.98 nm) with a good value of the surface area (16.9 $m^2 g^{-1}$). These findings support sufficient doping and interchain spacing, while at a higher HCl concentration of 1.0 M, the surface area reduced (11.72 $m^2 g^{-1}$) which can be attributed to a compact polymer structure with slightly enlarged pores.

Regarding the PTF/graphite (PTF/G) composites, as shown in Figure 3.4f, the surface area gradually decreases from 6.92 m^2 g^{-1} at 0.2 g graphite to a minimum of 4.57 m^2 g^{-1} at 0.8 g, followed by a slight increase to 5.5 m^2 g^{-1} at 1.0 g. This trend is consistent with the behavior observed in PANi/G composites and can be attributed to the partial obstruction or coverage of the polymer surface by graphite particles. Graphite's layered structure may also contribute to the reduction in available surface area by acting as a barrier to nitrogen adsorption during BET analysis. In contrast, the pore diameter fluctuates only slightly between 11.27 nm and 10.99 nm across all graphite contents, indicating that the incorporation of graphite has a minimal effect on the pore structure of PTF. This subtle variation implies that the mesoporous framework of the composite is largely maintained, despite the filler addition. The preservation of such pore characteristics is beneficial for electrochemical performance, as it ensures sufficient pathways for ion diffusion and electrolyte penetration. Figures 3.4g and h present the results of the pore diameter and surface area measurements of PPy synthesized under different pyrrole and sulfuric acid concentrations through chemical oxidative polymerization. As shown in these figures, the highest surface area and pore size were obtained when the pyrrole concentration was 0.3 M. At this concentration, the polymerization process was most efficient, leading to the formation of a conducting polymer structure with improved porosity. This enhancement in surface area and pore size can be attributed to the optimal balance between the pyrrole monomer concentration and the reaction conditions. The efficient polymerization resulted in a more porous network, increasing the number of active sites available for electrochemical reactions. The results suggest that the 0.3 M pyrrole concentration enables the formation of a more structured and conductive PPy material, making it suitable for use as additive in fumed silica-based gel electrolyte requiring high surface area. Overall, while the inclusion of graphite generally leads to a decrease in surface area in both PANi and PTF matrices, it either improves or maintains favorable pore structures, which are essential for achieving efficient charge transport and utilization in supercapacitor and battery applications.

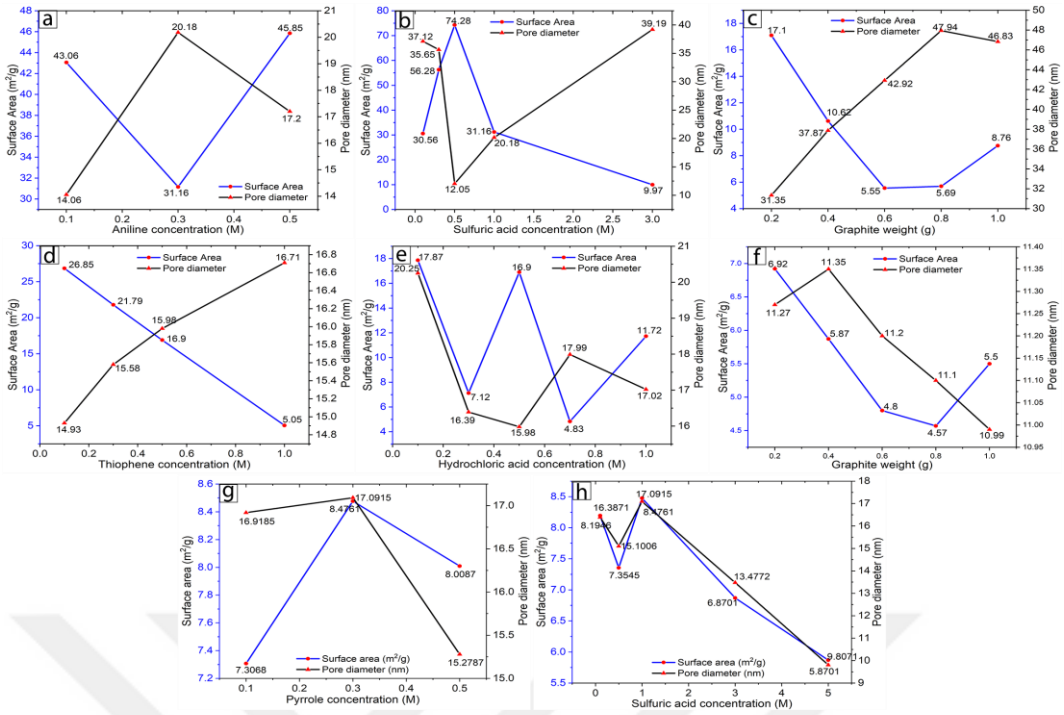


Figure 3.4 BET analysis (Surface area & Pore diameter) of CPs and their graphite composites under various conditions: a) varying aniline concentration; b) sulfuric acid concentration; c) PANi/graphite content; d) thiophene concentration; e) HCl concentration; f) PTF/graphite content; g) varying pyrrole concentration; h) sulfuric acid concentration.

3.2.5 Field Emission Scanning Electron Microscopy (EF-SEM) and Scanning Electron Microscopy (SEM)

Figure 3.5 displays the SEM images of PANi samples prepared with varying concentrations of aniline and sulfuric acid. Images (a), (b), and (c) present the SEM results corresponding to different aniline concentrations. It is evident that the polyaniline samples do not exhibit smooth surfaces, but rather display a heterogeneous and granular morphology, composed of agglomerated flake-like structures. This morphology is typical of PANi and is often described as "cauliflower-like," a common feature of its amorphous nature. With increasing acid concentration, PANi particles tend to adopt a more flake-like and interconnected morphology. The average particle size was observed to gradually decrease with increasing aniline concentration, ranging approximately from 120 to 110 nm. Similarly, as sulfuric acid concentration increased, a slight increase in particle size was observed, ranging from about 109 to 121 nm. These observations suggest that

higher monomer and acid concentrations promote the agglomeration of particles, likely due to more efficient polymerization and enhanced chain organization during the synthesis process. This morphological evolution is believed to improve interconnectivity among PANi particles, which can contribute to more effective charge transport. This morphological evolution is believed to improve interconnectivity among PANi particles and increase the effective surface area accessible to the electrolyte. Images (d), (e), (f), and (g) illustrate the effect of sulfuric acid concentration on the morphology of PANi. A notable increase in agglomeration is seen at higher acid molarities, which is consistent with previously reported trends in the literature [48], [57], [91], [92].

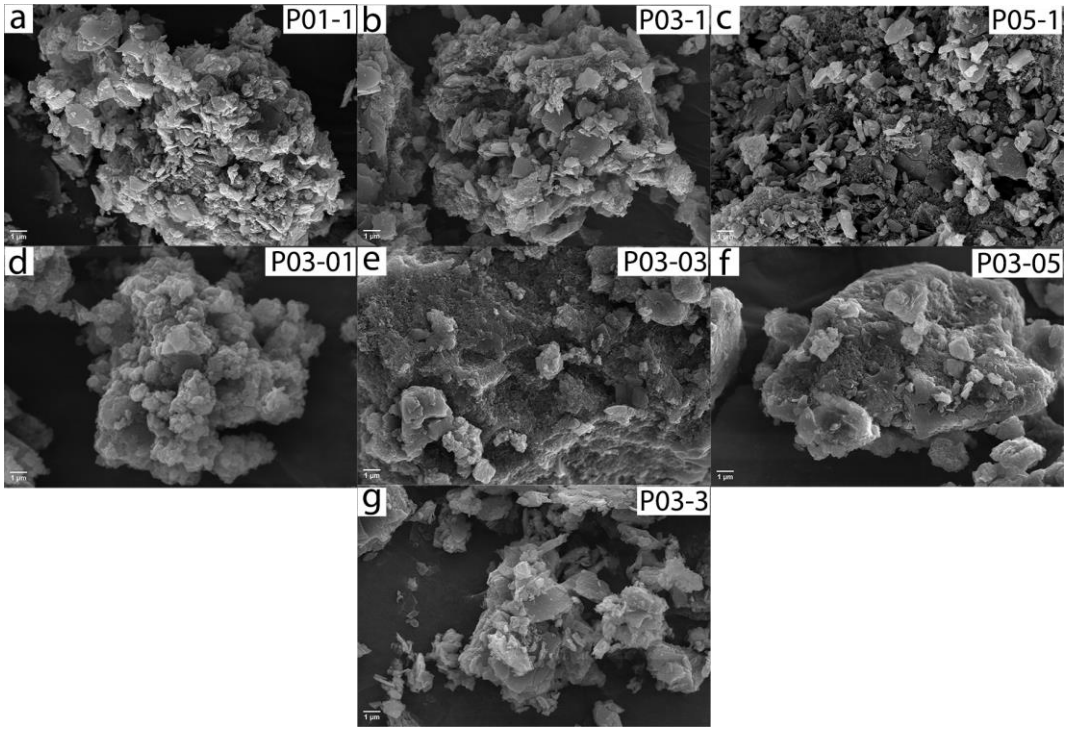


Figure 3.5 Scanning electron microscopy of different polyaniline samples synthesized using varying concentration of monomer and sulfuric acid.

The SEM images of the PANi/G composites with varying graphite content Figure 3.6 show a clear presence of layered graphite sheets decorated with polyaniline. Unlike pure PANi, which typically has a granular or cauliflower-like morphology, the PANi/G composites exhibit a more flake-like and layered structure due to the incorporation of graphite [60], [63], [65]. As the graphite content increases from PANi/G-0.2 to PANi/G-1.0, the images reveal denser packing and stronger agglomeration of thin, crumpled sheets, suggesting that polyaniline has

successfully coated or partially wrapped around the graphite flakes. This results in a more interconnected network, which can improve electrical pathways and enhance contact between conductive domains. Similar to how monomer and acid concentration affect PANi morphology, increasing graphite promotes more compact and ordered composite structures, which is beneficial for applications requiring high conductivity.

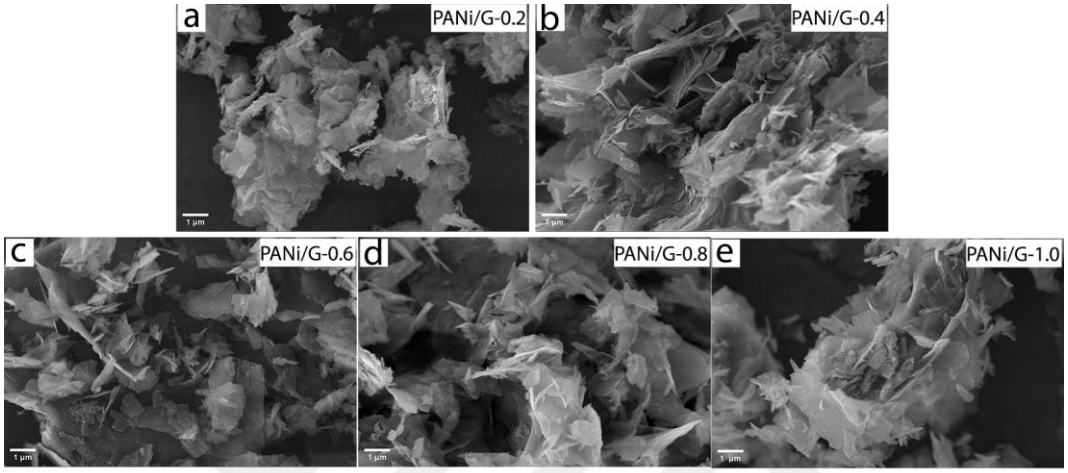


Figure 3.6 Scanning electron microscopy of different polyaniline/graphite composite samples synthesized using varying graphite content.

Figure 3.7 illustrates FESEM images of PTF samples synthesized with different thiophene monomer concentrations. The samples' morphology is generally characterized by a granular and agglomerated structure [66], [77], [78], [84], [93], often referred to as "cauliflower-like," which is typical for polythiophene conductive polymer amorphous form. At 0.1 M and 0.3 M (images a and b), the surface structure appears fragmented with non-uniform particle distribution. However, at a higher concentration of 1.0 M (image d), this increase leads to excessive agglomeration and particle overgrowth, reducing porosity and structural uniformity. Adding 0.5 M (image c) of thiophene monomer makes the surface structure more compact and connected, with better homogeneity. This means that the polymerization process and network formation were improved. The average particle size in the optimized sample (0.5 M) is estimated to be between 115 and 120 nm, based on the scale bar and visual inspection. Images (e, f, g, and h) illustrate the effect of hydrochloric acid concentration on the morphology of PTF at 0.5 M of thiophene content. Increasing the acid concentration enhances particle organization

and compactness. The samples with 0.1 M and 0.3 M of HCl acid concentration have aggregated and irregular particles. At higher acid concentrations of 0.7 M and 1.0 M, the presence of excessive acid induces stronger agglomeration and causes a slight increase in particle size. The average particle size for samples with different acid concentrations ranges from 115 to 125 nm. These findings suggest that moderate acid and monomer concentrations result in a strong and more uniform morphology, which is considered suitable for electrochemical applications, by enhancing the surface area and interconnectivity between PTF particles.

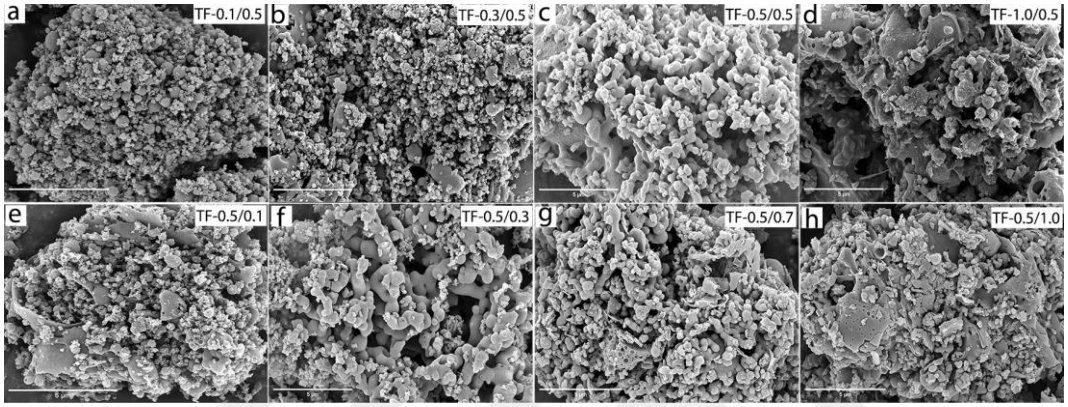


Figure 3.7 Field emission scanning electron microscopy of different polythiophene samples synthesized using varying concentration of monomer and hydrochloric acid.

Figure 3.8 presents FESEM images of PTF/G composites synthesized with varying graphite content, ranging from 0.2 to 1.0 wt%. All samples display a porous and granular surface morphology typical of polythiophene-based materials. At lower graphite content (PTF/G-0.2 and 0.4), the microstructure is dominated by globular PTF particles with limited dispersion of graphite, and the morphology appears loosely packed with irregular porosity [52], [72]. As the graphite content increases to 0.6 and especially 0.8 wt%, the surface becomes more structured and densely packed, with graphite flakes visibly embedded within the polymer matrix. These samples show the most balanced morphology, with well-integrated PTF spheres anchored onto graphite sheets, forming a highly interconnected network. At the highest graphite loading (PTF/G-1.0), excessive graphite results in particle overgrowth and agglomeration, reducing the uniformity and accessible surface area. This suggests that moderate graphite content, particularly at 0.8 wt%, optimizes the

composite's structure by enhancing interfacial contact and conductive pathways, which are favorable for charge transfer in electrochemical applications.

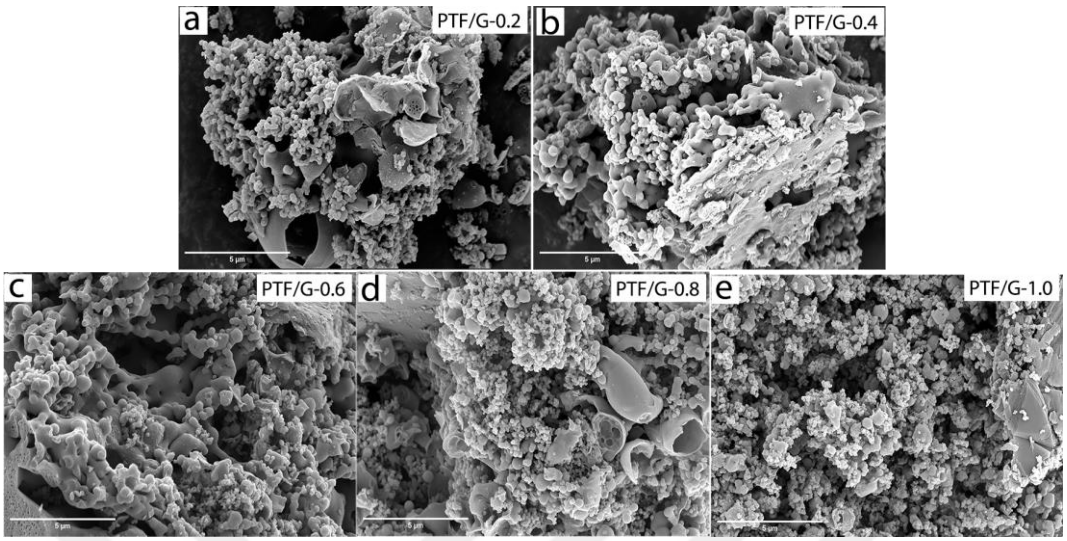


Figure 3.8 Field emission scanning electron microscopy of different polythiophene/graphite composite samples synthesized using different graphite content.

Figure 3.9 shows the scanning electron microscopy (SEM) images of polypyrrole (PPy) samples prepared with different concentrations of pyrrole monomer and sulfuric acid. The SEM images reveal that the synthesized PPy exhibits a cauliflower-like morphology with hemi-granular grains, which is characteristic of conducting polymers synthesized via chemical oxidative polymerization. This morphology is typically indicative of a high degree of polymerization, where the polymer chains form dense clusters, resulting in a rough, granular surface. Interestingly, the concentration of sulfuric acid and pyrrole did not significantly affect the overall morphology of the PPy samples. Regardless of the varying concentrations of these components, the PPy retained the cauliflower-like structure. This suggests that the polymerization process reached a point of saturation, where the structural development of the polymer became independent of further increases in pyrrole or sulfuric acid concentration. These results align with previous studies [75], [80], [94]–[96], which have shown that while the monomer and acid concentrations can influence the degree of polymerization and conductivity, they have a minimal impact on the overall morphological characteristics of the PPy. The uniformity and consistency of the cauliflower-like structure across different concentrations suggest that the polymerization conditions were controlled

effectively, ensuring a homogeneous distribution of the polymer grains. The hemi-granular nature of the particles is also indicative of the amorphous, non-crystalline nature of PPy, which is often desired for applications requiring high surface areas and enhanced electrochemical properties.

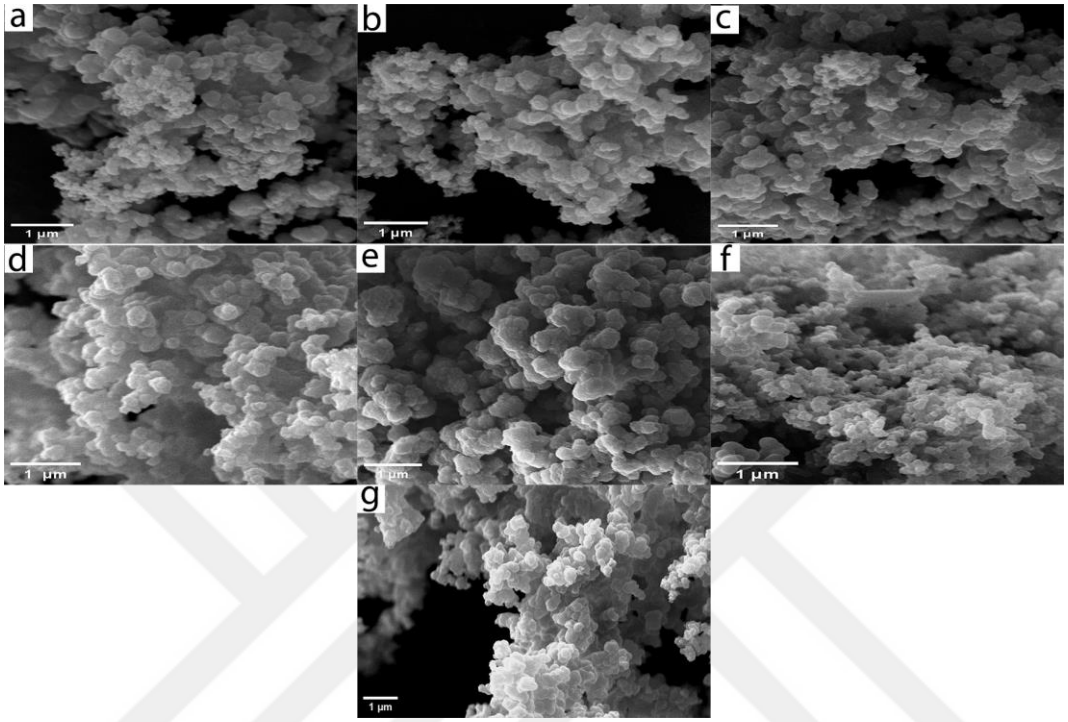


Figure 3.9 SEM images of chemically synthesized PPy with different pyrrole concentrations (a, b, c) and different sulfuric acid concentrations (d, e, f, g).

3.3 Optimization and characterization of Gel Electrolyte Systems

For the optimization of conductive polymers and conductive polymers/graphite composite content into the gel systems that prepared, cyclic voltammogram, electrochemical impedance spectroscopy and Tafel extrapolation were used to monitor the electrochemical behavior of different gel systems each additive was tested separately [29], [53], Table 3.1 shows the conductive polymers and conductive polymers / graphite composite that optimized with the best monomer and acid concentrations.

Table 3.1 The optimal samples of CP's and CP's/G composite that used as gel additives

No.	Sample name	Monomer concentration / M	Acid concentration / M	Graphite content / g
1.	P03-3	Aniline – 0.3	Sulfuric - 3	0
2.	P/G-08	Aniline – 0.3	Sulfuric - 3	0.8
3.	PTF05-05	Thiophene – 0.5	Hydrochloric – 0.5	0
4.	PTF/G-08	Thiophene – 0.5	Hydrochloric – 0.5	0.8
5.	PPy03-01	Pyrrole – 0.3	Sulfuric – 0.1	0

3.3.1 Optimization of Conductive Polymers and Conductive Polymers/Graphite Composites Additives in Fumed Silica Gel Electrolyte

In this part, the optimum sample of CP's and CP's/G composites listed in Table 1. were introduced to the fumed silica-based gel electrolyte. Three major parameters (additives content, stirring time, and stirring rate) were used to optimize the gel system for the battery test. The electrochemical behavior of each gel electrolyte system with different additives were investigated using electrochemical analyses methods, cyclic voltammetry, electrochemical impudence spectroscopy, and Tafel extrapolation.

3.3.2 Optimization of Conductive Polymers and Conductive Polymers/Graphite Composites Additives Content in Fumed Silica Gel Electrolyte

The additive content considered as major parameters that affects the gel consistency and 3D network. In valve-regulated lead-acid batteries, the electrochemical mechanism is controlled by reversible redox reactions of lead electrodes in a sulfuric acid medium (fumed silica-based gel electrolyte), accompanied by the formation of lead sulfate ($PbSO_4$) then reversed into the original form of lead or

lead dioxide in a process called sulfation/desulfation. During the discharge process, metallic lead (Pb) oxidizes to $PbSO_4$ at the negative electrode, while lead dioxide (PbO_2) is simultaneously reduced to ($PbSO_4$) at the positive electrode. As a result of these reactions, the sulfate ions are consumed from the electrolyte. The reverse reaction occurs upon charging, where lead sulfate is electrochemically decomposed back into metallic lead and lead dioxide, restoring sulfate ions in the electrolyte. These sulfation/desulfation processes are directly reflected in cyclic voltammetry by well-defined oxidation and reduction peaks corresponding to the $Pb/PbSO_4$ redox couple. The desulfation process in gel-type batteries is poorly reversible, particularly on the negative electrodes, due to the high charge transfer resistance and less ion diffusion pathways through the gel network, resulting in increasing polarization losses and performance degradation. Therefore, the electrochemical performance of gel-type VRLA batteries is governed by the balance between redox reversibility, sulfate ion diffusion, and charge transfer resistance within the constrained gel network [10], [21], [97]–[99]. Figure 3.10 shows the redox peaks of different gel systems with different additives. Figure 3.10a. illustrates the cyclic voltammograms obtained from bare fumed silica gel electrolyte and fumed silica-based gel electrolytes containing varying amounts of P03-3 additive Specifically, the oxidation peak observed around -0.5 V corresponds to the electrochemical oxidation of metallic lead to lead sulfate ($PbSO_4$), while the reduction peak observed around -0.7 V represents the reduction of lead sulfate back to metallic lead during the reverse scan [27]–[29], [53]. The cyclic voltammetry results indicate that introducing PANi powder into the bare gel electrolyte significantly enhances the redox peaks (anodic and cathodic), indicating electrochemical activity was improved. This behavior is attributed to the presence of PANi with high electrical conductivity and capacitive nature, which enhances both the ionic transport and the charge transfer processes within the gel electrolyte. However, the PANi loading influences the gel matrix and the formation of the 3D silica network. Both excessive and insufficient PANi contents lead to a non-homogeneous gel structure; higher PANi amounts result in pore blockage and/or particle agglomeration and reduce ion electrode interactions, while lower PANi loadings below 0.6 wt% provide limited conductivity enhancement and may disrupt the gel structure. The highest peak current and charge/discharge capacities were obtained at 0.6 wt% of PANi content. This indicates an improvement in electrochemical reversibility and overall gel

performance. The deviation from this optimal loading causes a reduction in the electrochemical performance as a result of aggregation-induced, ion-transport limitations at higher contents or insufficient conductivity at lower PANi loadings [100]–[102]. The CV results indicate that the incorporation of the PANi/G composite significantly enhances electrochemical activity compared to the bare gel electrolyte. Adding a PANi/G composite increases the anodic and cathodic peak currents. This means that PANi/G composite has a similar effect as PANi, has high electrical conductivity, and improves storage capacity, which speeds up ion and charge transport. Similar to PANi, the gel system with 0.6 wt% of PANi/G has the highest anodic and cathodic peak currents, as shown in Figure 10b. This data indicates that the PANi additive and the PANi/G composite additive have a similar effect on the electrochemical performance of the doped fumed silica-based gel electrolyte. At lower PANi/G content (0.2 and 0.4 wt%), the redox peaks show better behavior than the PANi additive at the same loading. This can be attributed to the presence of polyaniline particles coated with graphite particles. PANi/G powder has higher electrical conductivity [76], which leads to the enhancement of electrochemical reversibility of the Pb/PbSO4 reaction during charge/discharge processes [103]. The improvement can be attributed to less agglomeration and better additive dispersion within the gel matrix. At higher PANi/G composite content, the redox peaks show similar electrochemical performance to the PANi additive at the same ratio due to disrupted gel formation and/or powder agglomeration and a lack of homogeneity in the gel structure. Figure 3.10c. presents the results of the polypyrrole (PPy) additive in the fumed silica gel electrolyte. The highest oxidation and reduction peaks correspond to the gel electrolyte containing 0.8 wt% of PPy, indicating the best consistency and stability at this additive ratio. This suggests that, at 0.8 wt%, PPy forms a highly conductive, stable network that facilitates efficient ion movement during the electrochemical processes. On the other hand, for the 1 wt% sample, the oxidation and reduction peaks decreased significantly, approaching those of the fumed silica-based gel electrolyte without any PPy addition. This decrease can be attributed to the reduced homogeneity of the gel as the PPy concentration increased. At higher concentrations, the excess PPy particles may disrupt the uniformity of the gel, leading to the formation of aggregates or clusters, which can impede the smooth flow of ions and degrade electrochemical performance. A slight shifting was noticed in the CV curve for

different PPy additive content; this can be attributed to inhomogeneous dispersion of PPy within the gel matrix. Such accumulation may result in a localized variation in conductivity and electrochemical activity, which may cause inconsistency in redox peak position. On the other hand, the addition of PPy may cause some changes in electrode surface properties over successive cycles, such as surface oxidation, roughening, or partial passivation, which may alter the electron transfer kinetics leading to peak shift. The other PPy loading also enhances the electrochemical performance of gel systems, indicating that the PPy particles have better homogeneity when introduced into the fumed silica-based gel electrolyte and do not disrupt the gel structure, also afford better charge transfer, and increase the ionic conductivity [94], [104]–[107]. Figure 3.10d. shows the results of polythiophene conductive polymer as an additive material. The overall redox activity was improved with various PTF loadings; the gel system containing 0.2 wt% of PTF has the highest and sharpest current peaks, indicating that the use of a small addition of PTF improves the gel structure, facilitates the ionic transport, and increases the redox reversibility of the sulfation/desulfation reaction. As noticed in the figure, the increases in PTF loading decrease the peak current, indicating that the presence of a higher amount of PTF powder within the gel matrix disrupts gel structure and suppresses a well-connected three-dimensional network, resulting in less ionic transport and increasing the charge transfer resistance. Despite the decrease in electrochemical performance with the increasing of PTF content in the gel structure, the current peaks and electrochemical performance are way better than in the fumed silica-based gel system [108]–[112]. Figure 3.10e presents the results of a CV analysis of gel systems containing various amounts of a polythiophene/graphite composite. The addition of PTF/G composite shows improvement in current peaks in comparison with the gel without additive material; the additive materials enhance the gel formation without disrupting the three-dimensional matrix. Additive particles improve the ionic transfer and charge transfer resistance through increasing the ion diffusion pathways and enhancing the gel homogeneity [67, 68]. The gel system containing 0.2 wt% of PTF/G composite shows the highest peak current, indicating a better homogeneity of the gel structure. The peak currents decrease slightly with the increase of PTF/G composite loadings but lie within the same range of results. The decrease in peak currents results from the agglomeration of additive materials, which decreases the ion diffusion

pathways, or from the disruption of 3D network formation in the case of high content. Figure 3.10f. illustrates the peak current responses corresponding to the optimum additive content for each material. Among all gel systems investigated, the incorporation of PPy exhibit the highest electrochemical performance compared with the bare fumed silica-based gel electrolyte. The enhancement in peak current observed of PTF came after PPy, suggesting that PPy embedded in a fumed silica gel matrix achieves a more uniform dispersion with reduced agglomeration, leading to a well-connected three-dimensional network formation. In contrast, PANi, PANi/G, and PTF/G composites exhibit comparable electrochemical behavior, with peak current values approximately 0.01 A. This similarity indicates that these additives may partially disrupt the gel network structure, resulting in fewer effective ion diffusion pathways and reduced ionic transport. Overall, the addition of conductive polymer and conductive polymer composites materials improves the electrochemical performance of the gel electrolyte relative to the bare fumed silica-based gel system, due to increasing ionic transport, more gel uniformity, and structural homogeneity of the gel.

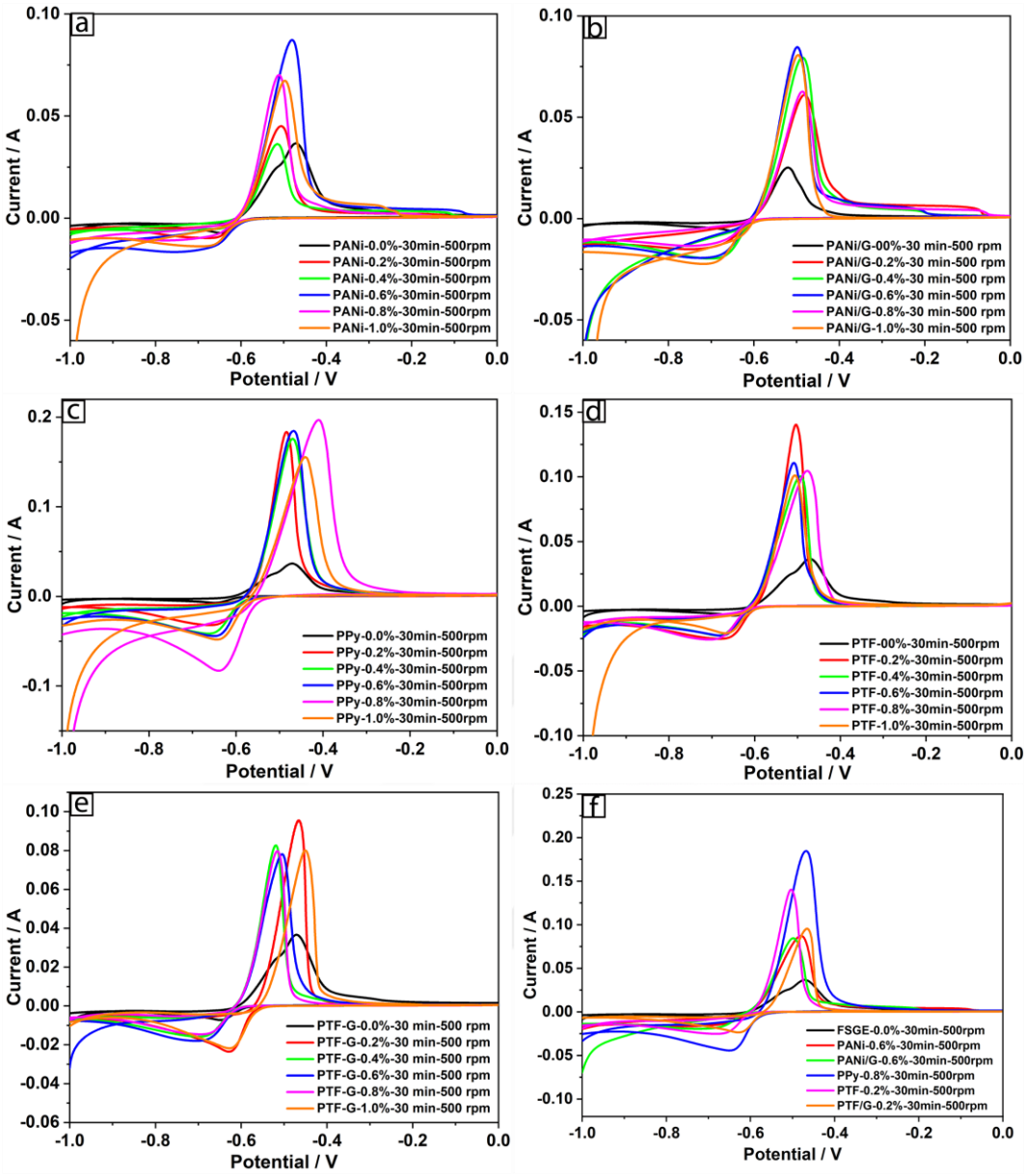


Figure 3.10 Cyclic voltammetry analysis of fumed silica-based gel electrolytes containing different additive contents at stirring time 30 min and stirring rate 500 rpm (a) PANi, (b) PANi/G composite, (c) PPy, (d) PTF, and (e) PTF/G composite.

Electrochemical impedance spectroscopy (EIS) is an important parameter that gives a great analysis of charge transfer reactions, ionic transport, and interfacial phenomena in fumed silica gel electrolyte used in VRLA batteries. In gel-type batteries, the fumed silica immobilizes the sulfuric acid and forms a porous three-dimensional gel network and preserves continuous pathways that allow for sulfate-ion migration toward the electrode surfaces. In EIS, the high frequency intercepted in the impedance spectrum corresponds to the bulk resistance of the gel electrolyte,

which is governed by the well-connected silica network and acid concentration. The charge transfer resistance at the electrode/electrolyte gel interface is reflected by the mid-frequency semicircle and is strongly influenced by the reversible formation and dissolution of lead sulfate ($PbSO_4$) during charge/discharge. According to the electrochemistry of VRLA, the reversible formation of $PbSO_4$ low interfacial resistance and active surface accessibility, whereas the irreversible growth of coarse $PbSO_4$ crystals partially blocks pores and active sites, resulting in increasing charge transfer and diffusion resistance. At low frequencies, the impedance response is dominated by diffusion-controlled processes that are represented by the sulfate-ion transport within the gel matrix and porous active materials. In the case of irreversible sulfation, the sulfate ion is increasingly hindered due to the pore blockage and lack of active sites. Accordingly, the EIS response of fumed silica-based gel electrolyte shows the combined effects of gel structure, interfacial sulfate chemistry, and ion diffusion dynamics within the gel type VRLA system. Figure 3.11 illustrates the EIS results of gel systems with different additive materials with various additive content. PANi results in figure 3.11a confirms the positive impact of PANi on the electrochemical performance of the fumed silica-based gel electrolytes. The lowest charge transfer resistance (R_{ct}) was achieved when the PANi additive amount was 0.6 wt%. Indicating that the highest ionic transport in the gel electrolyte system, which confirms CV analysis results. The decrease in R_{ct} suggests that the introducing of PANi to the gel facilitates faster charge transfer kinetics at the electrode/electrolyte interface, particularly during the oxidation of metallic lead to lead-sulfate. The improved charge transfer can be attributed to the intrinsic conductivity of PANi and its ability to form a percolation network within the silica gel matrix, which supports ion and electron mobility. The development of a well-connected three-dimensional porous gel structure, which plays a key role in enhancing electrochemical performance, was also supported by the Warburg impedance values (W) listed in Table 3.2 A lower Warburg impedance reflects improved ion diffusion within the electrolyte, indicating that the PANi additive contributes to forming a more interconnected and ion-permeable gel network. This structure enables more efficient mass transport processes, especially in redox reactions involving lead and lead sulfate.

Table 3.2 R_s, R_{ct}, I_{corr}, and corrosion rate values of fumed silica-based gel electrolytes containing different amounts of PANi (wt%)

PANi (wt%)	R_s (Ω)	R_{ct} (Ω)	W	E_{corr} (V)	I_{corr} (mA)	Corrosion Rate (mpy)
0	**1.373**	**364.9**	**0.001365**	**-0.600**	**0.0470**	**214.5**
0.2	**1.320**	**348.0**	**0.001161**	**-0.601**	**0.0427**	**195.1**
0.4	**1.280**	**408.8**	**0.000739**	**-0.595**	**0.0326**	**149.0**
0.6	**1.101**	**165.3**	**0.001096**	**-0.585**	**0.0222**	**101.3**
0.8	**0.940**	**384.5**	**0.000982**	**-0.589**	**0.0327**	**149.3**
1.0	**1.451**	**320.8**	**0.001746**	**-0.582**	**0.0271**	**123.8**

Figure 3.11b presents the EIS results of gel systems containing different PANi/graphite composite contents. The best EIS value was achieved with 0.6 wt% of PANi/G, which is consistent with the CV results and indicates that this amount enhances gel network homogeneity and the formation of a well-connected network, resulting in lower charge transfer resistance. The Warburg parameter exhibits noticeable variation with PANi/G content, with a high Warburg (W) value recorded at 0.6 wt%, leading to the conclusion that graphite and PANi particles enhance ion mobility at the electrode/electrolyte interface and the ionic conductivity of the gel system, as well as enhance network pores and sulfate ion transport within the gel matrix. Table 3.3 presents the EIS and Warburg results of gel systems with different PANi/G loadings.

Table 3.3 R_s, R_{ct}, I_{corr}, and corrosion rate values of the gel electrolyte prepared at different PANi/G composite content

PANi/G (wt%)	R_s (Ω)	R_{ct} (Ω)	W	E_{corr} (V)	I_{corr} (mA)	Corrosion Rate (mpy)
0	**1.373**	**364.9**	**0.001365**	**-0.600**	**0.0470**	**214.5**
0.2	**2.199**	**376.3**	**0.00133**	**-0.556**	**0.028**	**13.23**
0.4	**1.254**	**286.1**	**0.001881**	**-0.569**	**0.028**	**12.93**
0.6	**2.272**	**238.10**	**0.003141**	**-0.513**	**0.005**	**2.71**
0.8	**1.751**	**283.6**	**0.001555**	**-0.551**	**0.018**	**8.602**
1.0	**7.916**	**370.9**	**0.002096**	**-0.567**	**0.017**	**7.884**

The increased concentration of PPy in the gel electrolyte led to a noticeable increase in solution resistance and charge transfer resistance as shown in figure 3.11c This indicates that the excessive amount of PPy interferes with the formation of the 3D network structure of fumed silica in the electrolyte, potentially obstructing the internal channels and hindering ion diffusion. As a result, the overall conductivity of the electrolyte decreases, leading to poorer electrochemical performance. As shown in Table 3.4, the gel with 0.8 wt% of PPy displayed the lowest charge transfer resistance (R_{ct}) with the highest Warburg parameter, suggesting that this concentration is optimal for reducing the resistance to charge transfer and give optimal formation of a well-connected three-dimensional network with best ion diffusion pathway. The presence of PPy at this level enhances the solution conductivity and reduces the charge transfer resistance. This reduction is achieved by increasing the interstitial surface area between the electrode and the electrolyte, which in turn provides more available sites for ion exchange and improves the overall ion transport efficiency of the hydronium and sulfate. These findings support the cyclic voltammetry results and the electrochemical performance.

Table 3.4 The R_s, R_{ct}, E_{corr}, and I_{corr} values of the electrolyte consisting of different amounts of PPy in fumed silica-based gel electrolyte

PPy wt%	R_s (Ω)	R_{ct} (Ω)	W	E_{corr} (V)	I_{corr} (mA)	Corrosion Rate (mpy)
0	**1.373**	**364.9**	**0.001365**	**-0.600**	**0.0470**	**214.5**
0.2	**0.6003**	**328.1**	**0.0019**	**-0.575**	**0.159**	**72.58**
0.4	**0.5861**	**229.6**	**0.0033**	**-0.563**	**0.153**	**69.86**
0.6	**0.9006**	**225.4**	**0.0022**	**-575.0**	**0.0934**	**42.68**
0.8	**0.7017**	**205.8**	**0.0041**	**-0.578**	**0.082**	**37.46**
1.0	**0.9271**	**334.9**	**0.0017**	**-0.573**	**0.120**	**54.90**

Figure 3.11d shows the Nyquist plots; a noticeable improvement was observed when using 0.2 wt% of PTF as an additive material to the fumed silica gel electrolyte, as listed in Table 3.5 The R_{ct} of the gel decreased at 0.2 wt% of PTF content, then returned to increase with increasing PTF loading into the gel electrolyte. These findings support the results of CV analysis, which confirm that the 0.2% wt improves the electrochemical behavior of the gel electrolyte; the EIS analysis showed that the incorporation of PTF powder into the fumed silica gel electrolyte enhances the charge transfer through the electrode/electrolyte interface and facilitates the ion mobility and ion diffusion pathways during the oxidation of the metallic Pb electrode to $PbSO_4$. The enhancement of a well-formed 3D porous network of gel structure, which is considered the major reason for enhancing electrochemical performance, and the results of Warburg parameter values (W) listed in Table 3.5.

Table 3.5 The R_s, R_{ct}, E_{corr}, and I_{corr} values of the electrolyte consisting of different PTF content in fumed silica-based gel electrolyte

PTF content wt%	R_s (Ω)	R_{ct} (Ω)	W	E_{corr} (V)	I_{corr} (mA)	Corrosion Rate (mpy)
0	**1.373**	**364.9**	**0.001365**	**-0.600**	**0.0470**	**214.5**
0.2	**0.4849**	**271.4**	**0.004011**	**-0.606**	**0.0302**	**13.81**
0.4	**0.5968**	**386.7**	**0.002006**	**-0.602**	**0.0413**	**18.85**
0.6	**0.5901**	**290.9**	**0.002454**	**-0.597**	**0.0368**	**16.80**
0.8	**0.6488**	**379**	**0.001937**	**-0.576**	**0.046**	**21.04**
1.0	**0.8578**	**640.9**	**0.001402**	**-0.597**	**0.0352**	**16.08**

Figure 3.11e shows the Nyquist spectra for gels containing different amounts of the PTF/G composite and reveals a clear optimum at low loading. Solution resistance of the gel (Rs) varies only slightly with composition but trends upward as the composite fraction grows, indicating that the increase in PTF/G loading enhances the gel conductivity by reducing the bulk resistance. For the charge transfer resistance, the gel system with 0.2 wt% has the lowest Rct referring to better ionic transfer and more homogeneity for the gel matrix as noticed in CV results, while the R_{ct} values increase with the increase in PTF/G content, suggesting that the gel matrix is disrupted, ionic transfer is reduced, and sulfate-ion diffusion is hindered due to less interconnected ion diffusion pathways. These claims can be confirmed according to Warburg parameter data that shows the gel system with 0.2 wt% has a high W value, which corresponds to adequate sulfate ion diffusion at both the electrode/electrolyte interface and through the gel matrix. On the other hand, the increase in PTF/G loadings resulting in higher R_{ct} values indicates that these additions disrupt the gel matrix due to agglomeration and hinder the sulfate ion transport. Solution, charge transfer resistance, and Warburg values are listed in Table 3.6.

Table 3.6 The R_s, R_{ct}, E_{corr}, and I_{corr} values of the electrolyte consisting of different PTF/G composite content in fumed silica-based gel electrolyte

PTF/G content wt%	R_s (Ω)	R_{ct} (Ω)	W	E_{corr} (V)	I_{corr} (mA)	Corrosion Rate (mpy)
0	**1.373**	**364.9**	**0.001365**	**-0.600**	**0.0470**	**214.5**
0.2	**0.7501**	**298.1**	**0.000966**	**-525.0**	**23.10**	**10.57**
0.4	**0.9706**	**534.8**	**0.0006269**	**-534.0**	**43.60**	**19.94**
0.6	**1.129**	**459.7**	**0.000777**	**-505.0**	**28.30**	**12.359**
0.8	**1.073**	**566.6**	**0.0005996**	**-526.0**	**28.40**	**12.99**
1.0	**0.9061**	**430.2**	**0.001097**	**-552.0**	**24.10**	**11.03**

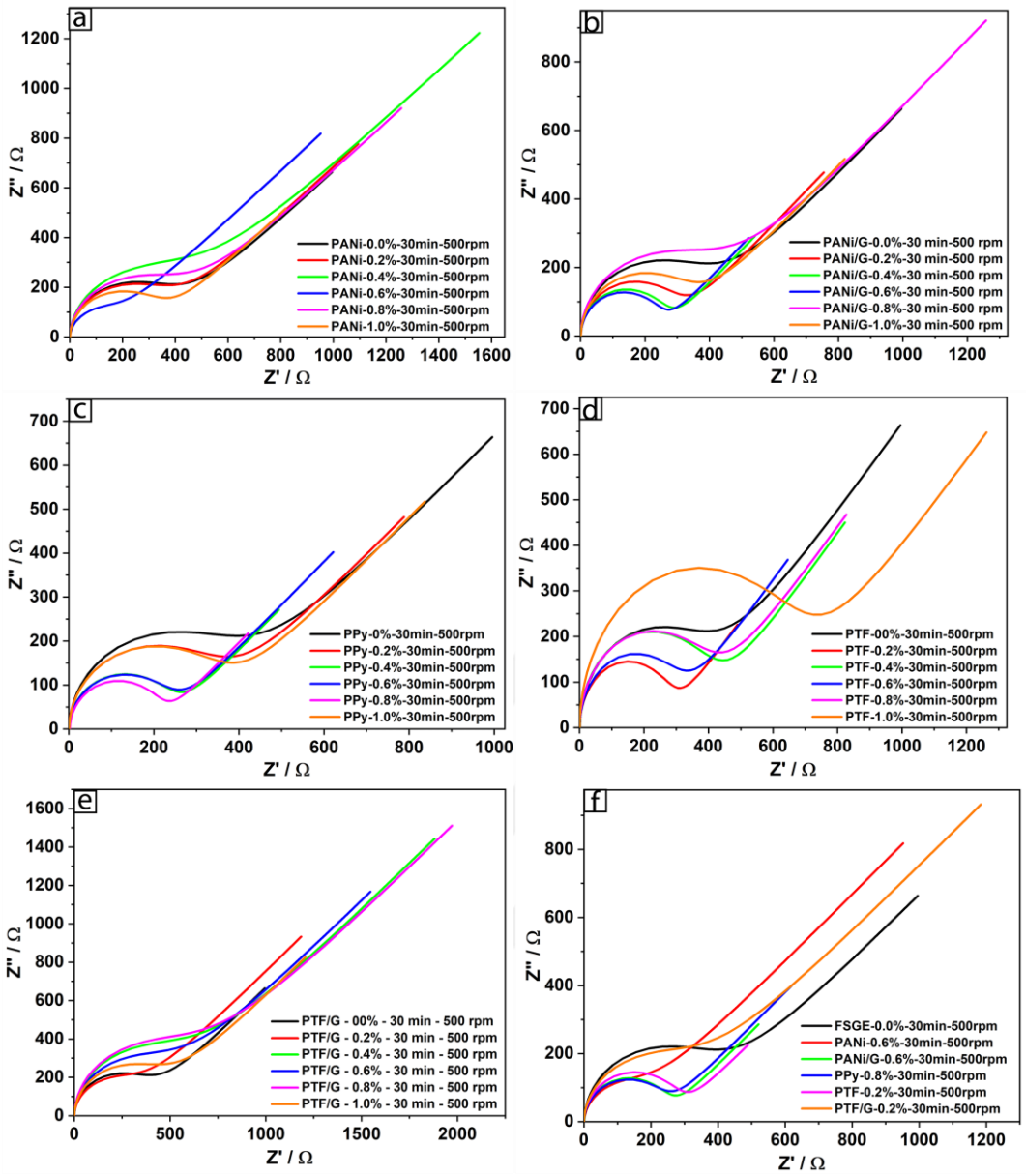


Figure 3.11 Electrochemical impedance spectroscopy EIS of fumed silica-based gel electrolytes containing different additive contents at stirring time 30 min and stirring rate 500 rpm (a) PANi, (b) PANi/G composite, (c) PPy, (d) PTF, and (e) PTF/G composite.

In gel-type VRLA batteries, the formation of lead sulfate ($PbSO_4$) on the electrode surface during discharge mainly refers to the reduction peaks observed in cyclic voltammetry. On the other hand, the formed $PbSO_4$ is reduced back to active lead; this process happens in parallel with corrosion and passivation reactions at the electrode/electrolyte interface. Tafel extrapolation describes the balance between corrosion processes and reduction kinetics. Therefore, $PbSO_4$ reversibility, corrosion behavior, and interfacial charge transfer can be explained through the

changes in peak reduction. Figure 3.12 summarizes the Tafel polarization analysis of various contents of different additive materials. Figure 3.12a presents the corrosion analysis of gel systems containing various PANi amounts. The corrosion behavior of gel systems with different PANi loadings was inspected using Tafel analysis, which confirms the major role of PANi as a protective additive in gel systems. Gel electrolyte containing 0.6 wt% exhibits the lowest corrosion current value, I_{corr}, among other amounts, as well as the minimum corrosion rate recorded. The corrosion potential E_{corr} shifted positively, indicating that the lead electrodes had enhanced electrochemical stability and effective surface passivation in gel electrolyte [102], [113]. The results at lower or higher PANi loadings showed that the corrosion resistance was in decline, suggesting that the excessive amount of PANi disrupts the gel structure of the passivation layer, while insufficient additive suppresses electrode protection. I_{corr}, and E_{corr} values for gel systems containing various PANi contents listed in Table 3.2 The Tafel analysis for gel electrolytes containing various PANi/G composite powders is shown in figure 3.12b, which illustrates that the E_{corr} (corrosion potential) has small changes in shifting towards more positive values; these changes indicate that the electrochemical stability of lead electrodes was improved. As well as the corrosion current I_{corr} decreasing with the increasing in PANi/G additive amount, the gel electrolyte containing 0.6 wt% has the minimum I_{corr} value, suggesting that the gel matrix at this additive ratio has better dispersion and also better gel consistency. These findings were supported with the lowest corrosion rate value at this composition. As shown in table 3.3 The I_{corr}, E_{corr}, and corrosion rates, and the insufficient or excessive PANi/G contents disrupt the gel structure by particle agglomerations and the graphite particles, resulting in galvanic corrosion and localized corrosion [114], or incomplete formation of the three-dimensional gel network. Figure 3.12c presents the Tafel polarization of gel electrolytes with various PPy content; the I_{corr}, E_{corr}, and corrosion rates are listed in table 3.4 The increase in PPy loading decreases both corrosion current density and corrosion rate, suggesting that the gel structure homogeneity is consistent with PPy contents, resulting in the formation of a passivation protecting layer on the Pb electrode surface. At the optimum value of 0.8 wt% of PPy, the lowest I_{corr} and corrosion rate were observed, confirming that this composition has the best gel structure, which improves corrosion resistance within. At a higher PPy content of 1 wt%, the I_{corr} and corrosion rate increase again

due to the additive agglomeration with the gel matrix causing disruption and less-uniform coverage of the electrode surface, leading to less effective protection [115]–[117]. Figure 3.12d illustrates the corrosion analysis of PTF-doped gel electrolyte; the addition of PTF conductive polymer to fumed silica-based gel electrolyte enhances the electrochemical activity as well as the corrosion resistance by reducing corrosion current densities (I_{corr}), subsequently reducing the lead electrode corrosion rate. PTF-doped gel electrolyte with 0.2 wt% exhibits the lowest I_{corr} and corrosion rate, suggesting that this PTF loading disperses uniformly within the gel matrix, leading to the best gel homogeneity as well as good protection behavior against corrosion. The increase in PTF addition slightly increases the corrosion current densities. These changes result from the gel matrix disruption due to powder agglomeration and lack of electrode coverage. PTF-doped gel electrolytes' corrosion current densities, corrosion potentials, and corrosion rates are listed in Table 3.5 The Tafel polarization results for gel electrolytes containing various PTF/G composite content are presented in figure 3.12e. The results show that PTF/G additives have a positive effect on the corrosion current density I_{corr}, which was decreased, leading to decreases in the corrosion rates. The additive material works as a passivating protective layer that covers the Pb electrode and reduces the acidic galvanic effect during electrochemical activity. The gel system containing 0.2 wt% of PTF/G has the optimum corrosion current density Icorr and the lowest corrosion rate, indicating that this additive ratio gives a well-dispersed powder with the gel matrix and enhances gel homogeneity, which is leading to a better Pb electrode coverage than other PTF/G loadings. PTF/G composite-doped gel electrolytes' corrosion current densities, corrosion potentials, and corrosion rates are listed in Table 3.6.

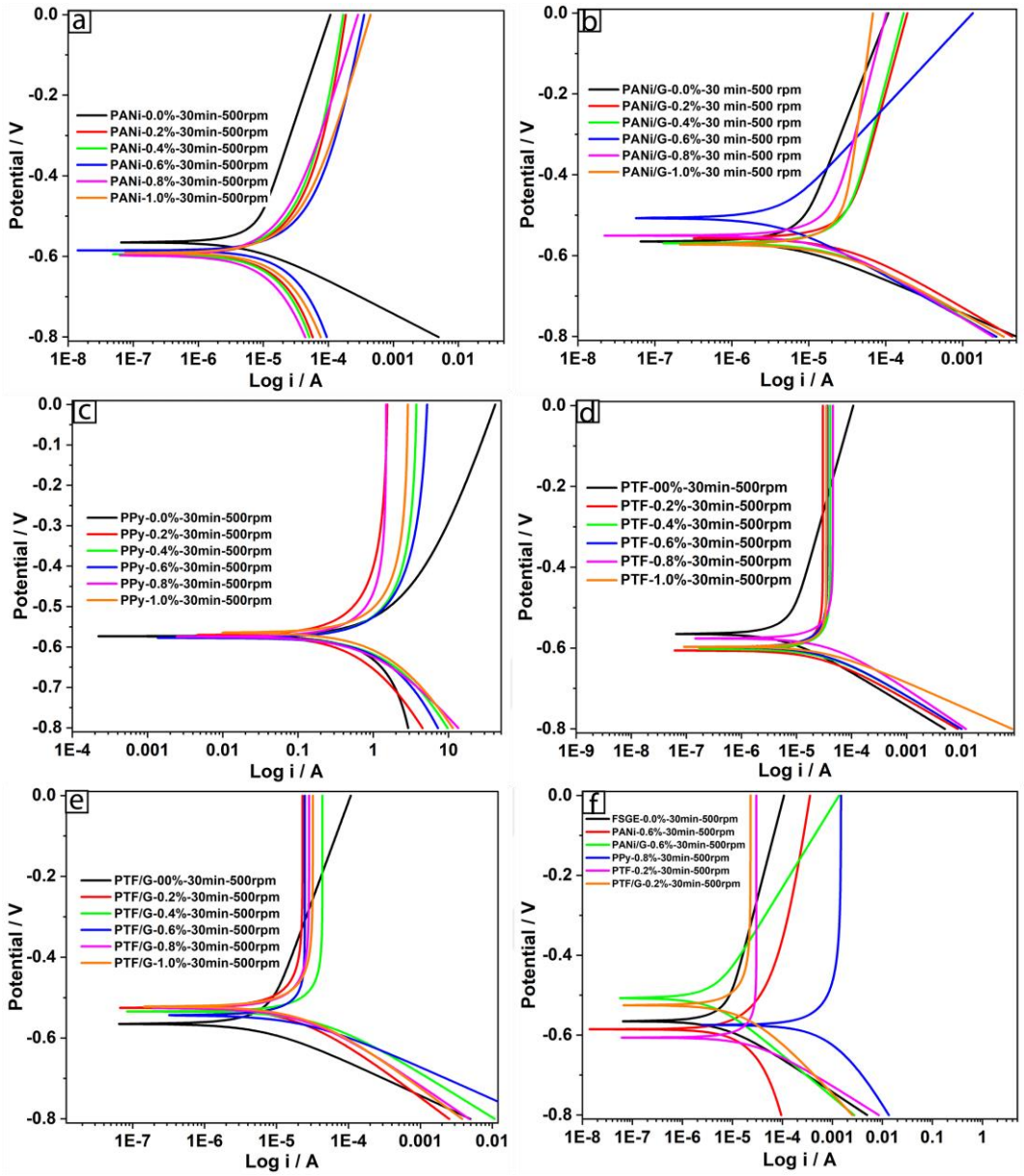


Figure 3.12 TAFEL polarization analysis of fumed silica-based gel electrolytes containing different additive contents at stirring time 30 min and stirring rate 500 rpm (a) PANi, (b) PANi/G composite, (c) PPy, (d) PTF, and (e) PTF/G composite.

3.3.3 Optimization of Stirring Time for the Preparation of Conductive Polymers and Conductive Polymers/Graphite Composites - Containing Fumed Silica-Based Gel Electrolytes

Stirring time plays a crucial role in the formation of the three-dimensional (3D) network and in determining the overall performance of fumed silica-based gel electrolytes [53], [118], [119]. Stirring time was systematically optimized to enhance the dispersion of additive particles within the fumed silica-based gel matrix and to ensure a homogenous gel structure. Various stirring durations (15-150 min) were evaluated to understand the influence of the additives over time. As shown in Figure 3.13, cyclic voltammetry (CV) for different gel systems for each additive material. Figure 3.13a shows the results of the PANi-modified gel electrolyte; short and long stirring times show the lowest current peaks, indicating that the formation of the three-dimensional network is disrupted with lack and excessive time, leading to less homogeneity of gel as well as lower ionic transport and decreased ion diffusion pathways. The moderate stirring time has a positive effect on the redox activity of the gel system, suggesting that the formation of a gel network at these stirring times enhances PANi particle dispersion within the gel matrix, leading to improvement in the overall gel structure; the optimum stirring time was observed at 90 min, suggesting that the gel system exhibits a uniform gel structure with well-dispersed PANi particles within the gel structure, resulting in better ionic transport, ion diffusion pathways, and enhanced reversibility, among other systems. In contrast, the PANi/G composite-doped gel electrolyte shows different electrochemical behavior as presented in Figure 3.13b; the short and moderate stirring times improve the redox activity of the gel systems compared to these systems prepared with the same conditions containing PANi particles. This can be attributed to the presence of PANi-coated graphite particles, which both have a major effect on the enhancement of ionic conductivity and transport within the gel structure. On the other hand, the gel needs a longer stirring time; the optimum stirring time at 150 min enhances the electrochemical activity of the gel system with better gel structure due to higher ionic transport, gel homogeneity, and ion diffusion pathways. The increase of stirring time up to 180 min disrupts the gel formation and reduces electrochemical activity due to particle agglomeration within the gel matrix and leads to non-uniform gel structure. For gel systems containing PPy as

shown in Figure 3.13c. The peak current is significantly enhanced compared to those in PANi and PANi/G gel systems; all peak currents show higher values for gel systems containing PPy additive material, as observed in figures 3.13a, 3.13b, and 3.13c. The best electrochemical performance was observed at a stirring time of 60 min, which has the highest electrochemical performance, concluding that this stirring time provides better PPy dispersion within the gel matrix, leading to enhanced ionic transport and gel homogeneity. At shorter and longer stirring times the gels exhibit lower electrochemical activity than at the optimum time, suggesting that the short and excessive times disrupt the gel structure and decrease the electrochemical activity due to non-uniform three-dimensional network formation as well as decrease the ionic conductivity and lower the electrochemical performance. The addition of PTF and PTF/G exhibit similar trends as presented in Figures 3.13d and 3.13e; in both gel systems, the optimum stirring time was observed at 30 min, suggesting a good dispersion of the additive materials leading to better 3D network formation and ionic transport. On the other hand, increasing stirring time decreases electrochemical performance due to gel structure disruption as well as lower ionic transport as a result of non-uniform three-dimensional network formation in the gel. Overall, these results demonstrate that each additive system requires a specific optimum stirring time to achieve a uniform dispersion, effective gel network formation, and enhanced ionic transport, as shown in Figure 3.13f, which illustrates the gel systems with the optimum stirring time.

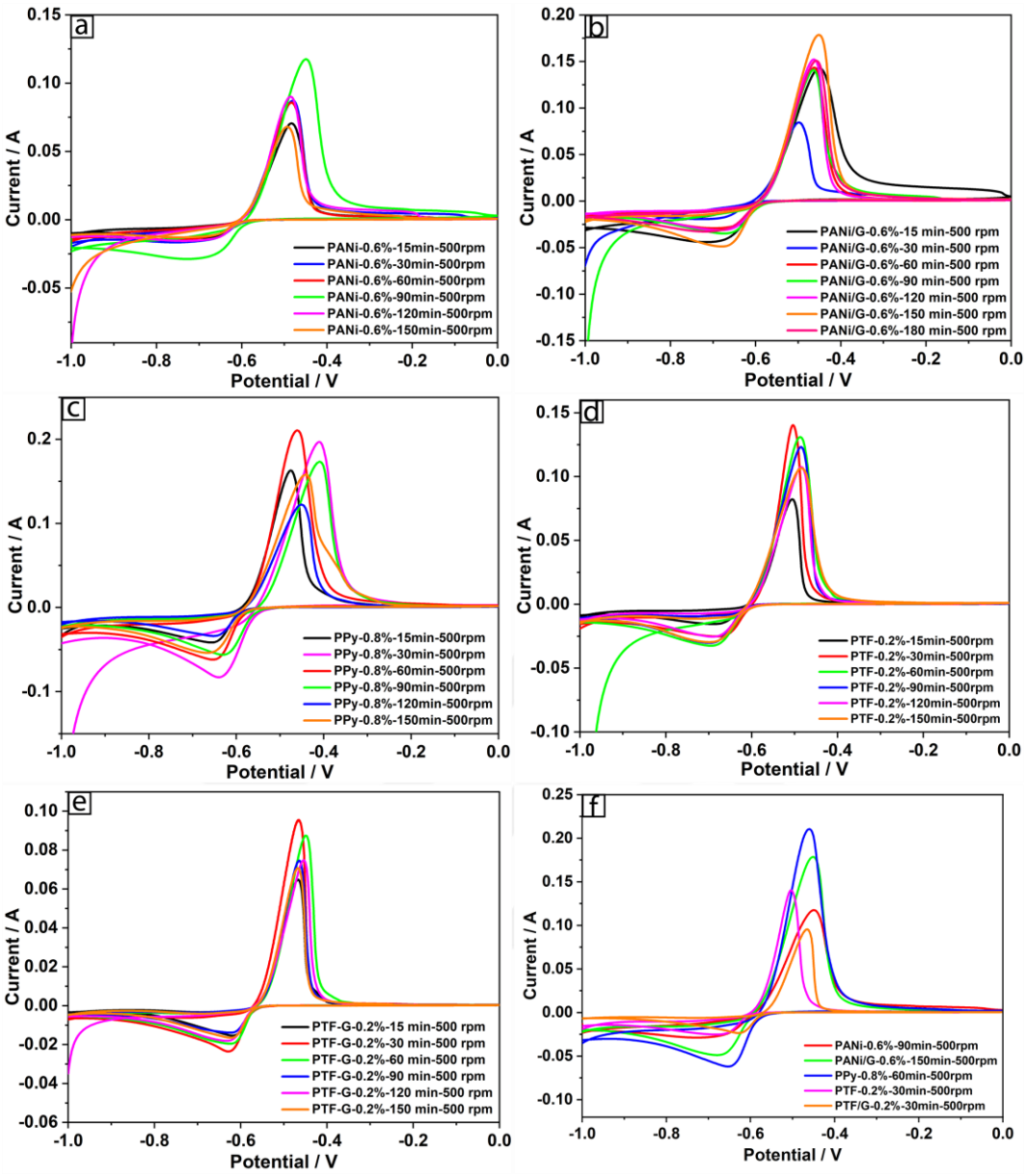


Figure 3.13 Cyclic voltammetry analysis for gel systems prepared at 500 rpm with different stirring time containing (a) 0.6 wt% of PANi, (b) 0.6 wt% of PANi/G composite, (c) 0.8 wt% of PPy, (d) 0.2 wt% of PTF, and (e) 0.2 wt% of PTF /G composite.

Electrochemical impedance spectroscopy (EIS) results in Figure 3.14a supporting cyclic voltammetry findings. The gel system containing 0.6 wt% PANi stirred for 90 minutes exhibits the lowest solution resistance (R_s), indicating high ionic conductivity. Although a slight increase in its charge transfer resistance (R_{ct}) was recorded compared to the sample stirred for 30 minutes, the enhancement in the electrochemical performance of the gel system stirred for 90 min was confirmed by CV data as evidenced by its higher redox peak currents and capacities. At higher

stirring times (15–150 min), gel systems showed less favorable results, with increased R_s and R_{ct} values. At short stirring times the gel system exhibits poor homogeneity as a result of insufficient mixing, resulting in incomplete gelation and uneven PANi particle dispersion. On the other hand, the excessive stirring period may lead to the break of weak physical bonds in the 3D gel network or cause re-agglomeration of either PANi or fumed silica particles within the gel matrix, leading to an inhomogeneous microstructure and hindered ionic mobility. The solution resistance, charge transfer resistance, and Warburg values listed in Table 3.7.

Table 3.7 R_s, R_{ct}, I_{corr}, and corrosion rate values of the gel electrolyte containing PANi 0.6 wt% prepared at different stirring times.

Stirring time/min.	R_s (Ω)	R_{ct} (Ω)	W	E_{corr} (V)	I_{corr} (mA)	Corrosion Rate (mpy)
15	**1.283**	**439.5**	**0.000942**	**-0.578**	**0.0246**	**112.2**
30	**1.101**	**165.3**	**0.001096**	**-0.585**	**0.0222**	**101.3**
60	**1.0496**	**469.4**	**0.001264**	**-0.578**	**0.0221**	**100.8**
90	**0.9061**	**299.2**	**0.001198**	**-0.580**	**0.0243**	**111.0**
120	**0.9498**	**273.3**	**0.001859**	**-0.578**	**0.0259**	**118.3**
150	**1.262**	**321.4**	**0.001277**	**-0.582**	**0.0238**	**108.9**

The Nyquist EIS results presented in Figure 3.14b further support the CV results for PANi/G-doped gel electrolyte prepared at different stirring times. The gel electrolyte mixed for 150 min exhibits the lowest charge transfer resistance value (R_{ct}) with relatively low solution resistance (R_s), suggesting the enhancement of interfacial charge transfer and ionic conductivity within the gel matrix. Similarly, in PANi additive behavior, the shorter mixing time (15 - 30 min) decreases both R_s and R_{ct}; this can be attributed to the insufficient mixing, incomplete gel network formation, and non-uniform particle dispersion within the gel structure, causing hindered ionic transport. In contrast, at higher stirring time (180 min), the R_s and

R_{ct} tend to decrease, indicating that the longer the mixing time, the more inhomogeneous the gel network formation as well as the agglomeration of PANi encapsulated with graphite particles, leading to decreases in the electrochemical activity of the gel system as well as the capacities. Table 3.8 summarizes R_s, R_{ct}, and Warburg data.

Table 3.8 R_s, R_{ct}, I_{corr}, and corrosion rate values of the PANi/G-doped gel electrolyte prepared at different stirring rates.

Stirring time/min.	R_s (Ω)	R_{ct} (Ω)	W	E_{corr} (V)	I_{corr} (mA)	Corrosion Rate (mpy)
15	**0.5737**	**200.8**	**2.859**	**-0.583**	**0.056**	**25.12**
30	**2.272**	**238.1**	**3.141**	**-0.513**	**0.005**	**2.71**
60	**0.9295**	**313.1**	**2.104**	**-0.578**	**0.017**	**8.121**
90	**0.7945**	**188.1**	**2.615**	**-0.584**	**0.013**	**5.938**
120	**0.7776**	**169.7**	**4.27**	**-0.582**	**0.029**	**13.31**
150	**0.5885**	**162.3**	**2.652**	**-0.584**	**0.006**	**2.995**
180	**0.5819**	**213.2**	**2.487**	**-0.585**	**0.034**	**15.8**

For PPy-modified gel electrolytes, the results shown in Figure 3.14c are for gel systems prepared at different stirring times. The longer mixing times (120 and 150 min) exhibit the highest charge transfer resistance, indicating that the gel structure was disrupted as a result of PPy agglomeration within the gel structure and the formation of a thicker gel structure, leading to hindered ionic mobility within the electrode/electrolyte interface as well as a decrease in the electrochemical performance. On the other hand, the short to moderate stirring times shows similar behavior; these findings can be attributed to the improved dispersion of PPy particles within the gel structure leading to enhanced ionic mobility at the electrode/electrolyte interface. The optimum charge transfer resistance Rct was observed at a stirring time of 60 min, indicating the balance between enhanced gel

network formation as well as ionic mobility through the interface, resulting in the optimum electrochemical behavior as shown in the 0.8 wt% CV results.

Table 3.9 The R_s, R_{ct}, E_{corr}, and I_{corr} values obtained for fumed silica-based gel electrolyte consisting of 0.8 wt% of PPy at different stirring times

PPy stirring time (min)	R_s (Ω)	R_{ct} (Ω)	W	E_{corr} (V)	I_{corr} (µA)	Corrosion Rate (mpy)
15	**1.239**	**189.1**	**0.003215**	**-583.0**	**107.0**	**48.78**
30	**0.7017**	**205.8**	**0.0041**	**-578.0**	**82.00**	**37.46**
60	**0.7541**	**157.8**	**0.002795**	**-572.0**	**71.10**	**32.50**
90	**0.783**	**206.2**	**0.003013**	**-560.0**	**93.80**	**42.85**
120	**0.9606**	**228.2**	**0.001526**	**-537.60**	**188.0**	**85.90**
150	**0.7808**	**284.1**	**0.00195**	**-561.0**	**204.0**	**93.00**

Figure 3.14d illustrates the EIS results of PTF gel systems. The optimum values of both Rs and Rct were recorded at a stirring time of 30 minutes, indicating that the enhanced balance between ionic transport at the electrode/electrolyte interface and ionic mobility within the gel matrix was achieved at this stirring time as a result of improved PTF dispersion as well as well-connected pore formation of the gel network and increasing ion diffusion pathways. For other EIS results at shorter and longer stirring times, the R_{ct} is higher due to a lack of PTF dispersion within the gel structure as a result of insufficient or excessive mixing leading to a lack of or non-uniform gel network formation and decreasing the ionic transport through the Pb/gel interface as well as lowering the ionic mobility. In other words, the electrochemical performance decreases with the agglomeration or non-uniform dispersion of PTF additive material with the gel structure. The EIS results are summarized in Table 3.10.

Table 3.10 The R_s, R_{ct}, E_{corr}, and I_{corr} values obtained for fumed silica-based gel electrolyte consisting of 0.2 wt% of PTF at different stirring times

Stirring time (min)	R_s (Ω)	R_{ct} (Ω)	W	E_{corr} (mV)	I_{corr} (µA)	Corrosion Rate (mpy)
15	**0.7651**	**603.9**	**0.00113**	**-592.0**	**41.80**	**19.11**
30	**0.4849**	**271.4**	**0.004011**	**-606.0**	**30.20**	**13.81**
60	**0.9425**	**461.3**	**0.001733**	**-589.0**	**26.50**	**12.11**
90	**0.7037**	**427.2**	**0.001837**	**-596.0**	**38.00**	**17.39**
120	**0.9767**	**560.2**	**0.001229**	**-578.0**	**39.40**	**17.98**
150	**0.7174**	**589.2**	**0.001127**	**-587.0**	**101.0**	**46.36**

For PTF/G-doped gel electrolyte, the behavior is quite different from PTF-doped gel electrolyte. The optimum stirring time is 30 min, which is similar to the PTF additive as shown in Figure 3.14e The difference is at lower and moderate stirring times, which shows enhanced electrochemical performance for the same stirring times for PTF. The difference can be attributed to the presence of graphite particles, which improve gel homogeneity and additive dispersion and result in the formation of a well-connected gel matrix. At higher stirring times, the electrochemical performance drops down due to lack of PTF/G dispersion and the agglomeration of additive particles within the gel structure, leading to a non-uniform gel matrix and decreasing ionic transport as well as increasing the charge transfer resistance. Table 3.11 Summarized the R_s, R_{ct}, and Warburg data for PTF/G gel systems.

Table 3.11 The R_s, R_{ct}, E_{corr}, and I_{corr} values obtained for fumed silica-based gel electrolyte consisting of 0.2 wt% of PTF/G composite at different stirring times.

Stirring time (min)	R_s (Ω)	R_{ct} (Ω)	W	E_{corr} (mV)	I_{corr} (µA)	Corrosion Rate (mpy)
15	**0.8459**	**427.2**	**0.001152**	**-547.0**	**47.50**	**21.71**
30	**0.7501**	**298.1**	**0.000966**	**-525.0**	**23.10**	**10.57**
60	**0.6315**	**353.1**	**0.001249**	**-551.0**	**42.02**	**18.19**
90	**0.6717**	**447.2**	**0.0008244**	**-531.0**	**35.30**	**16.15**
120	**0.8704**	**465.6**	**0.001049**	**-538.0**	**33.70**	**15.40**
150	**0.6628**	**586.8**	**0.0007321**	**-544.0**	**24.80**	**11.35**

Figure 3.14e illustrates the overall electrochemical performance of gel systems with different additive materials and prepared with specific stirring time. PPy and PANi/G-modified gel electrolytes have slight similar R_{ct} values, then PTF-doped gel electrolyte comes second in order. The PANi and PTF/G gel electrolytes show the lowest electrochemical performance. These findings support the CV analysis results, indicating that PPy and PANi/G additive have enhanced interaction with fumed silica and sulfuric acid resulting in improving the redox activity as well as the ionic transfer and ion diffusion pathways.

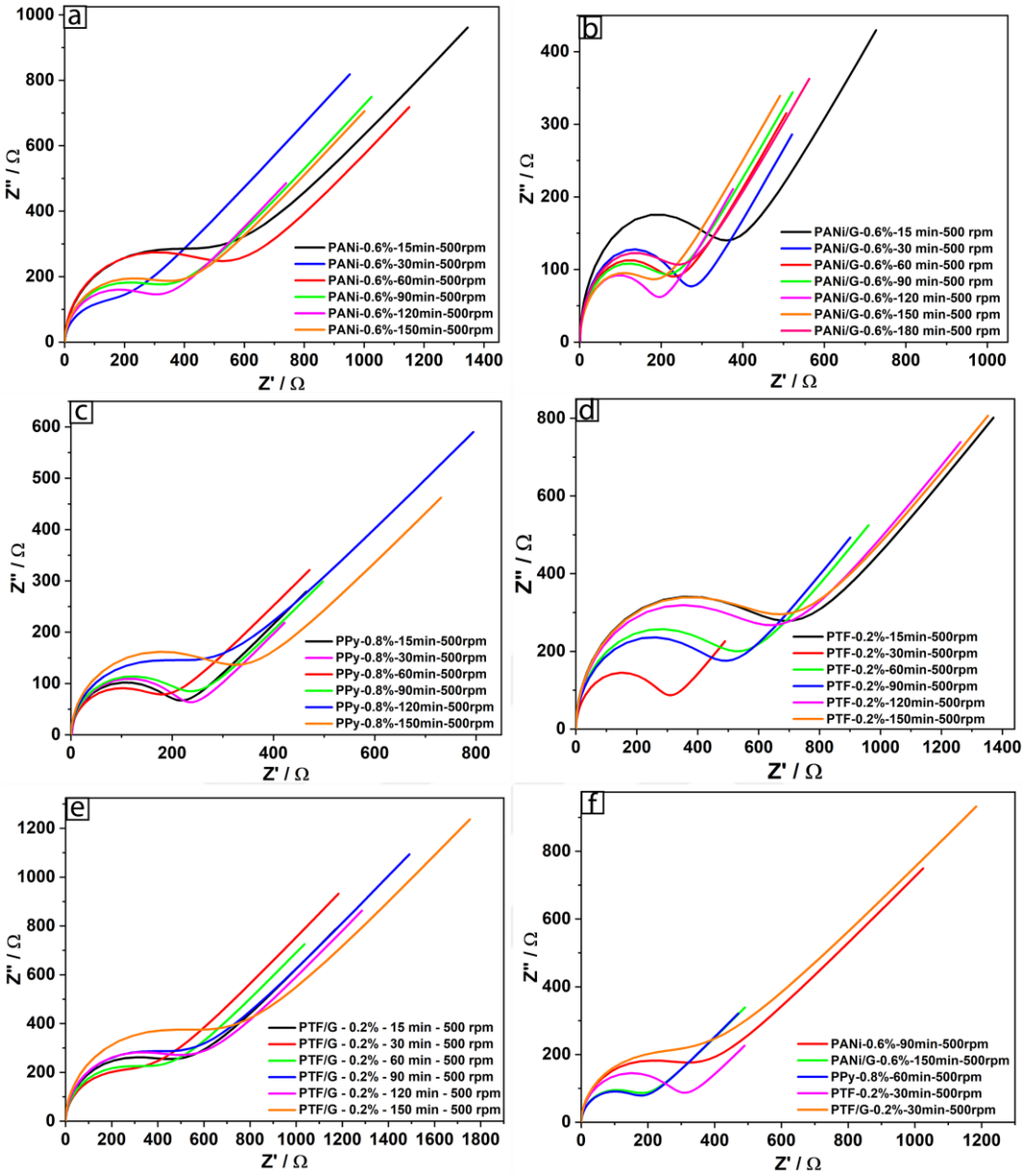


Figure 3.14 Electrochemical impedance spectroscopy for gel systems prepared at 500 rpm with different stirring time containing (a) 0.6 wt% of PANi, (b) 0.6 wt% of PANi/G composite, (c) 0.8 wt% of PPy, (d) 0.2 wt% of PTF, and (e) 0.2 wt% of PTF /G composite

The corrosion behavior of the gel electrolytes prepared at different stirring times was assessed using electrochemical techniques, including potentiodynamic polarization as shown in Figure 3.15 The Tafel test provides insight into the electrochemical stability and corrosion resistance of the gel electrolytes at various stirring durations. Regarding corrosion behavior, the corrosion rate (mpy) and corrosion current (I_{corr}) values provide a direct indication of the stability of the electrolyte system over time. Figure 15a illustrates the corrosion activity of PANi-

modified gel electrolytes prepared at different stirring times. As summarized in Table 3.7, the corrosion current density and corrosion rate vary moderately with stirring time; this variance reflects the changes in gel homogeneity and structure stability. The gel electrolyte prepared at 90 min exhibits a balanced corrosion behavior of I_{corr}, E_{corr}, and corrosion rate, indicating that the addition of PANi at different stirring times has a passivation effect during charge/discharge, which provides protection to the electrodes and decreases the corrosion. These findings show that the PANi-modified gel electrolytes prepared using different stirring times have similar benefits of corrosion protection during electrochemical activity. Figure 3.15a illustrates the corrosion activity of PANi-modified gel electrolytes prepared at different stirring times. As summarized in Table 3.7, the corrosion current density and corrosion rate vary moderately with stirring time; this variance reflects the changes in gel homogeneity and structure stability. The gel electrolyte prepared at 90 min exhibits a balanced corrosion behavior of I_{corr}, E_{corr}, and corrosion rate, indicating that the addition of PANi at different stirring times has a passivation effect during charge/discharge, which provides protection to the electrodes and decreases the corrosion. These findings show that the PANi-modified gel electrolytes prepared using different stirring times have similar benefits of corrosion protection during electrochemical activity. Figure 3.15b presents the Tafel results of PANi/G composite-doped gel electrolytes at different stirring times; the gel systems prepared at short and long stirring times show slightly higher corrosion rates and current density, indicating that the short and long stirring times have direct effects on gel structures and homogeneity, which affects the electrodes' surfaces and increases the corrosion effect. At moderate stirring times, the corrosion rates decrease as well as the I_{corr} as a result of the protective role of the PANi/G composite, which enhances the gel structure. The results of the PANi/G composite compared to the PANi results at different stirring times show the additional positive effect of graphite within the gel structure. The I_{corr}, E_{corr}, and corrosion rates are listed in Table 3.8. The corrosion analysis results in Figure 3.15c revealed that the 60 minute stirring time resulted in the lowest I_{corr} value, indicating the lowest corrosion rate for the electrodes in this gel electrolyte. It was observed that other I_{corr} values exhibited similar trends, with short to medium stirring times producing comparable outcomes. However, as the stirring time increased beyond 90 minutes, particularly at 120 and 150 minutes, the I_{corr} values significantly increased. This

suggests that excessive stirring time had a detrimental effect on the corrosion rate, likely due to the over-dispersion of the gel, which could lead to increased internal resistance and inhomogeneity, impacting the electrode's performance. Table 3.9 presents the EIS and Tafel curve values for different stirring times. The corrosion results of PTF and PTF/G composite modified gel electrolytes are presented in Figures 3.15d and 3.15e. For PTF gel systems at different stirring times, a reduction in corrosion rates and current density was observed at moderate stirring time (30–60 min) in comparison to short stirring time (15 min), indicating better gel homogeneity and PTF particle dispersion; however, at excessive stirring time (150 min), the I_{corr} and corrosion rate sharply increased, suggesting the breakdown of the gel network and poorer surface protection. In the case of using PTF/G composite as an additive to the gel systems at different stirring times, the corrosion behavior is clearly enhanced. The lowest I_{corr} and corrosion rates were observed at 30 and 150 min, presenting that the composite particles of PTF/G help form a more conductive and protective network that suppresses corrosion of the electrode surface. The Tafel curves confirm this trend by showing lower I_{corr} for PTF/G than PTF at comparable stirring times. For PTF/G, it exhibits better corrosion resistance and wider processing tolerance, while PTF is more sensitive to over-stirring. Tables 3.10 and 3.11 summaries the I_{corr}, E_{corr}, and corrosion rates of PTF and PTF/G gel systems at different stirring times.

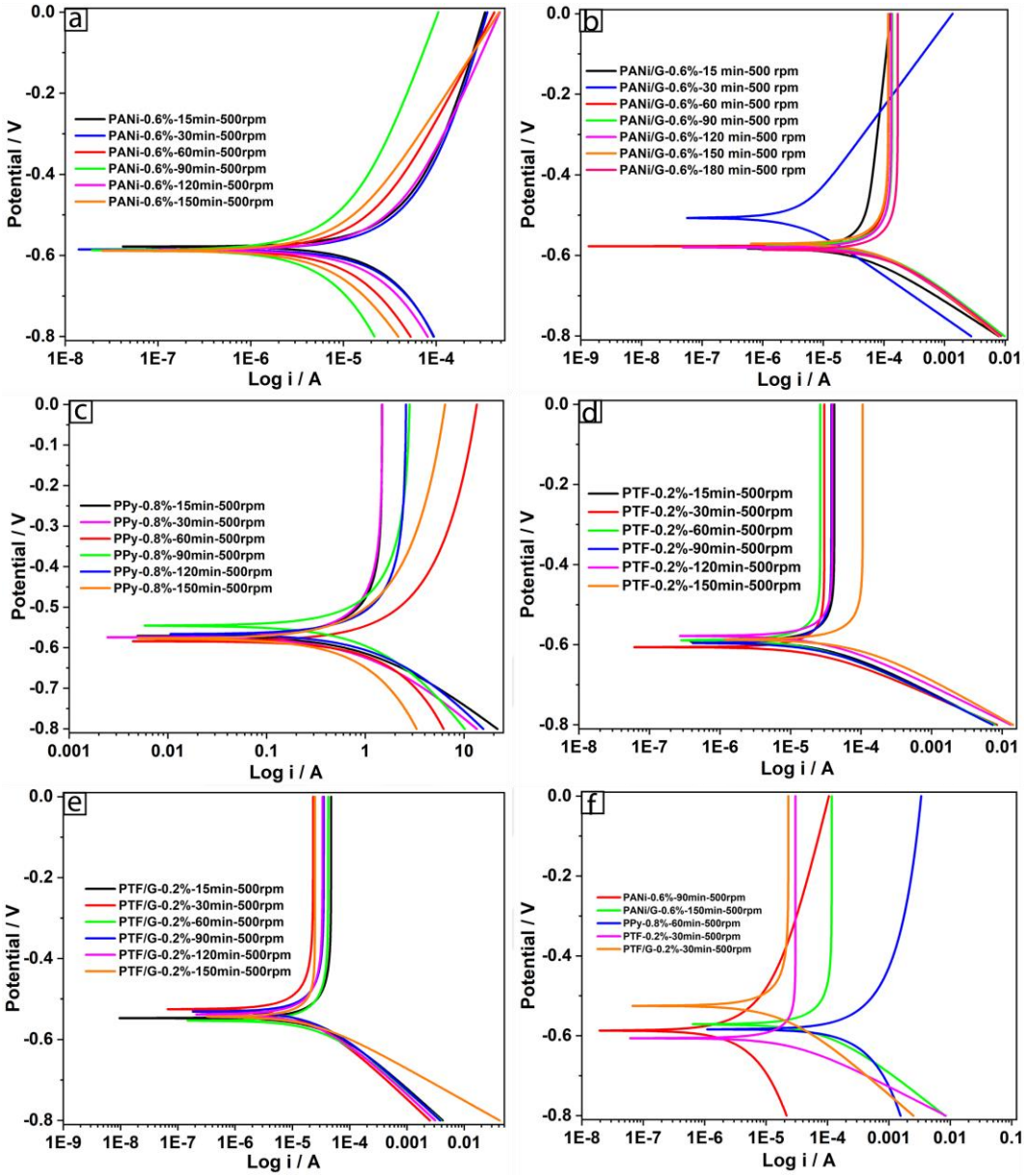


Figure 3.15 Tafel polarization analysis for gel systems prepared at 500 rpm with different stirring time containing (a) 0.6 wt% of PANi, (b) 0.6 wt% of PANi/G composite, (c) 0.8 wt% of PPy, (d) 0.2 wt% of PTF, and (e) 0.2 wt% of PTF /G composite.

3.3.4 Optimization of Stirring Rates for the Preparation of Conductive Polymers and Conductive Polymers Composites-Containing Fumed Silica-Based Gel Electrolytes

The final part of gel optimization, studying the effect of different stirring rates (250, 500, 750, and 1000 rpm) on the electrochemical behavior of the gel electrolyte system containing different additives with specific content and stirring time, was investigated. Figure 3.16 presents the electrochemical cyclic voltammetry results obtained for the gel system under these varying stirring rates. For gel systems modified with different additive materials, the optimum redox activity was obtained at a stirring rate of 500 rpm for all systems, indicating good formation of a 3D gel network with well-connected ion diffusion pathways. While at lower and higher stirring rates the CV results show similar behavior, suggesting a lack of dispersion leading to less homogeneity of gel structure or excessive stirring leading to the disruption of the gel network and/or particle agglomeration within the gel structures. For PANi/G electrochemical CV results shown in Figure 3.16b, the use of 1000 rpm causes excessive stirring, resulting in non-homogeneous gel structure and particle agglomeration, while the low and moderate stirring rates have slight differences between their results.

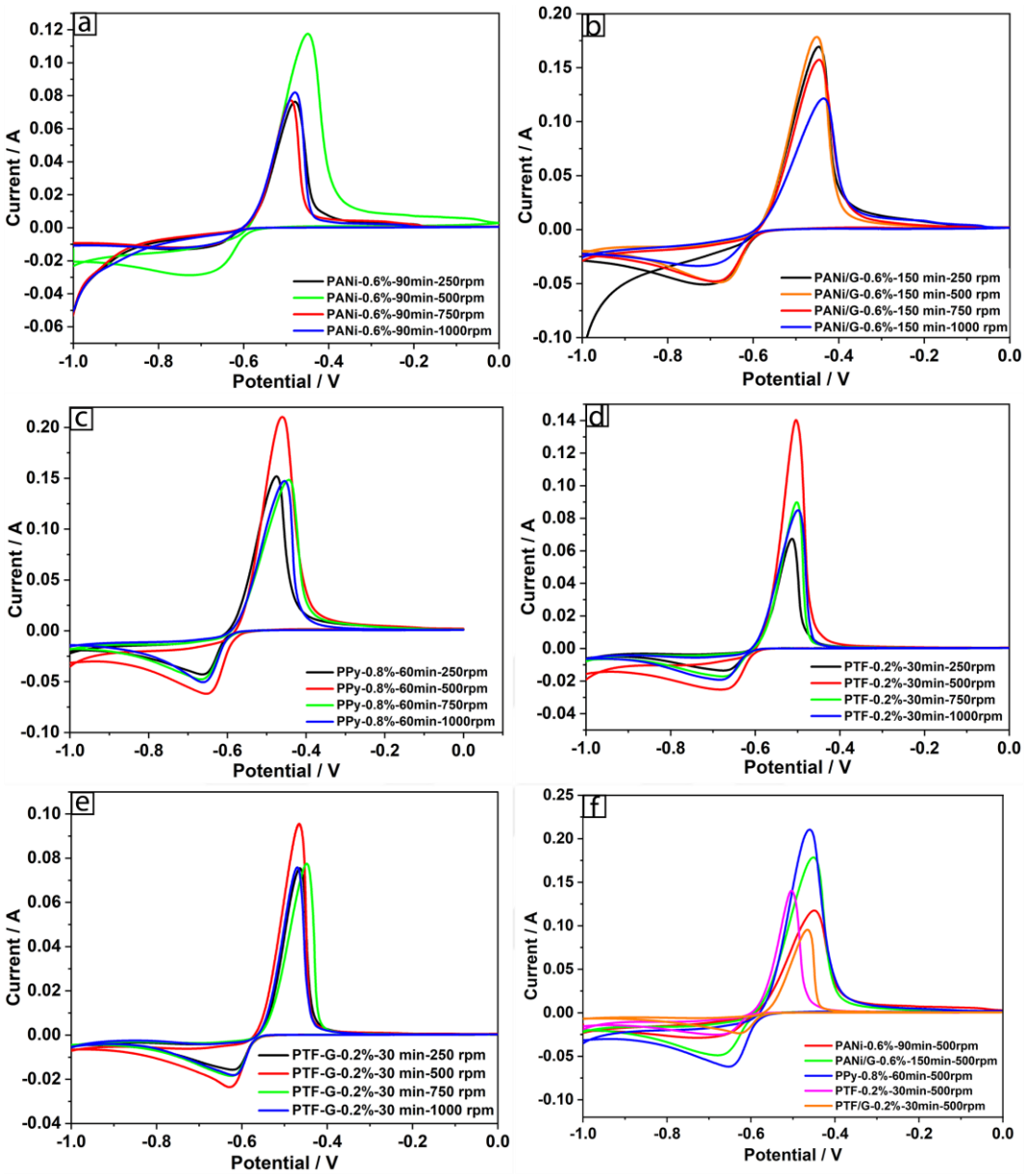


Figure 3.16 Cyclic voltammetry analysis for gel systems prepared with different stirring rates containing (a) 0.6 wt% of PANi for 90 min, (b) 0.6 wt% of PANi/G composite for 150 min, (c) 0.8 wt% of PPy for 60 min, (d) 0.2 wt% of PTF for 30 min, and (e) 0.2 wt% of PTF /G composite for 30 min.

Electrochemical impedance spectroscopy (EIS) analysis of the gel electrolytes prepared at different stirring rates further corroborated the cyclic voltammetry (CV) results; the lowest charge transfer resistance R_{ct} and solution resistance R_s were obtained at 500 rpm, suggesting that the gel network formation and particle dispersion improved at this stirring rate. Figures 3.17a, 3.17c, and 3.17e show that PANi, PPy, and PTF/G additives have slight differences between different stirring rates, indicating that the stirring rate has a small effect on material dispersion and

gel formation and interrupts the ion diffusion pathways slightly. On the other hand, for PANi/G and PTF, the effect of different stirring rates is higher, as shown in figures 3.17b and 3.17d; the effect of low and excessive stirring disrupts the gel formation and/or particles are less dispersed or agglomerated with the gel structure, which affects the charge transfer and ion mobility across the electrode/electrolyte interface. Tables 3.12, 3.13, 3.14, 3.15, and 3.16 summarize the R_s, R_{ct}, and Warburg results of different gel systems with different additive materials.

Table 3.12 R_s, R_{ct}, I_{corr}, and corrosion rate values of the PANi-doped gel electrolyte prepared at different stirring rates

Stirring rate / rpm	R_s (Ω)	R_{ct} (Ω)	W	E_{corr} (V)	I_{corr} (mA)	Corrosion Rate (mpy)
250	1.219	391.9	0.001293	-0.577	0.0280	128.1
500	0.9061	299.2	0.001198	-0.580	0.0243	111.0
750	1.287	473.6	0.001493	-0.579	0.0358	163.8
1000	1.048	497.4	0.001864	-0.583	0.0251	114.6

Table 3.13 R_s, R_{ct}, I_{corr}, and corrosion rate values of the PANi/G-doped gel electrolyte prepared at different stirring rates

Stirring rate / rpm	R_s (Ω)	R_{ct} (Ω)	W	E_{corr} (V)	I_{corr} (mA)	Corrosion Rate (mpy)
250	0.7437	182.8	0.002465	-0.585	0.015	7.308
500	0.5885	162.3	0.002652	-0.584	0.006	2.995
750	0.9356	172.8	0.003804	-0.582	0.031	14.16
1000	0.6989	246.4	0.002178	-0.583	0.047	21.65

Table 3.14 The R_s, R_{ct}, E_{corr} and I_{corr} values obtained for fumed silica-based gel electrolyte consisting of 0.8 wt% of PPy at different stirring rates

PPy stirring rate (rpm)	R_s (Ω)	R_{ct} (Ω)	W	E_{corr} (mV)	I_{corr} (µA)	Corrosion Rate (mpy)
250	1.262	321.4	0.001277	-564.0	71.30	32.60
500	0.7541	157.8	0.002795	-572.0	71.10	32.50
750	0.6996	253.1	0.002492	-566.0	73.50	33.60
1000	0.7611	287.4	0.002245	-577.0	76.10	34.79

Table 3.15 The R_s, R_{ct}, E_{corr} and I_{corr} values obtained for fumed silica-based gel electrolyte consisting of 0.2 wt% of PTF at different stirring rates

Stirring rate (rpm)	R_s (Ω)	R_{ct} (Ω)	W	E_{corr} (mV)	I_{corr} (µA)	Corrosion Rate (mpy)
250	0.8068	676.1	0.0008389	-578.0	29.70	13.57
500	0.4849	271.4	0.004011	-606.0	30.20	13.81
750	0.7072	509.9	0.001129	-583.0	36.20	16.55
1000	0.7689	673.3	0.0009284	-595.0	36.60	16.72

Table 3.16 The R_s, R_{ct}, E_{corr} and I_{corr} values obtained for fumed silica-based gel electrolyte consisting of 0.2 wt% of PTF/G composite at different stirring rates

Stirring rate (rpm)	R_s (Ω)	R_{ct} (Ω)	W	E_{corr} (mV)	I_{corr} (µA)	Corrosion Rate (mpy)
250	0.6224	446.5	0.0008474	-534,0	43,60	19,94
500	0.7501	298.1	0.000966	-525.0	23.10	10.57
750	0.7649	570.1	0.0007718	-522,0	32,10	14,67
1000	0.6395	579	0.000753	-512,0	15,80	7,206

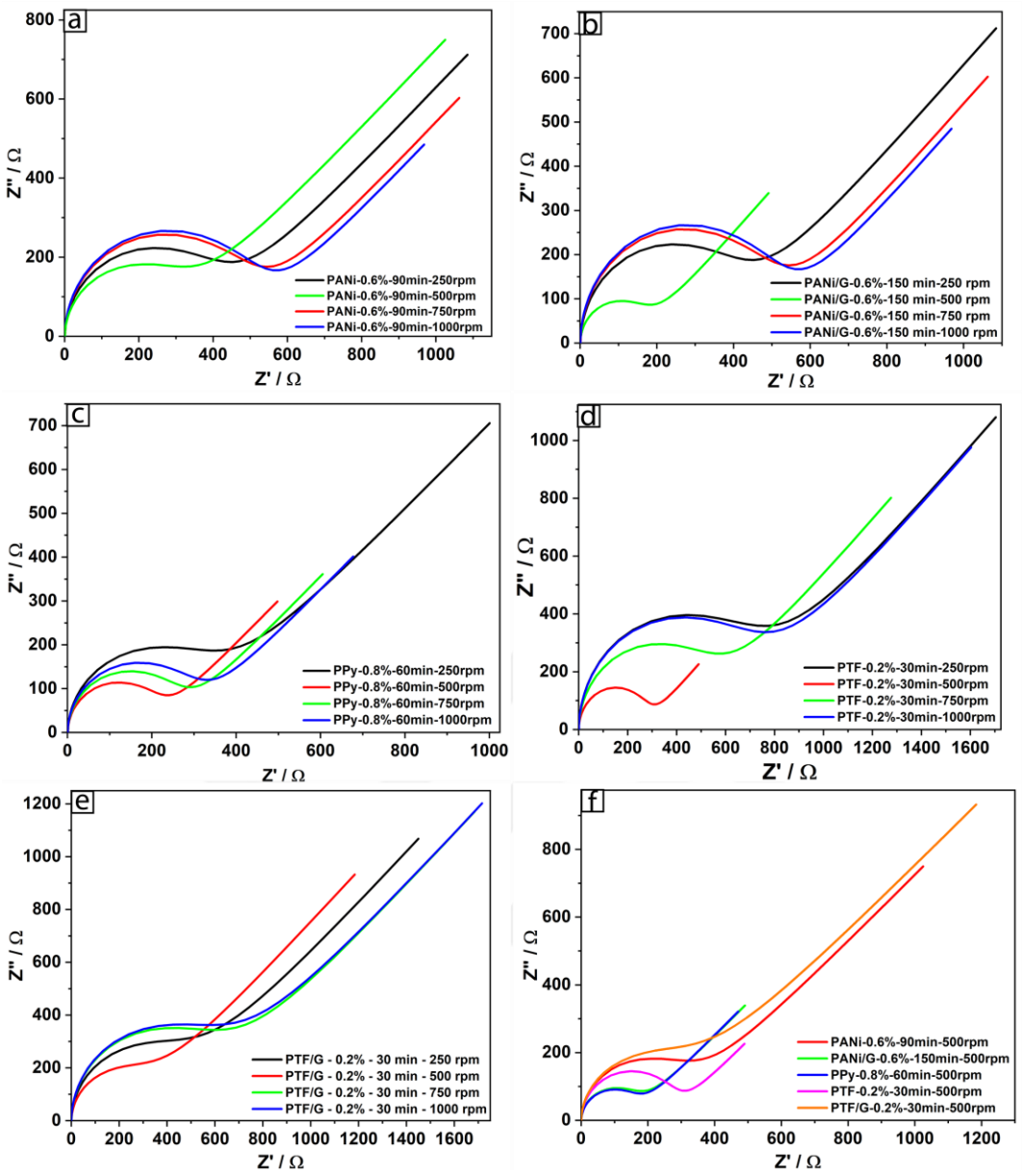


Figure 3.17 Electrochemical impedance spectroscopy (EIS) analysis for gel systems prepared with different stirring rates containing (a) 0.6 wt% of PANi for 90 min, (b) 0.6 wt% of PANi/G composite for 150 min, (c) 0.8 wt% of PPy for 60 min, (d) 0.2 wt% of PTF for 30 min, and (e) 0.2 wt% of PTF /G composite for 30 min

Figure 3.18 illustrates the Tafel polarization results; the curves and corresponding corrosion parameters clearly show that the additive material type and stirring rates strongly influence the corrosion behavior of the gel electrolytes. The PANi-doped gel system exhibits the lowest corrosion resistance, with higher corrosion activity and noticeable sensitivity to stirring rate. On the other hand, PANi/G-doped gel electrolyte improves corrosion protection through the formation of a more stable

conductive gel network, although excessive stirring affects corrosion resistance. For PPy-modified gel electrolytes display moderate corrosion resistance with relatively limited dependence on stirring rate. In the case of PTF additive materials, the corrosion behavior shows strong dependence on stirring conditions; at 500 rpm the gel network formed a protecting layer that improves the corrosion resistance of the electrodes, while low and excessive stirring rates reduce gel stability. Among all systems, gel electrolyte containing PTF/G demonstrates the most stable and protective behavior, maintaining lower corrosion rates through different stirring rates, suggesting that the synergistic effect of the PTF/G composite enhances gel structure as well as corrosion resistance. Tables 3.12, 3.13, 3.14, 3.15, and 3.16 summarize the I_{corr}, E_{corr}, and corrosion rates results of different gel systems with different additive materials.

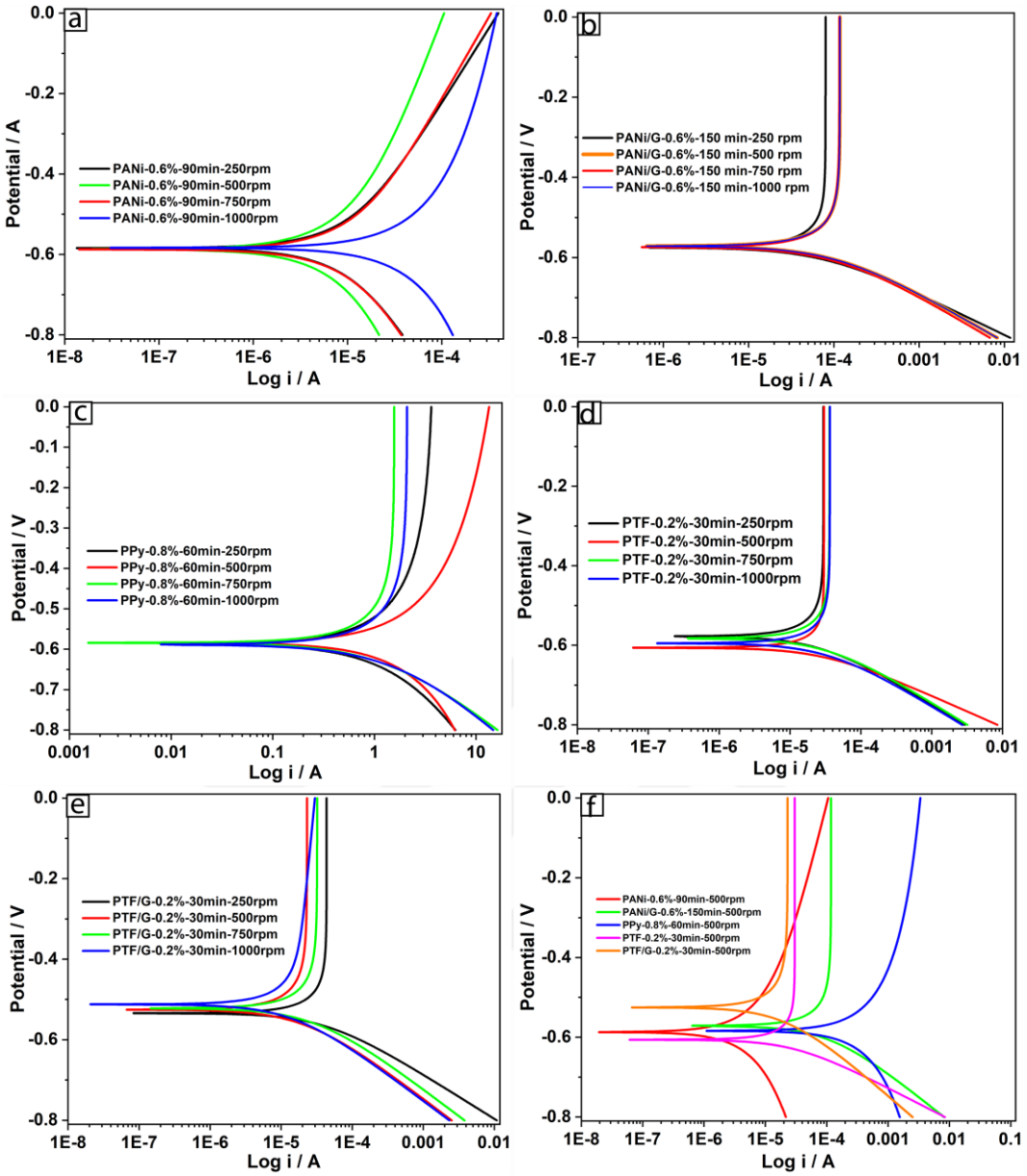


Figure 3.18 TAFEL polarization analysis for gel systems prepared with different stirring rates containing (a) 0.6 wt% of PANi for 90 min, (b) 0.6 wt% of PANi/G composite for 150 min, (c) 0.8 wt% of PPy for 60 min, (d) 0.2 wt% of PTF for 30 min, and (e) 0.2 wt% of PTF /G composite for 30 min

3.4 Battery Test for Polymers and Conductive Polymers Composites-Containing Fumed Silica-Based Gel Electrolyte

Galvanostatic charge/discharge (GCD) results shown in Figure 3.19 demonstrate that the discharge capacity and cycling stability of the lead acid/gels cells are electrolyte structure dependence (aqueous vs gel type) and additive chemistry. As shown in Figure 3.19a and summarized in Table 3.17, the sulfuric acid electrolyte exhibits the lowest initial discharge capacity of 35 mAh g^{-1} at current density 5 mA g^{-1} as well as the poorest long-term cycling stability, the retaining capacity only 50% after 200 cycles at a current density 10 mA g^{-1}. This unstable and weak behavior suggested that a sever polarization and non-uniform reaction distribution in the aqueous solution as a result to acid stratification as well as unstable interfacial processes resulting in inefficient sulfation/desulfation of lead sulfate and accelerate performance decay. Converting the electrolyte to a fumed silica-based gel substantially improves the initial capacity to 45.75 mAh g^{-1} and increases retention capacity up to 62%, confirming that the 3D gel network suppresses stratification and stabilizes ionic pathways; however, the fumed silica-based gel remains limited by its low electronic conductivity, which maintains noticeable polarization and still allows progressive capacity loss during cycling.

The introduction of conductive additives into the gel electrolyte produces a further, marked enhancement in both initial capacity and cycling stability. The PANi gel electrolyte (0.6 wt%) shows an initial capacity of 52.75 mAh g^{-1} and retains 82% capacity after cycling. This improvement is consistent with PANi forming a conductive network within the gel structure, which enhances the charge transfer processes at the electrode/electrolyte interface and supports more uniform lead sulfate ($PbSO_4$) formation and reduction. In the case of introducing PANi/G composite additive material (PANi/G, 0.6 wt%), the initial capacity remains comparable 51.52 mAh g^{-1}, but the retention capacity increases to 87%, indicating that the incorporation of graphite-PANi composite improves the structural and electrochemical stability during repeated cycling by strengthening electron percolation pathways and reducing degradation-driven polarization. A similar behavior is observed for PPy conductive polymer (0.8 wt%), a capacity of 50.98 mAh g^{-1} and 86% retention capacity were recorded; this suggests that the addition

of PPy powder improves lead sulfate reversibility and maintains stable cycling even though its initial capacity is not maximized. The PTF-doped gel electrolyte (0.2 wt%) provides a 51.3 mAh g^{-1} and a higher retention capacity of 88%, implying that PTF contributes strongly to long-term cycling stability, this might be attributed to improvement in gel structure and suppressing passivation-related loses during cycling. The most noticeable performance improvement is obtained with the addition of PTF/G composite gel electrolyte (0.2 wt%), which exhibits the highest initial discharge capacity of 55.75 mAh g^{-1} and the highest retention capacity of 91% after 200 cycles. This enhanced behavior is also supported by the GCD curves in figure 3.19a, where composite-modified gel electrolytes display longer discharge time and reduced voltage hysteresis, indicating lower polarization and improved contribution of active material. The GCD results show that optimizing cycling performance was done not only by enhancing charge transfer but also sustaining efficient ionic transport and preserving gel integrity. Overall, the combined evidence from the galvanostatic charge/discharge curves in Figure 3.19a and cycling retention/coulombic efficiency behavior in Figure 3.19b, and the quantitative capacity-retention values summarized in Table 3.17 establishes a clear performance progression: sulfuric acid < fumed silica-based gel < conductive polymers gels < conductive polymers/composite gels, with PTF/G providing the most balanced enhancement in capacity output and long-term durability.

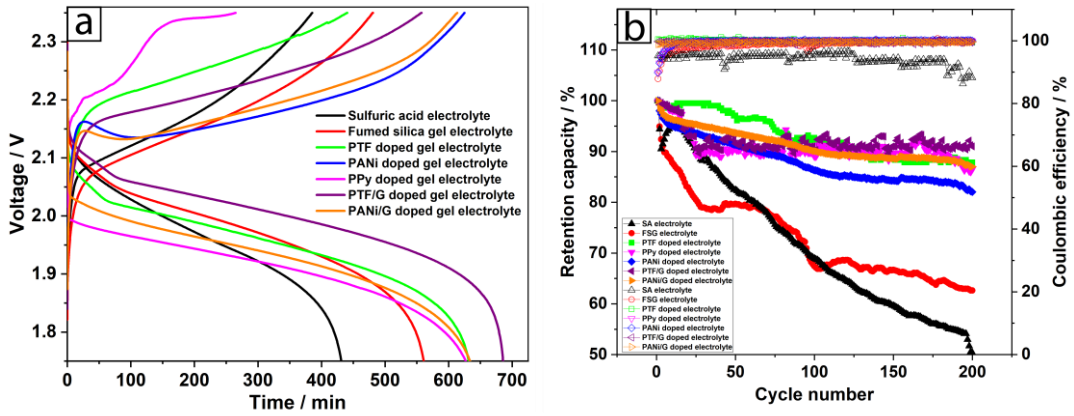


Figure 3.19 Galvanostatic charge/discharge test results for different electrolyte systems: (a) Initial capacities of sulfuric acid electrolyte, fumed silica-based electrolyte, PANi-doped gel electrolyte (0.6 wt% PANi, 90 minutes stirring at 500 rpm), PANi/G-doped gel electrolyte (0.6 wt% PANi/G, 150 minutes stirring at 500 rpm), PPy-doped gel electrolyte (0.8 wt% PPy, 60 minutes stirring at 500

rpm), PTF-doped gel electrolyte (0.2 wt% PTF, 30 minutes stirring at 500 rpm), and PTF/G-doped gel electrolyte (0.2 wt% PTF/G, 30 minutes stirring at 500 rpm). (b) Long-cycle test performance, showing coulombic efficiency and retention capacity for sulfuric acid electrolyte, fumed silica-based electrolyte, and Conductive polymers and conductive polymers composites additives fumed silica-based gel electrolyte.

Table 3.17 Initial Capacity and Retention Capacity for different gel systems with different conductive additives.

Additive	Content %	R_{ct} (Ω)	W	Initial capacity mAh g^{-1} at 5 mA g^{-1}	Retention capacity % at 10 mA g^{-1}
SA	**0**	**0**		**35**	**50**
FSG	**0**	**0**	**0.001365**	**45.75**	**62**
PANi	**0.6**	**299.2**	**0.001198**	**52.75**	**82**
PANi/G	**0.6**	**162.3**	**0.002652**	**51.52**	**87**
PPy	**0.8**	**157.8**	**0.002795**	**50.98**	**86**
PTF	**0.2**	**271.4**	**0.004011**	**51.3**	**88**
PTF/G	**0.2**	**298.1**	**0.000966**	**55.75**	**91**

4
CONCLUSION

4.1 Conclusion

In this work, a gel electrolyte system was developed using sulfuric acid, fumed silica, and conductive polymers and its graphite composites as conductive additive for valve-regulated lead-acid (VRLA) batteries. The optimization of conductive polymer and their graphite synthesis through electrochemical analysis revealed that the optimal contents, stirring time and rate obtained PANi (0.6 wt%, 90 min, and 500 rpm), PANi/G (0.6 wt%, 150 min, and 500 rpm), PPy (0.8 wt%, 60 min, and 500 rpm), PTF (0.2 wt%, 30 min, and 500 rpm), and PTF/G (0.2 wt%, 30 min, and 500 rpm). Electrochemical characterization demonstrated that the incorporation of these additives significantly improved battery performance by enhancing the electrical conductivity of the gel, facilitating ion charge transfer, and reducing both solution resistance (R_s) and charge transfer resistance (R_{ct}) as shown in Table 4.1.

Charge–discharge tests conducted at a current density of 5 mA g^{-1} showed that the initial specific capacities values for each gel electrolyte system (PANi, PANi/G, PPy, PTF, and PTF/G), the fumed silica-based gel electrolyte, and the flooded sulfuric acid electrolyte were 52.75, 51.52, 50.98, 51.3, 55.75, 44.01, and 33 mAh g^{-1}, respectively. Figure 4.1a presents specific capacity results of different gel systems doped with CPs and their graphite composites. Long-cycle charge–discharge testing further demonstrated the excellent stability of the gel electrolyte systems especially the PTF/G-doped gel, which retained 91% of its initial specific capacity after 200 cycles. Other CPs-doped gel systems recorded the retention in initial capacity as follow, PANi with 82%, PANi/G 87%, PPy 86%, and PTF 88% after 200 cycles. The addition of Cps and CPs/G composites to the gel electrolyte enhanced overall battery performance by 31 - 37% and 11 - 18% compared to the

flooded sulfuric acid electrolyte and the fumed silica-based gel electrolyte, respectively. Figure 4.1b shows the retention in initial capacity for different doped gel systems. The improved performance can be attributed to the conductive nature of CPs and graphite, which promotes efficient charge transport and ion mobility while maintaining the mechanical stability of the gel structure.

Table 4.1 Different gel systems with different preparation parameters and their results

Additive %	Stirring time / min	Stirring Rate / rpm	R_s / Ω	R_{ct} / Ω
FSG	**30**	**500**	**1.373**	**364.9**
PANi 0.6%	**90**	**500**	**0.9061**	**299.2**
PANi/G 0.6%	**150**	**500**	**0.5885**	**162**
PPy 0.8%	**60**	**500**	**0.7541**	**157.8**
PTF 0.2%	**30**	**500**	**0.4849**	**271.4**
PTF/G 0.2%	**30**	**500**	**0.7501**	**298.1**

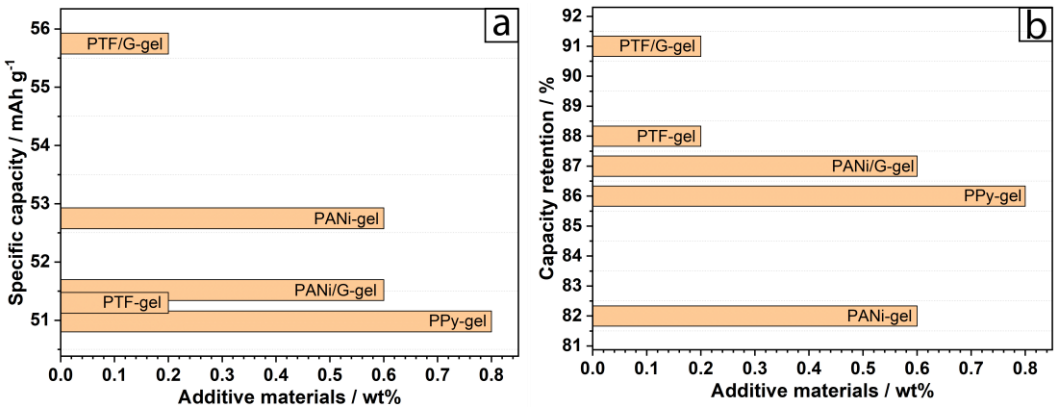


Figure 4.1 VRLA gel electrolytes. a) specific capacity with different additive materials, b) capacity retention with different additive materials.

The electrochemical performance can be summarized as follows.

- The polypyrrole and polyaniline/graphite-doped gel electrolyte demonstrated lowest charge transfer resistance in comparison to the other gel electrolyte systems, while polythiophene-doped gel electrolyte exhibits the lowest solution resistance. The overall GCD behavior of these gels show moderate cycling stability.
- Polythiophene/graphite-doped gel electrolyte demonstrated moderate electrochemical performance of $_{Rs}$ and R_{ct} while exhibiting exceptional cycling stability, and the highest specific capacity.
- Polyaniline-doped gel electrolyte demonstrated the lowest electrochemical performance as well as the initial capacity, providing the lowest performance between other gel electrolyte systems, but still enhanced in comparison to fumed silica-based gel electrolyte.

REFERENCES

[1] P. T. Moseley, D. A. J. Rand, and J. Garche, "Lead–acid batteries for future automobiles," in *Lead-Acid Batteries for Future Automobiles*, Elsevier, 2017, pp. 601–618. doi: 10.1016/B978-0-444-63700-0.00021-0.

[2] D. Linden and T. B. Reddy, *Handbook of batteries*, vol. 33, no. 04. McGraw-Hill, 2011. doi: 10.5860/CHOICE.33-2144.

[3] K. A. Vishnumurthy and K. H. Girish, "A comprehensive review of battery technology for E-mobility," *J. Indian Chem. Soc.*, vol. 98, no. 10, p. 100173, Oct. 2021, doi: 10.1016/j.jics.2021.100173.

[4] S. Petrovic, *Battery Technology Crash Course*. Cham: Springer International Publishing, 2021. doi: 10.1007/978-3-030-57269-3.

[5] S. Nazaralizadeh, P. Banerjee, A. K. Srivastava, and P. Famouri, "Battery Energy Storage Systems: A Review of Energy Management Systems and Health Metrics," *Energies*, vol. 17, no. 5, 2024, doi: 10.3390/en17051250.

[6] A. Townsend and R. Gouws, "A Comparative Review of Lead-Acid, Lithium-Ion and Ultra-Capacitor Technologies and Their Degradation Mechanisms," *Energies*, vol. 15, no. 13, p. 4930, Jul. 2022, doi: 10.3390/en15134930.

[7] S. Anuradha, R. Manimegalai, and M. Devasena, "Challenges in Recycling Lead Acid Battery and Lithium-Ion Battery: A Comprehensive Review," *Int. Conf. Smart Syst. Electr. Electron. Commun. Comput. Eng. ICSSEEC 2024 - Proc.*, no. Icsseecc, pp. 101–106, 2024, doi: 10.1109/ICSSEECC61126.2024.10649483.

[8] H. Ibrahim, A. Ilinca, and J. Perron, "Energy storage systems-Characteristics and comparisons," *Renew. Sustain. Energy Rev.*, vol. 12, no. 5, pp. 1221–

1250, 2008, doi: 10.1016/j.rser.2007.01.023.

[9] J. Mitali, S. Dhinakaran, and A. A. A. Mohamad, “Energy storage systems: a review,” *Energy Storage Sav.*, vol. 1, no. 3, pp. 166–216, Sep. 2022, doi: 10.1016/j.enss.2022.07.002.

[10] D. Pavlov, *Lead-acid batteries: Science and technology a handbook of lead-acid battery technology and its influence on the product*. Elsevier, 2017. doi: 10.1016/C2012-0-00146-9.

[11] P. T. Moseley, D. A. J. Rand, and S. Kitaronka, *Lead-Acid Batteries for Future Automobiles*, no. January. Elsevier, 2022. [Online]. Available: https://www.sciencedirect.com/book/edited-volume/9780444637000/lead-acid-batteries-for-future-automobiles

[12] J. O. G. Posada *et al.*, “Aqueous batteries as grid scale energy storage solutions,” *Renew. Sustain. Energy Rev.*, vol. 68, pp. 1174–1182, 2017, doi: 10.1016/j.rser.2016.02.024.

[13] J. Büngeler, E. Cattaneo, B. Riegel, and D. U. Sauer, “Advantages in energy efficiency of flooded lead-acid batteries when using partial state of charge operation,” *J. Power Sources*, vol. 375, no. November 2017, pp. 53–58, 2018, doi: 10.1016/j.jpowsour.2017.11.050.

[14] D. A. J. Rand, P. T. Moseley, J. Garche, and C. D. Parker, *Valve-Regulated Lead-Acid Batteries*, 1st ed. Elsevier, 2004. doi: 10.1016/B978-0-444-50746-4.X5000-4.

[15] A. Mohammedi, D. Rekioua, T. Rekioua, and S. Bacha, “Valve Regulated Lead Acid battery behavior in a renewable energy system under an ideal Mediterranean climate,” *Int. J. Hydrogen Energy*, vol. 41, no. 45, pp. 20928–20938, Dec. 2016, doi: 10.1016/j.ijhydene.2016.05.087.

[16] J. Jung, L. Zhang, and J. Zhang, Eds., *Lead-Acid Battery Technologies*. CRC Press, 2016. doi: 10.1201/b18665.

[17] H. Jafari and M. R. Rahimpour, “Pb Acid Batteries,” in *Rechargeable Batteries: History, Progress, and Applications*, Wiley, 2020, pp. 17–39. doi: 10.1002/9781119714774.ch2.

[18] Y. Nakayama, K. Kishimoto, S. Sugiyama, and S. Sakaguchi, “Micro-

structural design and function of an improved absorptive glass mat (AGM) separator for valve-regulated lead-acid batteries," *J. Power Sources*, vol. 107, no. 2, pp. 192–200, 2002, doi: 10.1016/S0378-7753(01)01005-9.

[19] B. Drenchev, M. Dimitrov, V. Boev, and A. Aleksandrova, "Absorptive glass mat separator surface modification and its influence on the heat generation in valve-regulated lead-acid battery," *J. Power Sources*, vol. 280, pp. 66–73, 2015, doi: 10.1016/j.jpowsour.2015.01.090.

[20] S. S. Misra, S. L. Mraz, J. D. Dillon, and D. B. Swanson, "VRLA Battery with AGM-Gel Hybrid for Superior Performance," *INTELEC, Int. Telecommun. Energy Conf.*, pp. 378–382, 2003.

[21] T. Tantichanakul, O. Chailapakul, and N. Tantavichet, "Influence of fumed silica and additives on the gel formation and performance of gel valve-regulated lead-acid batteries," *J. Ind. Eng. Chem.*, vol. 19, no. 6, pp. 2085–2091, Nov. 2013, doi: 10.1016/j.jiec.2013.03.024.

[22] D. Yu, X. Li, and J. Xu, "Safety regulation of gel electrolytes in electrochemical energy storage devices," *Sci. China Mater.*, vol. 62, no. 11, pp. 1556–1573, Nov. 2019, doi: 10.1007/s40843-019-9475-4.

[23] K. Pan *et al.*, "The performance of a silica-based mixed gel electrolyte in lead acid batteries," *J. Power Sources*, vol. 209, no. June 2011, pp. 262–268, Jul. 2012, doi: 10.1016/j.jpowsour.2012.02.101.

[24] M. Q. Chen, H. Y. Chen, D. Shu, A. J. Li, and D. E. Finlow, "Effects of preparation condition and particle size distribution on fumed silica gel valve-regulated lead-acid batteries performance," *J. Power Sources*, vol. 181, no. 1, pp. 161–171, Jun. 2008, doi: 10.1016/j.jpowsour.2008.03.009.

[25] H. Li, H. Liu, Q. Wang, H. Chen, A. Ren, and J. Hu, "Effects of covalently bonded siloxane on the electrochemical and physical behaviour of GEL-VRLA battery," *Electrochim. Acta*, vol. 56, no. 2, pp. 663–666, Dec. 2010, doi: 10.1016/j.electacta.2010.09.075.

[26] M. L. Soria, J. C. Hernández, J. Valenciano, A. Sánchez, and F. Trinidad, "New developments on valve-regulated lead-acid batteries for advanced automotive electrical systems," *J. Power Sources*, vol. 144, no. 2, pp. 473–

485, Jul. 2005, doi: 10.1016/j.jpowsour.2004.11.005.

[27] A. Mansuroglu *et al.*, "N-Doped Graphene Oxide as Additive for Fumed Silica Based Gel Electrolyte of Valve Regulated Lead Acid Batteries," *J. Electrochem. Soc.*, vol. 168, no. 6, p. 060512, Jun. 2021, doi: 10.1149/1945-7111/ac0555.

[28] A. Mansuroglu, M. Gencten, M. B. Arvas, M. Sahin, A. E. Bozdoğan, and Y. Sahin, "A novel electrolyte additive for gel type valve regulated lead acid batteries: Sulfur doped graphene oxide," *Int. J. Energy Res.*, vol. 45, no. 15, pp. 21390–21402, Dec. 2021, doi: 10.1002/er.7189.

[29] A. Mansuroglu, M. Gencten, M. B. Arvas, M. Sahin, and Y. Sahin, "Investigation the effects of chlorine doped graphene oxide as an electrolyte additive for gel type valve regulated lead acid batteries," *J. Energy Storage*, vol. 64, no. July 2022, p. 107224, Aug. 2023, doi: 10.1016/j.est.2023.107224.

[30] M. Chen *et al.*, "Effect of polyols on the electrochemical behavior of gel valve-regulated lead-acid batteries," *Electrochim. Acta*, vol. 164, pp. 243–251, May 2015, doi: 10.1016/j.electacta.2015.02.210.

[31] Y. ŞAHİN, M. GENÇTEN, and K. B. DÖNMEZ, "a Novel Gel Electrolyte for Valve-Regulated Lead Acid Battery," *ANADOLU Univ. J. Sci. Technol. A - Appl. Sci. Eng.*, vol. 18, no. 1, pp. 146–146, Mar. 2017, doi: 10.18038/aubtda.300420.

[32] N. S. P. Sari, T. Nurtono, W. Widiyastuti, and H. Setyawan, "Cellulose-Based Hydrogel Polymer Electrolyte Derived from Coir Fiber for High-Performance Lead-Acid Batteries," *Energy Technol.*, vol. 13, no. 1, Jan. 2025, doi: 10.1002/ente.202401307.

[33] B. S. Chikkatti *et al.*, "Novel polymer gel electrolytes comprising montmorillonite embedded in sodium alginate and their electrochemical performance for future lead acid batteries," *New J. Chem.*, vol. 49, pp. 3654–3660, 2025, doi: 10.1039/d4nj05557h.

[34] Y. Yang *et al.*, "The Possible Mechanism of Improving the Performance of Lead-Acid Batteries by Using Aluminum Ions to Influence the Gel

Structure," *Energy Technol.*, no. 12, Jul. 2024, doi: 10.1002/ente.202400570.

[35] S. H. Rajur *et al.*, "Unleashing the electrochemical performance of zirconia nanoparticles on valve-regulated lead acid battery," *Heliyon*, vol. 10, no. 8, p. e29724, 2024, doi: 10.1016/j.heliyon.2024.e29724.

[36] B. S. Chikkatti, A. M. Sajjan, P. B. Kalahal, and N. R. Banapurmath, "Insight into the performance of valve-regulated lead-acid battery using sodium salt of poly(4-styrene sulfonic acid-co-maleic acid)-poly(vinyl alcohol) gel electrolyte," *J. Energy Storage*, vol. 72, no. PA, p. 108261, Nov. 2023, doi: 10.1016/j.est.2023.108261.

[37] M. G. Insinga, A. Derelitto, S. Pisana, R. L. Oliveri, C. Sunseri, and R. Inguanta, "Gelled electrolyte for nanostructured lead-acid battery," *Chem. Eng. Trans.*, vol. 73, no. January, pp. 25–30, 2019, doi: 10.3303/CET1973005.

[38] K. B. Dönmez, M. Gençten, and Y. Şahin, "A novel polysiloxane-based polymer as a gel agent for gel–VRLA batteries," *Ionics (Kiel).*, vol. 23, no. 8, pp. 2077–2089, 2017, doi: 10.1007/s11581-017-2040-y.

[39] M. G. Sumdani, M. R. Islam, A. N. A. Yahaya, and S. I. Safie, "Recent advancements in synthesis, properties, and applications of conductive polymers for electrochemical energy storage devices: A review," *Polym. Eng. Sci.*, vol. 62, no. 2, pp. 269–303, 2022, doi: 10.1002/pen.25859.

[40] T. Nezakati, A. Seifalian, A. Tan, and A. M. Seifalian, "Conductive Polymers: Opportunities and Challenges in Biomedical Applications," *Chem. Rev.*, vol. 118, no. 14, pp. 6766–6843, Jul. 2018, doi: 10.1021/acs.chemrev.6b00275.

[41] K. Namsheer and C. S. Rout, "Conducting polymers: a comprehensive review on recent advances in synthesis, properties and applications," *RSC Advances*, vol. 11, no. 10. Royal Society of Chemistry, pp. 5659–5697, Feb. 03, 2021. doi: 10.1039/d0ra07800j.

[42] Y. Shi, L. Peng, Y. Ding, Y. Zhao, and G. Yu, "Nanostructured conductive polymers for advanced energy storage," *Chem. Soc. Rev.*, vol. 44, no. 19, pp. 6684–6696, Oct. 2015, doi: 10.1039/c5cs00362h.

[43] O. Yilmaz, H. Y. Kalyon, M. Gencten, and Y. Sahin, “One step production of phosphorene from red phosphorus and investigation of their supercapacitor applications with conducting polymers,” *J. Energy Storage*, vol. 79, no. November 2023, p. 110133, 2024, doi: 10.1016/j.est.2023.110133.

[44] A. K. Poddar, S. S. Patel, and H. D. Patel, “Synthesis, characterization and applications of conductive polymers: A brief review,” *Polym. Adv. Technol.*, vol. 32, no. 12, pp. 4616–4641, 2021, doi: 10.1002/pat.5483.

[45] S. Suriyakumar, P. Bhardwaj, A. N. Grace, and A. M. Stephan, “Role of Polymers in Enhancing the Performance of Electrochemical Supercapacitors: A Review,” *Batter. Supercaps*, vol. 4, no. 4, pp. 571–584, Apr. 2021, doi: 10.1002/batt.202000272.

[46] A. R. Peringath *et al.*, “Chemical synthesis of polyaniline and polythiophene electrodes with excellent performance in supercapacitors,” *J. Energy Storage*, vol. 73, no. PA, p. 108811, 2023, doi: 10.1016/j.est.2023.108811.

[47] L. C. P. Almeida, “Conducting polymers: Synthesis, properties and applications,” *Conduct. Polym. Synth. Prop. Appl.*, no. November 2015, pp. 1–358, 2013, doi: 10.17148/IARJSET.2015.21123.

[48] J. C. Carranza-Cruz, E. Rivera, G. Santana, S. Martínez-Gallegos, and J. Illescas, “Synthesis of polyaniline (PANI) through chemical oxidation for its preparation in thin films,” *MRS Adv.*, vol. 6, no. 43–44, pp. 965–968, Dec. 2021, doi: 10.1557/s43580-021-00178-y.

[49] B. Ok, M. Gencten, M. B. Arvas, and Y. Sahin, “One-pot synthesis of Vanadium-doped conducting polymers for using as electrode materials of supercapacitors,” *J. Mater. Sci. Mater. Electron.*, vol. 34, no. 23, pp. 1–13, 2023, doi: 10.1007/s10854-023-11102-5.

[50] I. Sapurina *et al.*, “Polypyrrole nanotubes: The tuning of morphology and conductivity,” *Polymer (Guildf).*, vol. 113, pp. 247–258, 2017, doi: 10.1016/j.polymer.2017.02.064.

[51] C. Saravanan, R. C. Shekhar, and S. Palaniappan, “Synthesis of polypyrrole using benzoyl peroxide as a novel oxidizing agent,” *Macromol. Chem. Phys.*,

vol. 207, no. 3, pp. 342–348, 2006, doi: 10.1002/macp.200500376.

[52] N. S. Wadatkar and S. A. Waghuley, "Studies on properties of as-synthesized conducting polythiophene through aqueous chemical route," *J. Mater. Sci. Mater. Electron.*, vol. 27, no. 10, pp. 10573–10581, 2016, doi: 10.1007/s10854-016-5152-7.

[53] M. Gençten, K. B. Dönmez, Y. Şahin, K. Pekmez, and E. Suvacı, "Voltammetric and electrochemical impedimetric behavior of silica-based gel electrolyte for valve-regulated lead-acid battery," *J. Solid State Electrochem.*, vol. 18, no. 9, pp. 2469–2479, Sep. 2014, doi: 10.1007/s10008-014-2507-y.

[54] M. Trchová and J. Stejskal, "Polyaniline: The infrared spectroscopy of conducting polymer nanotubes (IUPAC Technical report)," *Pure Appl. Chem.*, vol. 83, no. 10, pp. 1803–1817, 2011, doi: 10.1351/PAC-REP-10-02-01.

[55] K. Y. Lin *et al.*, "Characterization of polyaniline synthesized from chemical oxidative polymerization at various polymerization temperatures," *Eur. Polym. J.*, vol. 88, pp. 311–319, 2017, doi: 10.1016/j.eurpolymj.2017.01.035.

[56] W. Zeng *et al.*, "Enhanced Ion Conductivity in Conducting Polymer Binder for High-Performance Silicon Anodes in Advanced Lithium-Ion Batteries," *Adv. Energy Mater.*, vol. 8, no. 11, Apr. 2018, doi: 10.1002/aenm.201702314.

[57] J. Liu, M. Zhou, L. Z. Fan, P. Li, and X. Qu, "Porous polyaniline exhibits highly enhanced electrochemical capacitance performance," *Electrochim. Acta*, vol. 55, no. 20, pp. 5819–5822, 2010, doi: 10.1016/j.electacta.2010.05.030.

[58] H. Xu, X. Li, and G. Wang, "Polyaniline nanofibers with a high specific surface area and an improved pore structure for supercapacitors," *J. Power Sources*, vol. 294, pp. 16–21, Oct. 2015, doi: 10.1016/j.jpowsour.2015.06.053.

[59] H. Noby, A. H. El-Shazly, M. F. Elkady, and M. Ohshima, "Strong acid

doping for the preparation of conductive polyaniline nanoflowers, nanotubes, and nanofibers," *Polymer (Guildf).*, vol. 182, no. June, p. 121848, 2019, doi: 10.1016/j.polymer.2019.121848.

[60] E. Ahlatcio¦lu Özerol, B. F. Şenkal, and M. Okutan, "Preparation and characterization of graphite composites of polyaniline," *Microelectron. Eng.*, vol. 146, pp. 76–80, 2015, doi: 10.1016/j.mee.2015.03.062.

[61] N. T. Tung, T. Van Khai, H. Lee, and D. Sohn, "The effects of dopant on morphology formation in polyaniline graphite nanoplatelet composite," *Synth. Met.*, vol. 161, no. 1–2, pp. 177–182, 2011, doi: 10.1016/j.synthmet.2010.11.018.

[62] L. Nikzad, S. Alibeigi, M. R. Vaezi, B. Yazdani, and M. R. Rahimipour, "Synthesis of a graphite-polyaniline nanocomposite and evaluation of its electrochemical properties," *Chem. Eng. Technol.*, vol. 32, no. 6, pp. 861–866, Jun. 2009, doi: 10.1002/ceat.200800470.

[63] X. S. Du, M. Xiao, and Y. Z. Meng, "Facile synthesis of highly conductive polyaniline/graphite nanocomposites," *Eur. Polym. J.*, vol. 40, no. 7, pp. 1489–1493, 2004, doi: 10.1016/j.eurpolymj.2004.02.009.

[64] R. M. N. M. Rathnayake *et al.*, "Graphite intercalated polyaniline composite with superior anticorrosive and hydrophobic properties, as protective coating material on steel surfaces," *Appl. Surf. Sci.*, vol. 410, pp. 445–453, 2017, doi: 10.1016/j.apsusc.2017.03.119.

[65] T. N. Atiqah, S. J. Tan, K. L. Foo, A. G. Supri, A. M. M. Al Bakri, and Y. M. Liew, "Effect of graphite loading on properties of polyaniline/graphite composites," *Polym. Bull.*, vol. 75, no. 1, pp. 209–220, 2018, doi: 10.1007/s00289-017-2031-1.

[66] B. Senthilkumar, P. Thenamirtham, and R. Kalai Selvan, "Structural and electrochemical properties of polythiophene," *Appl. Surf. Sci.*, vol. 257, no. 21, pp. 9063–9067, 2011, doi: 10.1016/j.apsusc.2011.05.100.

[67] Y. Lu, S. Wang, C. Xiong, and G.-H. Hu, "Synthesis and characterization of a liquid-like polythiophene and its potential applications," *Synth. Met.*, vol. 270, no. June, p. 116603, Dec. 2020, doi: 10.1016/j.synthmet.2020.116603.

[68] M. R. Karim, K. T. Lim, C. J. Lee, and M. S. Lee, “A facile synthesis of polythiophene nanowires,” *Synth. Met.*, vol. 157, no. 22–23, pp. 1008–1012, Nov. 2007, doi: 10.1016/j.synthmet.2007.10.010.

[69] A. Husain, S. Ahmad, and F. Mohammad, “Preparation and Applications of Polythiophene Nanocomposites,” *JESC) J. Eng. Sci. Comput.*, vol. I, no. Iii, pp. 36–53, 2020.

[70] J. P. Melo, E. N. Schulz, C. Morales-Verdejo, S. L. Horswell, and M. B. Camarada, “Synthesis and characterization of graphene/polythiophene (GR/PT) nanocomposites: Evaluation as high-performance supercapacitor electrodes,” *Int. J. Electrochem. Sci.*, vol. 12, no. 4, pp. 2933–2948, 2017, doi: 10.20964/2017.04.09.

[71] R. Shah, A. Kausar, and B. Muhammad, “Exploration of polythiophene/graphene, poly(methyl methacrylate)/graphene and polythiophene-co- poly(methyl methacrylate)/graphene nanocomposite obtained via in-situ technique,” *J. Plast. Film Sheeting*, vol. 31, no. 2, pp. 144–157, 2015, doi: 10.1177/8756087915572934.

[72] M. R. Karim, C. J. Lee, and M. S. Lee, “Synthesis and characterization of conducting polythiophene/carbon nanotubes composites,” *J. Polym. Sci. Part A Polym. Chem.*, vol. 44, no. 18, pp. 5283–5290, Sep. 2006, doi: 10.1002/pola.21640.

[73] Y. C. Wong, Y. H. Wong, B. C. Ang, A. A. Baharuddin, and A. S. M. A. Haseeb, “Effects of polymerization oxidants on the fabrication of electrospun PPy/WO3 composites,” *J. Mater. Sci. Mater. Electron.*, vol. 34, no. 1, pp. 1–15, 2023, doi: 10.1007/s10854-022-09483-0.

[74] Y. Wang, R. Song, L. Li, R. Fu, Z. Liu, and B. Li, “High crystalline quality conductive polypyrrole film prepared by interface chemical oxidation polymerization method,” *Appl. Sci.*, vol. 12, no. 1, 2022, doi: 10.3390/app12010058.

[75] N. V. Dave and D. M. Nerkar, “The influence of the oxidant on structural and morphological properties of conductive polypyrrole,” *Mater. Today Proc.*, vol. 45, pp. 5939–5943, 2020, doi: 10.1016/j.matpr.2020.09.104.

[76] G. Gheno, N. R. De Souza Basso, and R. Hübler, “Polyaniline/graphite nanocomposites: Synthesis and characterization,” *Macromol. Symp.*, vol. 299–300, no. 1, pp. 74–80, 2011, doi: 10.1002/masy.200900137.

[77] X. G. Li, J. Li, and M. R. Huang, “Facile optimal synthesis of inherently electroconductive polythiophene nanoparticles,” *Chem. - A Eur. J.*, vol. 15, no. 26, pp. 6446–6455, 2009, doi: 10.1002/chem.200900181.

[78] D. Thanasamy, D. Jesuraj, S. K. Konda kannan, and V. Avadhanam, “A novel route to synthesis polythiophene with great yield and high electrical conductivity without post doping process,” *Polymer (Guildf).*, vol. 175, no. March, pp. 32–40, Jun. 2019, doi: 10.1016/j.polymer.2019.03.042.

[79] A. Yussuf, M. Al-Saleh, S. Al-Enezi, and G. Abraham, “Synthesis and Characterization of Conductive Polypyrrole: The Influence of the Oxidants and Monomer on the Electrical, Thermal, and Morphological Properties,” *Int. J. Polym. Sci.*, vol. 2018, pp. 1–8, Jul. 2018, doi: 10.1155/2018/4191747.

[80] A. Kausaite-Minkstimiene, V. Mazeiko, A. Ramanaviciene, and A. Ramanavicius, “Evaluation of chemical synthesis of polypyrrole particles,” *Colloids Surfaces A Physicochem. Eng. Asp.*, vol. 483, pp. 224–231, 2015, doi: 10.1016/j.colsurfa.2015.05.008.

[81] S. J. Hawkins and N. M. Ratcliffe, “A study of the effects of acid on the polymerisation of pyrrole, on the oxidative polymerisation of pyrrole and on polypyrrole,” *J. Mater. Chem.*, vol. 10, no. 9, pp. 2057–2062, 2000, doi: 10.1039/b001912g.

[82] W. F. Alves *et al.*, “Thermo-analyses of polyaniline and its derivatives,” *Thermochim. Acta*, vol. 502, no. 1–2, pp. 43–46, 2010, doi: 10.1016/j.tca.2010.02.003.

[83] J. Stejskal and R. G. Gilbert, “POLYANILINE. PREPARATION OF A CONDUCTING POLYMER,” *Pure Appl. Chem.*, vol. 74, no. 5, pp. 857–867, 2002.

[84] D. P. Bhattarai *et al.*, “Synthesis of polythiophene nanoparticles by surfactant-free chemical oxidative polymerization method: Characterization, in vitro biomineralization, and cytotoxicity evaluation,” *J. Ind. Eng. Chem.*,

vol. 77, pp. 243–252, 2019, doi: 10.1016/j.jiec.2019.04.045.

[85] N. Hebestreit, J. Hofmann, U. Rammelt, and W. Plieth, “Physical and electrochemical characterization of nanocomposites formed from polythiophene and titaniumdioxide,” *Electrochim. Acta*, vol. 48, no. 13, pp. 1779–1788, 2003, doi: 10.1016/S0013-4686(02)00783-1.

[86] X. Hong *et al.*, “A novel ternary hybrid electromagnetic wave-absorbing composite based on BaFe11.92(LaNd)0.04O19-titanium dioxide/multiwalled carbon nanotubes/polythiophene,” *Compos. Sci. Technol.*, vol. 117, pp. 215–224, Sep. 2015, doi: 10.1016/j.compscitech.2015.06.022.

[87] R. S. Futane, V. M. Raut, and S. D. Dhande, “Synthesis and characterisation of polythiophene and Tio2 doped polythiophene thin films by chemical bath deposition,” *Rasayan J. Chem.*, vol. 9, no. 4, pp. 842–848, 2016, [Online]. Available: https://www.rasayanjournal.co.in/admin/php/upload/96_pdf.pdf

[88] K. Kadac and J. Nowaczyk, “Polythiophene nanoparticles in aqueous media,” *J. Appl. Polym. Sci.*, vol. 133, no. 23, pp. 1–10, 2016, doi: 10.1002/app.43495.

[89] X. Yin, Y. Li, Y. Feng, and W. Feng, “Polythiophene/graphite fluoride composites cathode for high power and energy densities lithium primary batteries,” *Synth. Met.*, vol. 220, pp. 560–566, Oct. 2016, doi: 10.1016/j.synthmet.2016.07.032.

[90] T. M. Wu, H. L. Chang, and Y. W. Lin, “Synthesis and characterization of conductive polypyrrole with improved conductivity and processability,” *Polym. Int.*, vol. 58, no. 9, pp. 1065–1070, 2009, doi: 10.1002/pi.2634.

[91] B. Butoi, A. Groza, P. Dinca, A. Balan, and V. Barna, “Morphological and structural analysis of polyaniline and poly(o-anisidine) layers generated in a DC glow discharge plasma by using an oblique angle electrode deposition configuration,” *Polymers (Basel).*, vol. 9, no. 12, 2017, doi: 10.3390/polym9120732.

[92] S. Golba *et al.*, “Impact of Acidity Profile on Nascent Polyaniline in the Modified Rapid Mixing Process—Material Electrical Conductivity and

Morphological Study," *Materials (Basel).*, vol. 13, no. 22, p. 5108, Nov. 2020, doi: 10.3390/ma13225108.

[93] X. G. Li, J. Li, Q. K. Meng, and M. R. Huang, "Interfacial synthesis and widely controllable conductivity of polythiophene microparticles," *J. Phys. Chem. B*, vol. 113, no. 29, pp. 9718–9727, 2009, doi: 10.1021/jp901395u.

[94] F. M. A. Almuntaser, S. Majumder, P. K. Baviskar, J. V. Sali, and B. R. Sankapal, "Synthesis and characterization of polypyrrole and its application for solar cell," *Appl. Phys. A Mater. Sci. Process.*, vol. 123, no. 8, 2017, doi: 10.1007/s00339-017-1131-y.

[95] M. A. Chougule, S. G. Pawar, P. R. Godse, R. N. Mulik, S. Sen, and V. B. Patil, "Synthesis and Characterization of Polypyrrole (PPy) Thin Films," *Soft Nanosci. Lett.*, vol. 01, no. 01, pp. 6–10, 2011, doi: 10.4236/snl.2011.11002.

[96] H. K. Chitte, G. N. Shinde, N. V. Bhat, and V. E. Walunj, "Synthesis of Polypyrrole Using Ferric Chloride (FeCl₃) as Oxidant Together with Some Dopants for Use in Gas Sensors," *J. Sens. Technol.*, vol. 01, no. 02, pp. 47–56, 2011, doi: 10.4236/jst.2011.12007.

[97] A. Singh, P. B. Karandikar, and N. R. Kulkarni, "Mitigation of sulfation in lead acid battery towards life time extension using ultra capacitor in hybrid electric vehicle," *J. Energy Storage*, vol. 34, no. January, p. 102219, Feb. 2021, doi: 10.1016/j.est.2020.102219.

[98] H. A. Catherino, F. F. Feres, and F. Trinidad, "Sulfation in lead–acid batteries," *J. Power Sources*, vol. 129, no. 1, pp. 113–120, Apr. 2004, doi: 10.1016/j.jpowsour.2003.11.003.

[99] X. Xu, J. Liu, Q. Zhang, and H. Wang, "A facile approach to suppress the sulfation in lead acid batteries using N-doped carbon derived from chitosan," *Mater. Lett.*, vol. 247, pp. 29–31, Jul. 2019, doi: 10.1016/j.matlet.2019.03.055.

[100] P. Sharma and V. Kumar, "Current Technology of Supercapacitors: A Review," *J. Electron. Mater.*, vol. 49, no. 6, pp. 3520–3532, 2020, doi: 10.1007/s11664-020-07992-4.

[101] N. Kularatna, *Energy Storage Devices for Electronic Systems*. Elsevier, 2015. doi: 10.1016/C2012-0-06356-9.

[102] N. Boudieb, B. Moussa, Z. Ghebache, T. H. Boumediene, and F. Hamidouche, "Electrochemical behaviors of negative and positive plates lead- acid battery in the presence of polyaniline hydro-soluble in 0 . 5 M," *Int. J. Chem. Chem. Eng. Syst.*, vol. 4, no. March, pp. 21–27, 2020.

[103] S. M. Adnan, S. Zaidi, and I. I, "High Energy Density Polyaniline/Exfoliated Graphite Based Supercapacitor with Improved Stability in Wide Voltage Window," *Orient. J. Chem.*, vol. 37, no. 2, pp. 450–458, 2021, doi: 10.13005/ojc/370227.

[104] z A. N. Nabeel, A. Jain, K. C. Juglan, S. Bhagwa, and S. Naeem, "Structural, Morphological, and Electrochemical Characteriation of Polypyrrole-Enhanced Reduced Graphene Oxide/$NiCoFe_2O_4$ Ternary Composite for High-Performance Supercapacitors," *Energy Technol.*, Feb. 2025, doi: 10.1002/ente.202402142.

[105] A. A. Alguail, A. H. Al-Eggiely, M. M. Gvozdenović, B. Z. Jugović, and B. N. Grgur, "Battery type hybrid supercapacitor based on polypyrrole and lead-lead sulfate," *J. Power Sources*, vol. 313, pp. 240–246, 2016, doi: 10.1016/j.jpowsour.2016.02.081.

[106] V. Niščáková, A. Gubóová, O. Petruš, H. Fei, M. Almáši, and A. S. Fedorková, "Investigation of polypyrrole based composite material for lithium sulfur batteries," *Sci. Rep.*, vol. 14, no. 1, p. 22928, Oct. 2024, doi: 10.1038/s41598-024-74119-8.

[107] K. Maksymiuk, "Chemical reactivity of polypyrrole and its relevance to polypyrrole based electrochemical sensors," *Electroanalysis*, vol. 18, no. 16, pp. 1537–1551, 2006, doi: 10.1002/elan.200603573.

[108] K. S. Ryu, Y. Lee, K. S. Han, and M. G. Kim, "The electrochemical performance of polythiophene synthesized by chemical method as the polymer battery electrode," *Mater. Chem. Phys.*, vol. 84, no. 2–3, pp. 380–384, 2004, doi: 10.1016/j.matchemphys.2003.12.009.

[109] T. M. S. K. Pathiranage, D. S. Dissanayake, C. N. Niermann, Y. Ren, M. C.

Biewer, and M. C. Stefan, “Role of polythiophenes as electroactive materials,” *J. Polym. Sci. Part A Polym. Chem.*, vol. 55, no. 20, pp. 3327–3346, 2017, doi: 10.1002/pola.28726.

[110] F. Wu *et al.*, “Sulfur/polythiophene with a core/shell structure: Synthesis and electrochemical properties of the cathode for rechargeable lithium batteries,” *J. Phys. Chem. C*, vol. 115, no. 13, pp. 6057–6063, 2011, doi: 10.1021/jp1114724.

[111] R. Ullah, M. Ullah, N. Khan, and M. Rahim, “Electrochemical properties of polythiophene/iron dust composites synthesized using chemical oxidative polymerization,” *J. Solid State Electrochem.*, vol. 28, no. 11, pp. 4119–4129, 2024, doi: 10.1007/s10008-024-06008-z.

[112] B. H. Patil, S. J. Patil, and C. D. Lokhande, “Electrochemical characterization of chemically synthesized polythiophene thin films: Performance of asymmetric supercapacitor device,” *Electroanalysis*, vol. 26, no. 9, pp. 2023–2032, 2014, doi: 10.1002/elan.201400284.

[113] R. Gašparac and C. R. Martin, “Investigations of the Mechanism of Corrosion Inhibition by Polyaniline. Polyaniline-Coated Stainless Steel in Sulfuric Acid Solution,” *J. Electrochem. Soc.*, vol. 148, no. 4, p. B138, 2001, doi: 10.1149/1.1354615.

[114] H. Iken, R. Basseguy, A. Guenbour, and A. Ben Bachir, “Classic and local analysis of corrosion behaviour of graphite and stainless steels in polluted phosphoric acid,” *Electrochim. Acta*, vol. 52, no. 7, pp. 2580–2587, 2007, doi: 10.1016/j.electacta.2006.09.013.

[115] G. F. Chen, Z. Q. Liu, J. M. Lin, N. Li, and Y. Z. Su, “Hierarchical polypyrrole based composites for high performance asymmetric supercapacitors,” *J. Power Sources*, vol. 283, pp. 484–493, 2015, doi: 10.1016/j.jpowsour.2015.02.103.

[116] Y. Huang *et al.*, “Nanostructured Polypyrrole as a flexible electrode material of supercapacitor,” *Nano Energy*, vol. 22, pp. 422–438, 2016, doi: 10.1016/j.nanoen.2016.02.047.

[117] M. Al-Bujasim, M. Gencten, K. B. Donmez, M. B. Arvas, N. Karatepe, and

Y. Sahin, “A Tripartite Composite Incorporating Nitrogen-Doped Graphene Oxide, Polypyrrole, and Silica for Lithium-Ion Battery Anodes,” *ECS J. Solid State Sci. Technol.*, vol. 13, no. 5, p. 051001, 2024, doi: 10.1149/2162-8777/ad423b.

[118] M. Gençten, “Investigation the effects of boehmite and gibbsite on the electrochemical behaviours of Gel-VRLA batteries,” *Int. J. Electrochem. Sci.*, vol. 13, no. 12, pp. 11741–11751, Dec. 2018, doi: 10.20964/2018.12.15.

[119] N. T. van Anh, M. T. Thanh Thuy, M. T. Xuan, and P. T. Binh, “Study on electrochemical properties of gelled electrolytes using nano fumed silica in the presence of some organic additives,” *Int. J. Nanotechnol.*, vol. 17, no. 7–10, pp. 648–658, 2020, doi: 10.1504/IJNT.2020.111331.

PUBLICATIONS FROM THE THESIS

Conference Papers

1. Mira, Ziyad, and Metin Gençten. "Investigation The Electrochemical Performance of Fumed Silica Based Gel Electrolyte-Lead Acid Batteries Using Polypyrrole Additive." Bakü, Azerbycan, (2024).
2. Mira, Ziyad, and Metin Gençten. "Electrochemical Evaluation of Lead Electrodes in Polyaniline-Doped Fumed Silica Gel Electrolytes." structure 4: 5., İzmit, Türkiye, (2025).

Papers

1. Z. Mira, I. C. Turu, and M. Gencten, “Enhancement of valve-regulated lead-acid battery performance using polyaniline additive in fumed silica–based gel electrolyte,” *Ionics (Kiel).*, vol. 31, no. 8, pp. 8043–8060, Aug. 2025, doi: 10.1007/s11581-025-06487-8.
2. Z. Mira, I. C. Turu, and M. Gencten, “Enhanced electrochemical performance of fumed silica-based gel electrolyte with polypyrrole for valve-regulated lead-acid batteries,” *J. Appl. Electrochem.*, vol. 55, no. 10, pp. 2755–2772, Oct. 2025, doi: 10.1007/s10800-025-02335-9.
3. Z. Mira and M. Gencten, “Electrochemical Performance Enhancement of VRLA Gel Electrolytes via Polythiophene Addition,” *J. Electrochem. Soc.*, vol. 173, no. 7, p. 070507, Apr. 2026, doi: 10.1149/1945-7111/ae568f.

Projects

1. Researcher, The Scientific and Technological Research Council of Türkiye (TÜBİTAK) for 124M200 Project code.